MICROCOPY RESOLUTION TEST CHART

NATIONAL BUREAU OF STANDARDS 1963 A

⑪

REPORT DOCUMENTATION PAGE

AD-A149 992	**1b. RESTRICTIVE MARKINGS**
	3. DISTRIBUTION/AVAILABILITY OF REPORT
2b. DECLASSIFICATION/DOWNGRADING SCHEDULE	Approved for public release; distribution unlimited.

4. PERFORMING ORGANIZATION REPORT NUMBER(S)
Final Technical Report

5. MONITORING ORGANIZATION REPORT NUMBER(S)
AFOSR-TR- 2578

6a. NAME OF PERFORMING ORGANIZATION	**6b. OFFICE SYMBOL** *(If applicable)*	**7a. NAME OF MONITORING ORGANIZATION**
The University of Chicago		AFOSR/NE

6c. ADDRESS *(City, State and ZIP Code)*	**7b. ADDRESS** *(City, State and ZIP Code)*
5801 S. Ellis Ave. Chicago, IL 60637	

8a. NAME OF FUNDING/SPONSORING ORGANIZATION Air Force Office of Scientific Research/AFSC	**8b. OFFICE SYMBOL** *(If applicable)* AFOSR/AFSC	**9. PROCUREMENT INSTRUMENT IDENTIFICATION NUMBER** F49620-83-C-0110

8c. ADDRESS *(City, State and ZIP Code)*
Directorate of Electronic & Mat. Sciences
Building 410
Bolling AFB DC 20332

10. SOURCE OF FUNDING NOS.

PROGRAM ELEMENT NO.	PROJECT NO.	TASK NO.	WORK UNIT NO.
61102F	2305	A4	

11. TITLE *(Include Security Classification)* New High Resolution Scanning Ion Microprobe & Focused Ion Beam Applications

12. PERSONAL AUTHOR(S)
Riccardo Levi-Setti, Principal Investigator

13a. TYPE OF REPORT Final Technical	**13b. TIME COVERED** FROM 6/01/80 TO 5/31/84	**14. DATE OF REPORT** *(Yr., Mo., Day)* 8/31/84	**15. PAGE COUNT** 151

16. SUPPLEMENTARY NOTATION

17. COSATI CODES			**18. SUBJECT TERMS** *(Continue on reverse if necessary and identify by block number)*
FIELD	GROUP	SUB. GR.	

19. ABSTRACT *(Continue on reverse if necessary and identify by block number)*

The University of Chicago and Hughes Research Laboratories have successfuly completed a four-year collaborative program for the development and construction of two 60 kV high-resolution, high current density ion-microscopes/microprobes. Performance evaluation tests with a liquid gallium ion source have thus far demonstrated focused spot diameters of 90 and 45 nanometers, excellent imaging capability using ion-induced secondary electrons and ion signals, and unusual performance of a high-transmission secondary ion mass spectrometry system. Concurrently with the new microprobe development, previously existing prototype scanning ion microscopes have been employed in fundamental studies of ion-solid interactions and contrast mechanisms in ion microscopy, where ion-channelling effects in crystalline materials yield images exhibiting extraordinary crystallographic contrast. Exploratory research applications of the new microprobes comprise elemental mapping at high spatial resolution (50 nm) of microelectronic structures and devices in gallium arsenide, studies of the (continued)

20. DISTRIBUTION/AVAILABILITY OF ABSTRACT UNCLASSIFIED/UNLIMITED ☑ SAME AS RPT ☐ DTIC USERS ☐	**21. ABSTRACT SECURITY CLASSIFICATION**

22a. NAME OF RESPONSIBLE INDIVIDUAL Dr. Gerald Witt	**22b. TELEPHONE NUMBER** *(Include Area Code)* (202) 767-4984	**22c. OFFICE SYMBOL** AFOSR/NE

DD FORM 1473, 83 APR EDITION OF 1 JAN 73 IS OBSOLETE.

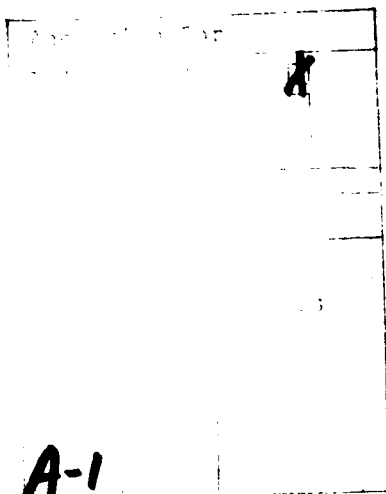85 01 25 064 page i

(Abstract, continued)

elemental composition and mineral distribution in stony meteorites (chondrites), with emphasis on the analysis of the rims of primordial aggregate bodies (chondrules), the detection of staging domains in antimony pentacloride-intercalated graphites, elemental mapping in minerals of biological origin, in particular the detection of the onset of calcification in bone tissues, and various approaches to focused ion beam microfabrication and microlithography, where structures with 100 nm linewidth have been demonstrated.

DTIC
COPY
INSPECTED

A-1

New High Resolution Scanning Ion Microprobe

and Focused Ion Beam Applications

FINAL TECHNICAL REPORT

AFOSR Contracts No.   F49620-80-C-0074

No.   F49620-83-C-0110

Principal Investigator: Riccardo Levi-Setti

Contract Period: June 01, 1980 through May 30, 1984

TABLE OF CONTENTS

New High Resolution Scanning Ion Microprobe
and Focused Ion Beam Applications

FINAL TECHNICAL REPORT

AFOSR Contracts No. ~~F49620-80-C-0074~~
No. F49620-83-C-0110

Principal Investigator: Riccardo Levi-Setti

Contract Period: June 01, 1980 through May 30, 1984

1. Objectives of the Research Effort

Over the period June 01, 1980 through May 30, 1984, the University of Chicago (UC) and Hughes Research Laboratories (HRL) have been engaged in a collaborative program of research and development which received joint AFOSR and NSF support. Prime objective of the UC-HRL program has been the development and construction of two 60 keV high resolution, high current density scanning ion microscopes/microprobes (SIM). Concurrent objectives have been the study of various aspects of the ion-solid interaction and SIM imaging, undertaken at UC with the existing prototype SIM. Two sets of coordinated technical and scientific tasks did form an integral part of the original three-year UC-HRL program. These tasks were extended to cover an additional fourth year, as dictated by the circumstances at the end of the first three years of effort. An outline of the program tasks is as follows:

Task 1 (UC & HRL) Design studies using existing prototype columns.

These were to include,

a). At UC, the installation of an HRL-built liquid metal ion (LMI) source in the existing UC prototype scanning transmission ion microscope (STIM), the determination of fundamental Ga^+ ion source parameters, and the development and testing of fast counting detector electronics for high resolution image display.

b). At HRL, the development and testing of eutectic LMI sources using the HRL prototype SIM to obtain ion beams of semiconductor dopant species.

The results of these parallel investigations were to help in finalizing several aspects of the design and instrumentation relative to the new high performance ion probes to be constructed.

Task 2 (UC) Study of physical processes yielding image contrast in ion microscopy

This task was to be pursued using the existing UC-SIM, modified during the first year to operate with a Ga⁺ LMI source. Objectives were the study of ion induced secondary electron (ISE) and ion induced secondary ion (ISI) emission under Ga⁺ ion bombardment of solid targets. This exploratory program was meant to provide a better understanding of the phenomena to be exploited with the new ion microprobes in various research applications.

Task 3 (UC & HRL) New ion microprobe development: Design and construction.

This task represented the primary objective of the program. It involved

a). The performance of optical calculations leading to an optimized micro-scope design.
b). The preparation of the assembly and engineering designs of the various instrument subsystems.
c). The choice and procurement of components and instrumentation.
d). The actual fabrication of the microprobes.
e). The assembly and initial check-out of all subsystems.
f). SIM system integration.
g). The design, construction and installation of a high-transmission ISI energy analyzer and transport system (ATS) to be coupled to an RF quadru-pole mass filter.

Task 4 (UC & HRL) Performance evaluation of new ion microprobes.

This part of the program was to entail:
a). The determination of probe size and current, as a function of beam defining aperture.
b). The demonstration of the imaging capabilities of the new instruments, using the ISE and ISI signals, and pulse-mode or analog display.
c). The study of the microanalytical capabilities of the UC-HRL SIM using a Ga⁺ ion beam, by secondary ion mass spectrometry (SIMS), after optimiza-tion of the ATS and RF quadrupole mass filter operation.

Task 5 (UC & HRL) Exploratory research applications of the UC-HRL SIM.

Several tentative topics were selected for this last phase of the program, pending the actual performance of the microprobes. To be exploited were the microanalytical capability and the high spatial resolution of the SIM for the characterization of materials, as well as the opportunity to explore various aspects of focused ion beam (FIB) microlithography and microfabrication.

page 2

2. Status of the Research Effort.

The UC-HRL collaborative program has been eminently successful. Two copies of the UC-HRL SIM were constructed, one presently operating at UC, the other at HRL. The demonstrated performance of the new microprobes is unparalleled by any other competing efforts, either in the United States, Great Britain, or Japan. While the performance evaluation is still in progress at UC, based on exploratory research applications using a Ga^+ probe, the results thus far obtained are extremely encouraging and unprecedented. These have already raised much interest on part of scientists representing a wide range of research interests, and already have produced a heavy demand for observation time on the new microprobe.

The novel features of the UC-HRL SIM, which uses a 40-60 KeV heavy ion focused beam from liquid metal sources, are the spatial resolution, the beam current density and the high performance secondary ion mass spectrometry (SIMS) system. High quality micrographs have thus far been obtained with a picture resolution of 90 and 40 nm in the SIM modes (secondary ion or secondary electron images), as well as in elemental maps by SIMS. There is reasonable expectation that the 10 nm level will be reached in the current performance evaluation program, which is still in progress.

Determined have been the feasibility of obtaining high spatial resolution elemental maps of a variety of materials and artifacts, both conductors and insulators. These have included metals and alloys, silicate minerals in meteorites, minerals of organic origin, superconducting wire matrices, optical fibers, metallic glass, intercalated graphite, and integrated circuits in Si and GaAs. This capability, coupled with the pronounced crystallographic contrast present in the SIM images, make the new UC-HRL SIM an extremely powerful new analytical instrument.

A detailed account of the accomplishments of the program will now be presented, following the chronology represented by the five tasks summarized in Section 1. In view of the volume of supporting illustrations to be included, all figures are collected in five appendices. In the text to follow, references will be made to the figure number in each appendix, and to the cumulative list of publications listed on page

2.1 Accomplishments under Task 1:   Design studies using existing prototype columns.

This task was primarily carried out in the first year of the program, although the operation of the prototype SIM columns in later years, in parallel to the new ion microprobe development, did contribute significantly to the progress of high resolution ion microscopy.

a). After constructing an appropriate tantalum housing, an HRL-built LMI liquid gallium source was installed in the UC-STIM (Fig. A1-1). The new gallium probe has been operational since January 1981. Studied were the energy spectra and beam composition of the source. Fig. A1-2 shows two momentum spectra obtained with the STIM magnetic sector spectrometer. The energy spread of the emitted Ga^+ ions is characterized by a full width at half maximum in the range 7 - 50 eV for source currents in the range 0.6 - 50 µA, as shown in Fig. A1-3a. This information did set on a firm basis the design specifications of the new ion probes in regard to the effect of chromatic aberrations. It clearly indicated (Fig. A1-1b) the existence of an optimum operating condition which maximizes beam current while minimizing chromatic aberration.

b). Also explored have been the limitations in the pulse-mode image display at high counting rates. This was in order to simulate the conditions which would prevail at the highest resolution achievable with the new ion probe. It was determined that good quality micrographs with linear response could be obtained at counting rates up to $\sim$ 2 MHZ, while saturation and loss of contrast sets in at higher rates. Figs. A1-4 and -5 show representative images of a variety of structures, obtained with the ISE signal using a channel multiplier detector, under 60 keV Ga^+ ion bombardment.

Explored has also been the analog-mode of image display, after constructing a display system which uses the current signal from the channel multiplier. High-quality images reaching the theoretical resolution limit of the one-lens column ($\sim$ 1000 Å) for a particular optical aperture setting, have been obtained with this approach. This can yield fast interlaced scans (Figs. A1-6 and -7) or single slow scans for maximum resolution (Fig. A1-8). The exposure times for the micrographs shown were typically 8 - 10 seconds.

These early results have been reported in Publications (a) 5, 6. Although the imaging results are now obsolete, the imaging methods developed at the time played a very important role in later stages of the program. The prompt

page 4

optimization of the imaging capabilities of the new microprobe is largely due to this preparatory work, and to the use of display instrumentation developed during this exploratory phase.

2.2 Accomplishments under Task 2: Study of physical processed yielding image contrast in ion microscopy.

This area of research has represented in many respects the scientific backbone of the development at UC of ion microscopy. It is through the understanding of the physics of ion-solid interactions that one could identify those processes which yield selective imaging contrast, thus suggesting the most promising applications of the new high resolution probes. Also, through studies of such processes, Ph.D. students have been exposed to basic physics throughout the program.

The investigations under this task have been carried out during the entire duration of the project, using the prototype UC-SIM, whose performance has been gradually improved. This exploration of contrast mechanisms has brought to light a number of phenomena which have considerably broadened the practical role of the SIM for materials characterization, beyond its designed microanalytical capability by SIMS.

Various contrast mechanisms and their physical origin have been studied, based on ISE and ISI emission, as well as aspects of the sputtering process. In addition to contrast due to the surface topography, the SIM was found to yield strong elemental contrast (Z-contrast) and dramatic crystallographic contrast due to ion-channelling effects. Several publications have documented the results obtained in this continuing investigation (Publications (a) 7 through 15). Selected examples out of an overwhelming amount of collected observations are contained in Appendix 2.

a). Topographic contrast. It has been established that the SIM can give remarkably good contrast due to the surface topography of any kind of material, by collecting either the ISE or the ISI signal. A comparison of the images of a variety of objects obtained with either kind of signal is shown in Fig. A2-1 through 4. Examples of ISI imaging of uncoated insulators are shown in Fig. A2-5 through 7. Insulator charging effects, unnoticeable in ISI imaging, do exist in ISE imaging. In this case, however, Ga^+ ion implant may, in some cases, provide enough conductivity to prevent electrical charging (Figs. A2-8, 9). This is dramatically evident in a comparison of SIM vs. SEM

imaging of a passivated integrated circuit (Fig. A2-10), where charging effects in the SEM prevent sharp image focusing. Ga^+ implant, however, restores good SEM imaging conditions (Fig. A2-11).

b). Z-contrast. The contrast due to the Z-dependence of the secondary electron emission yields is very pronounced in the Ga^+ SIM and differs from that provided by the SEM. Examples of this comparison are shown in Figs. A2-12 and -13.

c). Crystallographic contrast. SIM imaging of polished samples of metal, alloys and semiconductors was found to be dominated by ion-channelling effects, yielding very pronounced crystallographic contrast in both ISE and ISI images. These phenomena have been studied in detail and have been understood in terms of the dependence of the secondary emission yields on the lattice orientation relative to the incident beam. The first observations related to brass samples, where sputter progressively enhanced the image contrast (Fig. A2-14). Comparisons with SEM images of the same areas immediately revealed an extra- ordinary difference of prevailing contrast mechanisms (Fig. A2-15). Cu samples provided even more spectacular examples (Fig. A2-16). Evidence of ion-channel- ling was obtained by comparing images taken at normal beam incidence, with images taken after tilting the sample by 10°. Since the angle of tilt is larger than the critical channelling angles for Ga^+ on Cu at 60 keV, dramatic contrast reversals due to ion channelling/dechannelling were obtained between the two sets of micrographs (Fig. A2-17). The observations were extended to correlate ISE and ISI images of corresponding areas, revealing predominant correlation of the two processes, with noticeable exceptions still an object of study at present (Fig. A2-18 through 21). The crystallographic contrast observed in the SIM is very large, the ISE signal level changing up to a factor of four between channelling and nonchannelling conditions, the ISI signal level up to a factor of ten for Cu.

Special care was taken in the observation of crystalline silicon. Due to its fragile structure, the detection of channelling effects in silicon is much more of a challenge than in metals. With very short observation times, contrast reversals due to ion-channelling, at room temperature, could be documented (Fig. A2-22). Also documented has been the loss of contrast due to lattice amorphisation and the amorphisation dose (Fig. A2-23). Another form of crystallographic contrast in Si has been detected. It is due to the preferential oxidation of exposed (111) planes (Fig. A2-24). The SIM is particularly sensitive to this effect, in comparison with the SEM (Fig. A2-25).

Ion-channelling effects on the sputtering rates for Cu and Si have been probed by ion-beam writing across crystallite boundaries (Figs. A2-26 and 27). Quantitative results have been obtained on the crystal orientation dependence of writing speeds.

In conclusion, SIM observations have been shown to represent a method for the sensitive detection of crystalline structures. In addition, these observations have implications in connection with the conduct of microanalysis by SIMS. The large variations in the ISI yields with crystal orientation, due to ion-channelling, will have direct bearing on the interpretation of SIMS elemental maps of crystalline materials.

2.3 Accomplishments under Task 3: New ion microprobe development, design and construction.

This complex task has been brought to a successful conclusion during an additional fourth year of the program, rather than at the end of the third year, due to a nine month delay in the delivery of the microprobe vacuum chamber on part of Torr Vacuum Products. Nevertheless, most of the original design specifications have been met.

a). Optical column design. The original UC preliminary optimization of the column design for the new microprobes has been considerably extended at HRL, much along the lines set forth in the correspondence between the Principal Investigator and Dr. J. H. Harris and B. A. Wilcox of NSF, in answer to several comments and suggestions on the part of the NSF referees. Particular attention has been given to explore optimal configurations for longer working distances and larger demagnifications than previously considered. By and large, the new exploration has confirmed the soundness of the basic design originally proposed.

The column was designed so as to:

o Decouple the source extraction voltage from the final probe voltage.

o Maintain a fixed object and image position while varying source and probe voltages over an extended range.

o Minimize the chromatic aberration of the column.

o Provide a crossover where a small aperture could be placed without affecting the transmission of the column. Such an aperture would stop a large fraction of the residue of nonfocused, neutralized and energy degraded beam particles that may originate in the source region.

Figure A3-1 shows a schematic drawing of the two-lens electrostatic focusing column. The first lens (nearest the tip) is an asymmectric lens which first decelerates and then accelerates the beam to the final energy. This lens images the emitting tip to form an intermediate crossover. The final lens serves to demagnify the intermediate crossover formed by the first lens to provide the focused beam spot. Lens aberrations and column performance were calculated for a tip-lens distance of 1.6 cm and a total column length of $\sim$ 21 cm. For all these calculations the intermediate crossover was maintained 2 cm downstream of the first lens by suitably adjusting the intermediate electrode potential V_1. It was found that the initially decelerating mode ($V_1 < V_{EXT}$) for the first lens provided the best overall performance.

Since the focusing column was designed to operate with both gas-field ionization (GFI) and liquid-metal ion (LMI) sources, the analyses included both cases. The GFI source has a relatively low energy spread ($\sim$ 2 eV). The extraction voltage can vary from 5 to 30 kV depending on the radius of the field-emitting tip. Figure A3-2 shows the calculated spot size for the GFI source. The spot size is limited by diffraction at small acceptance angles ($\alpha_1 < 5 \times 10^{-4}$ rad) and by chromatic aberration for large angles. Minimum spot size occurs at $\alpha_1 \sim 8 \times 10^{-5}$ rad which corresponds to an expected current of 2×10^{-14}A; the spot size is not sensitive to V_{EXT} provided the first lens is adjusted appropriately. Minimum spot size is attained for the smallest working distance (1.2 cm) as expected. However, d_{SPOT} only increases by $\sim$ 2x when the working distance is increased to 5.6 cm. This latter condition was thought to be required for reflection spectrometry techniques where an energy analyzer is placed between the final lens and the specimen.

LMI sources typically emit heavy ions which sputter a specimen yielding characteristic secondary ions and electrons. The extraction voltage range is 5 to 10 kV, and an energy spread of 10 eV is common. Figure A3-3 shows the calculated spot size for an LMI gallium source. The virtual source size is not well known for LMI sources and was assumed zero in these calculations. The diffraction limit is at $\sim 10^{-5}$ rad for the heavier ions, and again chromatic aberration is limiting at larger values of α_1. Minimum spot sizes occur at $\sim 1.5 \times 10^{-5}$ rad, where the expected spot current would be $\sim 2 \times 10^{-14}$ A. It was anticipated that a larger working distance (5.6 cm) for SIMS with LMI sources would be used.

An update of these projections, based on the actual operating parameters of the microprobes, will be shown in relation to Task 4: Performance Evaluation, and compared with the initial calibration data.

page 8

b). <u>New ion microprobe system design: Summary</u>. After extensive deliberations by both HRL and UC investigators, a final design has emerged for the overall microprobe system, which incorporates the optical column design discussed under (a) above. This is shown in Fig. A3-4. A liquid metal (LMI) ion source is shown here, although the microscope is designed also to allow the use of a gas field ionization (GFI) source. The asymmetrical lens focuses the ion beam to a crossover located at the center of the differential pumping aperture which isolates the source vacuum chamber from the specimen vacuum chamber. This aperture is connected to a picoammeter to facilitate optical alignment of the source with the column. An octupole deflector upstream of the crossover aperture can be used to image the crossover aperture. After passing through this aperture, the beam is deflected by two electrostatic octupoles and finally focused onto the specimen by an einzel lens. In this configuration, the focused spot formed by the two-lens optical column is scanned across the specimen's surface by double-deflection. With such a system, the beam undergoes a rocking motion pivoted at the center of the einzel lens, thus minimizing off-axis geometrical and chromatic aberrations. A pair of channel multiplier detectors collect either <u>ion</u> induced <u>secondary</u> <u>electrons</u> (ISE) or <u>secondary</u> <u>ions</u> (ISI), emitted by the target under bombardment by the ion probe. Between the einzel lens and the specimen is an energy analyzer and transport system to collect and transmit secondary ions of selected energy to the entrance of a SIMS quadrupole mass filter. This ISI collection system will be described in further detail below, since it represents one of the determining factors in the unusual performance of the SIMS system of the UC-HRL SIM. The beam-defining aperture at the entrance to the accelerating (asymmetric) lens determines the beam half-angle, α_1, at the source and also the current in the probe, proportional to α_1^2 in this chromatic-aberration-limited system. Up to twelve specimens may be loaded into the microprobe specimen stage at one time, using an inserter system developed at HRL.

Except for the extraction and lens voltages, all of the optics and image display functions are controlled by a Z-80 based microcomputer. Control data is input to this computer from the keyboard and joystick shown. Images and SIMS data are then displayed on the two oscilloscopes and TV monitor.

Several views of the microprobe system installed at UC are shown in Figures A3-5 and 6.

c). Details of microprobe subsystems. The twin UC and HRL microprobes consist each of several main subsystems. These include vacuum system, ion source, optical system, detection and SIMS system, isolation transformers for power conditioning, high voltage electronics rack, control and display electronics rack. The overall ion microprobe layout is shown in Fig. A3-7.

Vacuum Chamber. The SIM vacuum chamber layout is shown in Fig. A3-8. Its realization has already been illustrated in Fig. A3-6. The entire vacuum system is bakeable and has met the vacuum design specifications of 5×10^{-10} Torr before being accepted from the manufacturer. The system is evacuated first by three sorption pumps, subsequently by two 450 l/s ion pumps. The entire assembly is supported on vibration isolation air legs. Viewing ports overlook the ion source and the specimen region respectively. The ion source is mounted on a liquid N_2 dewar, partially shown on top of the column, which will be used in conjunction with GFI sources. A specimen inserter enables loading of 12 samples on a carousel stage, provided with x, y and z motions. The SIMS system is inserted in the specimen chamber from a port on the rear side of the chamber. A side view of the SIM, showing the high voltage lens feedthrough is also shown in Fig. A3-6.

Ion Source. A completed liquid metal ion source assembly is shown in Fig. A3-9, along with a close up of the source tantalum housing and extraction aperture. The source is shown here inverted from its orientation in the microprobe, in which it extends down from the 4.5" O.D. UHV flange. The large insulator can withstand the full 60 kV accelerating voltage of the beam. At the lower end of this insulator a copper block forms the base on which the LMI source assembly is mounted. Adjustment screws allow the extraction electrode to be centered with respect to the top of the liquid metal source. The entire source assembly can then be moved along the x-y axes to align it with the optical column shown in Fig. A3-11. Two stainless steel jaws grip the LMI source from each side, providing both mechanical support and the electrical connections to the heater ribbon. The extraction electrode, normally a few kilovolts less positive than the source, is supported by the cylindrical Macor insulator shown in the close-up view of Fig. A3-8.

Figure A3-10 is a close-up of the liquid metal source in Figure A3-8 with the extraction electrode and its insulator removed. The liquid metal source itself is now visible as well as the two mounting jaws. These jaws are contained within the stainless steel cylinder which is mounted on the copper base block. The gas field ionization source looks very similar to the LM

source shown here, except that provision is made for the controlled supply of hydrogen gas to the source tip and a liquid nitrogen dewar is used to cool the source assembly to near 77° K.

Optical Column. Figure A3-11 shows the layout of the optical column, which is mounted below the ion source in the main vacuum chamber. Before insertion into the system, the column is assembled on the air-bearing rotary table shown in Figure A3-12, which allows highly accurate alignment (to 0.000001 in.) of each lens electrode. The larger white insulators seen here can stand off 60 kV, while the smaller insulators are designed for 30 kV. The large plate at the center serves as the main support for the column as well as the differential pumping barrier between the upper part of the chamber (source side) and lower part of the chamber (specimen side). The fairly short overall length of the column (desirable in reducing the effects of stray magnetic fields) is evident.

Probe Deflection System. Both deflection octupoles are contained in the housing mounted below the main mounting plate at the center of the optical column. Figure A3-13 is a combined illustration of the completed octupole assembly for the UC microprobe and the parts for the HRL octupole. The octupoles are of unequal length (upper 1.062/2; lower 2.000 in.) since a proper double-deflection scan through the center of the einzel lens requires an upper/lower strength ratio of 1.062/2. Each individual element is accurately machined and highly polished. The two sets of eight elements have been carefully assembled under clean conditions and adjusted to achieve precise alignment axially, radially, and tangentially by means of 32 mounting screws on each octupole (4 per element, 64 in the completed assembly).

Specimen Stage. The specimen stage in Figure A3-14 is mounted on an 8 in. O.D. UHV flange at the front of the main vacuum chamber. Three orthogonal x, y, z motions of ± 1 cm are provided along with rotation of the specimen turret to each of 12 positions. At the far right a single specimen holder can be seen. In normal operation, up to 12 new specimens may be interchanged with 12 old specimens in a single loading of the vacuum interlock. The inserter system is isolated by a gate valve from the main vacuum chamber.

Detection and Imaging Instrumentation. The two-channel electron multiplier (CEM) detectors (Fig. A3-4) overlooking the target region provide a signal containing information on the surface topography and/or the material contrast in either ISE or ISI imaging. For ISE collection, a positive voltage bias (0 - 300 V) is applied to the CEM, relative to the target. Higher acceleration

is required for ISI detection with good efficiency. This is accomplished by bringing the CEM to a negative potential of - 3000 V relative to the target.

Much as done in our previous work with the prototype UC-SIM, the signal pulses from the CEM's can be handled in two different ways for imaging purposes. In the pulse-mode, individual pulses are amplified, shaped and displayed as counts on the CRT. This mode is appropriate for counting rates less than a few MHz. In the analog display, the CEM pulses are processed through an analog amplifier to yield continuous-tone video images on the CRT. The digital raster size and dwell time per pixel can be varied over a wide range to provide rapid scans for visual focusing, astigmatism correction and specimen searching, as well as single-pass high resolution scans for image recording. The CRT used has a resolution of 1024 lines. Images 7×7 cm^2 are recorded on Polaroid film in single pass scans, typically 33 sec. long.

SIMS System. A fundamental component of the UC-HRL SIM is the ISI energy analyzer and transport system (ATS), located between the target and the entrance to the RF quadrupole mass filter, as shown schematically in Fig. A3-4. To improve on the commercially available units (Bessel box, Sphericel), which have low transmission and would not fit the geometry of our microprobe, a special system was designed by UC-HRL. The secondary ions emerging from the target are first accelerated and energy analyzed by a 90° cylindrical electrostatic prism. A transport system subsequently focuses the transmitted ions, after deceleration, so as to match the acceptance requirements of the RF quadrupole. A miniaturized construction (2 cm thick) was required for this entire system, so as not to unduly increase the working distance of the final lens of the microprobe, with consequent loss of resolution. The ATS assembly was fabricated at UC, its design as shown in Fig. A3-15, and a view of its arrangement relative to the two CEM detectors on the front plate of the einzel lens is shown in Fig. A3-16.

A heated filament within the transport system can be used to ionize the residual gas by electron bombardment, to use the SIMS as a residual gas analyzer (RGA). A potentiometric voltage divider and two 0 - 300 V power supplies provide for 12 voltages required to operate the ATS. In the configuration presently in use, the secondary ions within an energy window 10 eV wide are transported to the RF quadrupole, with a calculated transmission of $\sim$ 10%.

The RF quadrupole mass filter is a conventional unit supplied by Extranuclear Laboratories, Inc. (Fig. A3-17). The small cylinder at the left is the original energy analyzer, replaced in our design by the ATS system

page 12

described above. The center cylinder contains the rf/dc quadrupole proper, while the channel electron multiplier detector is contained in the third cylinder attached to the 6 in. O.D. UHF flange at the far right. This complete assembly is mounted on the vacuum system with an 8 in. bellows. At UC, elemental maps are obtained using the pulse-mode display electronics of the SIM, with a raster size of 1024 lines. Mass spectra are accumulated on a multichannel scaler (MCS) and printed on a chart recorder. At HRL, maps are displayed on the CRT using an analog video system.

Power Supplies. All electrical power is fed from two isolation transformers to the high voltage rack in Figure A3-18, and from there to the rest of the instrument. The high voltage rack contains two 450 l/s ion pump controllers which mount in the base of the rack, at ground potential. A 0-30 kV high voltage supply in the base sets the voltage of the lower of the two inner boxes of the rack. A floating 0-30 kV supply in this lower box then determines the potential of the upper box, which is also the final beam energy. Within the upper box are the extraction electrode, accelerating lens, and einzel lens power supplies shown schematically in Figure A3-4.

Microprobe control electronics. All of the microprobe electronics not at a high voltage are contained in the control and display rack of Figure A3-5. On the right are the SIMS control electronics, which include the quadrupole and ATS controls. Just below the shelf are the two octupole power supplies and the quadrupole high voltage supply. The octupole amplifiers, which must be separated from these power supplies for shielding purposes, are mounted at the top of the rack. On the left is the Z-80 based microcomputer box, the dual floppy disk drivers, the dual TV monitors (left for control parameters, right for computer-processed images), and the main keyboard for operating mode selection and data entry. The center rack contains, in addition to the lower octupole driver and power supply, the buffer-combine-invert box (containing all the analog electronics for the scans), and the Tektronix #5110 and #606A oscilloscopes for real-time image display. Visible on the shelf is the mode keyboard-joystick box for data entry into the microcomputer.

To control all the different operating parameters of the machine, 36 different operating modes may be selected by means of 16 keys on the right of the main keyboard and 20 keys on the joystick box. Once a mode has been selected, data is either entered from the keyboard or the joystick. As the operating parameters are changed, the screen display is constantly updated. The operating modes consist of the specimen x-y d.c. position (constant

displacement of scanning raster), stigmators, alignment d.c. offsets, channel-
tron voltages, time/pixel and number of pixels/line (also lines/picture), type
of scan, magnification, raster rotation, upper/lower octupole strength ratio,
coefficients for real-time combination of all three different signals de-
tected by the microprobe, video amplifier gains and bias, and controls for
the SIMS energy analyzer and mass command (selects which ion mass passses
through the rf/dc quadrupole). Additional operating modes allow the storage
and retrieval of parameter data and advanced image and SIMS data processing.

2.4 Accomplishments under Task 4: Performance evaluation of new ion microprobes.

The study of the optical column performance was initiated at UC in
November 1983 using a Ga^+ LMI source. The SIMS system began operating at UC
in April 1984. The HRL copy began operating shortly afterwards. Notwithstanding
the late start of this phase of the program, a remarkable amount of information
has already been collected on the performance of the microprobe. Preliminary
results pertinent to this phase of the program have been presented in public-
ations (a) 17 and 19.

a). Focusing performance. The early phase of this task involved the elimina-
tion of external disturbances which affected the operation of the probe. The
specimen stage proved inadequate for high resolution work due to resonant
vibrations of spring-loaded platforms. The vibration was eventually reduced
to acceptable levels by establishing solid mechanical contact between the stage
and the front lens of the optical column. Unacceptable RF noise pickup was
eliminated after a painstaking identification of ground loops in the complex
wiring of the microprobe control system. A new set of calculations of the
expected probe diameter d_p as a function of the beam acceptance angle at the
source α_0, was performed to correspond to the actual operating parameters of
the microprobe system, which differed somewhat from the original idealized
case treated previously. Curves for probe voltages 30 and 50 kV and for two
hypothetical choices of the virtual size of the source at 10 and 50 nm are
shown in Fig. A4-1. Clearly, a complete evaluation of the microprobe per-
formance would entail the exploration of its spot size for a large number of
settings of the beam defining aperture, which in turn determines the acceptance
half-angle α_0.

Thus far the operation of the column has been investigated with beam
defining apertures of 25 and 12.5 μm, defining source half-angles of 0.78 and

0.38 mr. The spot size (FWHM) for these aperture settings, at 40 kV, have been measured as 90 and 45 nm respectively by sputter-etching grooves in Au-coated Si wafers (Fig. A4-2). The two experimental points for d_p are seen to fit the calculated performance of Fig. A4-1 rather well. By futher restricting the defining aperture size, it will be feasible to investigate the limiting SIM resolution at least to the 10 nm level.

The probe current I_p has been measured by targeting the beam on a deep Faraday cup, so that no ISE contribution is included. An example of the time evolution the probe current I_p and source current I_s for a Ga LMI source, at constant extraction voltage, is shown in Fig. A4-3a. I_s generally decays much faster than I_p. The probe transmission becomes particularly efficient at total emission currents below $\sim$ 2 μA. This is further illustrated (Fig. A4-3b) by plotting the transmission ratio I_p/I_s, proportional to the inverse of the source solid angle of emission $1/\Omega_s$, vs. I_s. These data quantify previous observations of the expansion of the emission cone of LMI sources with increasing I_s. Typical probe currents at probe diameters of 90 and 45 μm are 40 and 10 pA respectively.

b). Imaging performance. The most immediate approach to the optimization of the optical column performance obtains through imaging of objects at various magnifications. Thus, a large number of micrographs is available to document the progress in the fine-tuning of the probe, and in the overall performance of the display system. Figs. A4-4 through 14 contain a vivid demonstration of the instrument's ability to image a variety of objects, using either pulse-mode or analog display, and ISE or ISI signals over a range of magnifications from $\sim$ 40x to 4000x. These observations have been patterned after the previous study of SIM imaging, carried out with the prototype UC-SIM and described under Task 2.

c). SIMS performance. The initial operation of the SIMS system has been extremely successful. Positive ions have been analyzed so far. Some high voltage feedthrough modifications are being implemented to operate the SIMS with negative ions. The calibration of the RF quadrupole mass filter has been performed by operating the system as a residual gas analyzer. This is accomplished through an ionizer filament in the ATS, as described under Task 3. Residual gas mass spectra are shown in Fig. A4-15. Shown in Fig. A4-16 is the spectral line shape for the two Ga isotopes, at a mass resolution M/ΔM of $\sim$ 850. Mass spectra of metallic glass, superconducting wire, a stony meteorite and a passivated integrated circuit are shown in Figs. A4-17 and 18.

The spectrum of a GaAs substrate, obtained at HRL, is shown in Fig. A4-19.

Although a Ga^+ probe is not expected to enhance the secondary ion yields for either sign of the secondary ion charge, the results thus far obtained, even without oxygen flooding of the sample, are surprisingly good. At the probe current density of ~ 1 A/cm^2, the initial O_2 coverage of a sample is adequate to yield several high spatial resolution maps 25 x 25 μm^2 in size, each with 10^6 pixels, before oxygen depletion seriously affects the ISI yields. In any case an oxygen jet is presently being installed to provide sufficient O_2 replenishment during prolonged observations.

Elemental maps have been obtained of a variety of samples, including integrated circuits in Si and GaAs, silicate minerals and glasses, metals and alloys and minerals of organic origin. Au-Pd coating of insulators has proven completely adequate in preventing sample charging. Alkali-metal-rich samples have yielded mass separated counting rates as high as 2 x 10^5 cps or 2 x 10^4 cps/pA of primary current, calcium in oxalates and apatite and magnesium in olivine and spinel rates of $\sim 10^3$ cps/pA.

This part of the performance evaluation task in effect overlaps several aspects of the last task of the program, dealing with exploratory research applications. For the present purposes, presented in this section are some of the results which are relevant to illustrate the lateral resolution which can be achieved in SIMS elemental mapping with the UC-HRL SIM. The conditions for high resolution mapping in SIMS have been explored in Publication (a) 19.

Figure A4-20 shows maps of Li^7 obtained from an Au-coated Si wafer, at x1800 and x3600 respectively. Similar maps have been obtained for K^{39}, suggesting the sample represents the residue of a detergent or etchant smear. Also shown are corresponding maps for Ga^{69}, self-sputtered after Ga^+ beam implant in the Au layer. Grains varying in size from a few micrometers to the limits of image resolution (~ 40 nm in the original micrographs) are clearly outlined in all maps, but many of the smaller grains did not survive the increased erosion rate of the x3600 scan.

Figure A4-21 shows maps of a section of Fermilab superconducting wire (Ti-Nb alloy wires embedded in a Cu matrix), for Cu^{63}, Ti^{48}, and Nb^{93}. The section was etched in HNO_3 to eliminate smears due to sectioning and polishing. Some of the Cu from the matrix seems to have diffused into the Ti-Nb wires, but not the reverse.

Maps for a Be-Cu section are shown in Fig. A4-22. The Na^{23} present is likely a residue of detergent.

Maps of a passivated integrated circuit are shown in Figs. A4-23, 24 and
25. These figures show the topography of the regions as seen through the
overall ISI signal. The presence of Ca^{40}, Na^{23} (and K^{39} not shown here)
suggests passivation with a soda lime glass at several stages of the multi-
layer structure built-up. Al^{27} metallizations on a Si or SiO_2-covered sub-
strate are clearly delineated.

2.5 Accomplishments under Task 5: Exploratory research applications.

In the course of the performance evaluation of the new microprobes,
several samples have been examined which pertained to areas of active research
and development. In such areas, the UC-HRL instrument has demonstrated ex-
tremely valuable new insights and the potential for unique diagnostic appli-
cations.

a). Structures and devices on GaAs substrates. Several uncharacterized
devices and structures on GaAs substrates, supplied by HRL, have been examined
by the UC microprobe. Figure A5-1 shows the topography and elemental maps of
a functional FET device, quite heavily passivated. A broad Si-implanted area,
corresponding to an exposed GaAs area which yielded a Ga signal, and Cr
metallizations are visible. The Ga signal is generally enhanced by the pre-
sence of metals heavier than Ga, due to backscattering and self-sputtering.

Although Au cannot be identified as yet, due to its extremely low posi-
tive secondary ion yield, its presence can be detected by an enhanced self-
sputtered Ga signal. This is evident in Fig. A5-2, where Au-coated pads
deposited on GaAs appear brighter in Ga maps, than the substrate. The Ti
contour of the FET gates is clearly delineated also. The Ga maps show the
presence of surface impurities on the GaAs substrate. In Fig. A5-3, the
underlying structure of FET devices has been exposed by prolonged ion beam
erosion. The Ga^{69+} map shows enhanced signal from the Au pads, and even
larger enhancement from the W-Ti gates. A map taken with the dimer Ga^{138+}
shows the Au pads even more clearly, but no signal emerges from the W-Ti gates.
This is an interesting example of matrix effects in molecular ISI emission,
which deserves further investigation. The Au-enhancement of the self-sputtered
Ga^+ signal has also been detected at HRL (Fig. A5-4 and 5).

b). SIMS studies of chondrites. The UC-HRL SIM/SIMS in emerging as an extremely
powerful new tool in the study of the microscopic structure and composition of
chondrites. Of particular interest are the rims surrounding chondrules.

Chondrules are small (1 micrometer to 4 nm) discrete, rounded silicate bodies that occur almost exclusively in the large class of stony meteorites called chondrites. They clearly represent primitive solar system matter that has undergone melting and rapid cooling--even quenching. Textures and mineralogies vary over a small range: olivine, troilite and many times silicate glass (containing Na, Al, Fe, Cr, Mg, Ca, Ti in varying amounts).

The exact origin of these chondrules is problematical, although there is a well established consensus that they are the result of early melting processes in the primitive solar system. Past studies have shown that after chondrules formed they accreted into asteroid-size bodies. Before accretion they remained for unknown lengths of time in a dusty and gaseous nebular cloud. During this period they acquired rimming coatings of different thicknesses (up to 50 micrometers).

The study of these rims has recently become a significant issue. Knowing the nature of the coating (composition and mineralogy), and any sequence of layers of varying composition will reveal the nature of the nebular medium surrounding them prior to accretion. The spatial resolution of the elemental maps obtained with the UC-HRL microprobe seems to provide the only means to examine their structure, since the grain-size of the minerals that comprise them appears to be in the range of only tenths of a micrometer. In a collaboration established with members of the cosmochemistry group at the University of Chicago (R. N. Clayton, L. Grossman, R. W. Hinton) anf the Field Museum of Natural History (E. Olsen), a preliminary study of feasibility has already been initiated. The initial results show tremendous promise, and these studies will become an area of concentration of further research with the new microprobe. A partial set of elemental maps for a chondrule rim in an unequilibrate chondrite is shown in Fig. A5-6. The Fe-rich rim is clearly resolved, and a glass coating (from the Na, K maps) of the chondrule is revealed. The chondrule itself appears as an aggregate of olivine bodies (Mg, Fe), cemented in alkali-rich glass. These are the first observations ever carried out with such detail and differentiation. Other chondrite areas are shown in Fig. A6-7, as seen through the Na^{23} and Mg^{24} windows. Again, the spatial resolution in these continuous-tone SIMS maps is exceptional. Another elemental survey of an inclusion in a carbonaceous chondrite is shown in Fig. A6-8. Here, the maps for two isotopes of Mg are compared, illustrating the potential capacity to detect large isotopic anomalies, such as are known to occur in meteorite inclusions of extra-solar origin.

c). Intercalated graphites. In collaboration with H. Wang of Bell Communications
Research (Murray Hill), and A. V. Crewe's Electron Microscopy group at UC,
preliminary SIM observation of $SbCl_5$-intercalated graphites have been carried
out.

Recent advances in the synthesis of graphite intercalation coumpounds,
coupled with current theoretical interest in two-dimensional physics, have
contributed to the current high level of interest in these coumpounds. Because
of their unusual ordering, intercalation compounds offer opportunities for
the study of new types of phenomena. For example, novel phase transitions
arise through the "staging" phenomenon, in which a constant number of layers
of host material are sandwiched between sequential intercalate layers. This
phenomenon gives a periodic array of intercalate sheets that can independently
undergo two-dimensional order-disorder and structural phase transitions. In
addition to these properties of fundamental interest in condensed matter
physics, a range of macroscopic properties, in particular the unique electrical
and thermal transport properties of these compounds, are attracting consider-
able attention toward a number of practical applications.

Somewhat paradoxically, the structure of intercalated graphite is better
known at the atomic level, through x-ray electron diffraction and transmission
electron microscopy studies, than it is at long range where domain structures
are expected to occur. For example, the Herold-Daumas model predicts pleated
structures across the lattice planes for a stage-2 material, defining regions
or domains of characteristic size. Such structures have not yet been observed
in e.g. $Sb-Cl_5$-intercalated single crystal graphite, although their existence
for domain sizes $\gtrsim 200\,nm$ has not been ruled out.

Other microdomain structures, accompanied by chemical segregation of the
intercalate, have been recently observed by H. Wang and collaborators in stage-4
$SbCl_5$-graphite. In this case, Sb-rich islands of lateral dimension 50 - 10 nm
have been directly observed with an analytical electron microscope, and their
composition deduced from energy dispersive x-ray spectra. Preliminary obser-
vations in the SIM of stage-4 and stage-2 $SbCl_5$-graphite have revealed striking
structures in secondary electron and ion images (Figs. A5-9 and 10) over a
range of sizes from tenths to several micrometers. A specimen of highly
oriented pyrolithic graphite (control), did not show any structure similar to
those in Figs. 9 and 10. Images of crystal structures from this specimen are
shown in Fig, A5-11. Whether or not the above observations may already be
examples of the Herold-Daumas domains remains to be demonstrated in a more

systematic and controlled program. Particularly important will be the chemical mapping for negative ions (Cl$^-$), which we will be able to perform in the near future. Here again, our instrument offers a tantalizing preview of results which could represent a breakthrough in the field.

d). Biological applications. The UC-HRL SIM/SIMS is already contributing to significant discoveries in the biomedical field. In a collaboration with D. A. Bushinsky, F.L. Coe and S. Deganello, of the UC Department of Medicine, a research program has been initiated using the new microprobe in the study of biomineralization. The crystallographic contrast of SIM images, and the high spatial resolution SIMS maps, reveal the structure of, and the calcium distribution in, e.g. kidney stones (Figs. A5-12 and 13) with unprecedented detail. The study of the skull bone of neonatal mice is decoding the onset of calcification in bone, and the extraordinary role of sodium and potassium in bone formation (Figs. A5-14 and 15). Experiments are planned making use of stable isotopes (e.g., K^{41}, Ca^{44}) as tracers of bone development. The present resolution of the UC-HRL SIM/SIMS already represents a twenty-fold improvement over the current state of the art.

e). Materials studies of eutectic alloys with applications to liquid metal
 ion sources.   A   proposed microanalytical application at HRL of the new microprobe   was   to study eutectic alloy liquid metal ion sources, a key element in the development at HRL of a scanned focused ion beam implantation capability for fabrication of ultra-submicron device geometries. Figures A5-16 and A5-17 illustrate the difficulty in developing long-lived alloy sources. As the SEM photographs in Figure A5-16 show, the Re tip which forms the substrate for the B-Pt alloy is initially smooth. After use in a three-lens column at HRL to dope silicon wafers with boron (the platinum is discarded by an ExB filter), the tip material has been eroded away, as can be seen in Figure A5-17. SEM photographs can show the surface topography of both used and unused sources, but elemental imaging, such as that possible with SIMS, is necessary to trace regions of B, Pt, and Re in order to determine the degrees of Re alloying into the initial B-Pt two-component system. Possible separation of the B-Pt alloy into regions of pure B or Pt or possibly B-Re and Pt-Re, could also be observed. Preliminary SIMS mapping of Pt with the UC-HRL SIM/SIMS shows that indeed, Pt does not cover the source needle uniformly, but has migrated up the shank and is not present in the apical region of the tip (Fig. A5-18).

f). Microfabrication and microlithography applications. At HRL, the new
microprobe is being applied to the microfabrication of structures by focused
ion beam exposure of resists. Figures A5-19 and A5-20 show high aspect ratio
(5 - 8) structures obtained by implanting 40 keV Ga^+ ions ($8 \times 10^{12}/cm^2$) into
a double layer resist on Si, and subsequently removing the unexposed areas
by reactive ion etching (RIE). The Ga-implanted layer on the surface of the
resist acts as an etch-stop to the subsequent RIE. The final width of the
unusual structures thus obtained is $\sim$ 100 nm.

At UC, the concentrated effort on the microanalytical applications of the
SIM has taken priority over microlithographic experimentation. On the other
hand, significant results in this area have been obtained using the prototype
UC-SIM. It has been found that the silicon, when implanted with doses of
gallium in excess of 10^{13} ions/cm^2, experiences little or no etching in aqueous
caustic solutions. With the 40 - 50 keV Ga^+ ion beam of the prototype UC-SIM,
(50 - 100 nm spot diameter), it has been possible to fabricate structures with
100 nm features. The silicon behaves as a negative resist with a sensitivity
of about 1 $\mu c/cm^2$. The etch stop process is largely insensitive to crystallo-
graphic orientation, except for the highly insoluble (111) plane in which
damage-induced etching occurs. Several examples of gratings, square grids,
and dot patterns obtained by this novel approach, are shown in Fig. A5-21 through
28. These results are described in Publication (a) 16, and an invention dis-
closure has been filed. A similar effect has been shown to occur also in glow-
discharge-deposited amorphous silicon. A Fresnel zone plate obtained by this
method is shown in Fig. A5-29.

A collaboration with scientists at LTV Aerospace and Defense Company is
being organized toward applications of this method of microlithography to
the fabrication of short wavelength infrared filters.

3. Cumulative Chronological List of Written Publications in the Technical Journals

(a) Published and in press

1. H_2^+ Traversing Ultra-Thin Carbon Foils: Measurements of Recombination Yields at 12.5 and 25 keV/amu.
   T. R. Fox; Nuclear Instruments and Methods 179 (1981) 407-10.

2. Molecular States from 25 keV/amu H_2^+ Traversing Ultra-Thin Carbon Foils.
   R. Levi-Setti, T. R. Fox and K. Lam; Annals of the Israel Physical Society, 4 (1981) 127-129.

3. H_2^+ Traversing Ultra-Thin Carbon Foils: Exiting Molecular States at 12.5 and 25 keV/amu.
   T. R. Fox, K. Lam and R. Levi-Setti; Nuclear Instruments and Methods, 194 (1982) pp. 285-289.

4. H_2^+ Traversing Ultra-Thin Carbon Foils: Cluster Effects in the Energy Loss at 12.5 and 25 keV/amu.
   R. Levi-Setti, K. Lam and T. R. Fox; Nuclear Instruments and Methods, 194 (1982) pp. 281-284.

5. Scanning Microscopy with Gallium Ions from a Liquid Metal Source.
   K. Lam, T. R. Fox and R. Levi-Setti, Proc. 28th Int'l Field Emission Symposium, eds., L. Swanson and A. Bell (The Oregon Graduate Center, Beaverton, Oregon, 1981) pp. 59-61.

6. Magnetic Prism Analysis of a Practical Gallium Ion Probe from a Liquid Metal Source.
   K. Lam, T. R. Fox and R. Levi-Setti, Proc. 28th Int'l Field Emission Symposium, eds. L. Swanson and A. Bell (The Oregon Graduate Center, Beaverton, Oregon, 1981) pp. 92-94.

7. Ion-Channelling Effects in Scanning Ion Microscopy with a Ga^+ Probe.
   R. Levi-Setti; Symposium paper, Proc. of the United States-Japan Seminar on Charged Particle Penetration Phenomena: "Charge States and Dynamic Screening of Swift Ions in Solids," Honolulu, Hawaii, Jan. 1982, ORNL CONF-820131, pp. 115-130.

8. Ion-Channelling Effects in Scanning Ion Microscopy and Ion Beam Writing with a 60 keV Ga^+ Probe.
   R. Levi-Setti, T. R. Fox and K. Lam; Proc. SPIE Conference on Submicron Lithography at Santa Clara, Calif., March 1982, Vol. 333, (1982), pp. 153-162.

9. Secondary Electron and Ion Imaging of Crystalline Materials with a 60 keV Ga$^+$ Scanning Ion Microscope.
    R. Levi-Setti, T.R. Fox and K. Lam; Proc. Tenth Int. Conf. on Electron and Ion Beam Technology, The Electrochemical Society, Inc., Montreal, Canada, May 1982, Extended Abstracts, Vol. 82-1, pp.462-463.

10. Ion-Channelling Effects in Scanning Ion Microscopy with a 60 keV Ga$^+$ Probe.
    R. Levi-Setti, T.R. Fox and K. Lam; Nuclear Instruments and Methods, 205 (1983) 299-309.

11. Crystallographic Contrast with a 60 keV Ga$^+$ Scanning Ion Microscope.
    R. Levi-Setti, P.H. La Marche and K. Lam; Proc. 29th International Field Emission Symposium, Göteborg, Sweden, August 9-13, 1982. Almqvist & Wiksell Int., Stockholm, 1982, pp. 417-424.

12. Heavy Ion Probes Play Significant Role in SIM Development.
    R. Levi-Setti
    Industrial Research and Development, September 1982, pp. 124-130.

13. Crystallographic Contrast Due to Primary Ion Channelling in the Scanning Ion Microscope.
    P.H. La Marche, R. Levi-Setti and K. Lam; Proc. Seventh Int. Conference on Applications of Small Accelerators, Denton, Texas, Nov. 1982. IEEE Transactions Nuclear Science, NS 30 (1983), pp. 1240-1242.

14. Secondary Electron and Ion Imaging in Scanning Ion Microscopy.
    R. Levi-Setti; Invited Review. Scanning Electron Microscopy SEM/83, I: 1-22.

15. Secondary Ion Imaging in the Scanning Ion Microscope.
    R. Levi-Setti, P.H. La Marche, K. Lam, T.H. Shields and Y.L. Wang. Nucl. Instr. and Methods, 218 (1983), 368-374.

16. Focused Ion Beam Microlithography by an Etch-Stop Process in Gallium-Doped Silicon.
    P.H. La Marche, R. Levi-Setti and Y.L. Wang; J. Vac. Sci. Technol. B 1 (1983), 1056-1058.

17. Initial Operation of a New High Resolution Scanning Ion Microscope.
    R. Levi-Setti, P. H. La Marche, K. Lam and Y. L. Wang; Proc. SPIE, 1984 Santa Clara Conference on Microlithography, Vol. 471, 74-82.

(a) Continued Publications

18. Amorphous Silicon as an Inorganic Resist.
    P. H. La Marche and R. Levi-Setti; Proc. SPIE, 1984 Santa Clara
    Conference on Microlithography, Vol. 471, 60-65.

19. High Spatial Resolution SIMS with the UC-HRL Scanning Ion Microprobe.
    R. Levi-Setti, Y.L. Wang and G. Crow. Invited paper presented at the
    31st Int. Field Emission Symposium, Paris, 1984. J. Physique, in
    press.

(b) Theses

1. Hydrogen Ion-Solid Interactions Near the Bohr Velocity.
   Timothy R. Fox, Ph.D. Thesis, The University of Chicago, December 1980.

2. Energy Loss of Diproton Clusters in Carbon Below the Fermi Velocity.
   Kin Lam, Ph.D. Thesis, The University of Chicago, December 1984.

Interactions (Coupling Activities)

(a) Spoken papers presented at meetings, conferences, seminars.

1. Progress in the Development of a Field Ionization Scanning Transmission Ion Microscope.
   R. Levi-Setti, T.R. Fox and K. Lam
   Paper presented at the 38th Annual EMSA Meeting, Reno, Nevada, August 1980.
   Abstract in Proc. 38th Ann. Meet. EMSA, pp. 66-67, ed. G.W. Bailey, Claitor's Publ. Div., Baton Rouge, 1980.

2. Information and Dose in the Scanning Transmission Ion Microscope.
   T.R. Fox and R. Levi-Setti
   Paper presented at the 38th Annual EMSA Meeting, Reno, Nevada, August 1980.
   Abstract in Proc. 38th Ann. Meet. EMSA, pp. 232-3, ed. G.W. Bailey, Claitor's Publ. Div., Baton Rouge, 1980.

3. Same title as Publications (a) 2. Paper presented by R. Levi-Setti at the Bat-Sheva Seminar on Molecular Ions, Molecular Structure and Interaction with Matter; Israel, January 1981.

4,5. Same title as Publications (a) 3, (a) 4. Papers presented by R. Levi-Setti at the Ninth Int'l Conf. on Atomic Collisions in Solids, Lyons, France, July 1981.

6. Same title as Publication (a) 5. Paper presented by R. Levi-Setti at the 28th Int'l Field Emission Symposium, The Oregon Graduate Center, July 1981.

7. Same title as Publication (a) 6. Paper presented by T.R. Fox at the 28th Int'l Field Emission Symposium, the Oregon Graduate Center, July 1981.

8. Same title as Publication (a) 7. Invited paper presented by R. Levi-Setti at the United States-Japan Seminar, Honolulu, Hawaii, January 1982.

9. Phenomenology of Low Energy Hydrogen-Ion Transmission through Thin Solid Foils.
   Invited paper presented by R. Levi-Setti at the United States-Japan Seminar, Honolulu, Hawaii, January 1982. R. Levi-Setti also chaired one session at the Seminar.

10. Same title as Publication (a) 8. Paper presented by R. Levi-Setti at the SPIE Conf. on Submicron Lithography, Santa Clara, Calif., March 29-30, 1982.

11. Same title as Publication (a) 9. Paper presented by R. Levi-Setti at the Tenth Int'l Conf. on Electron and Ion Beam Technology, The Electrochemical Society, Montreal, Canada, May 9-14, 1982.

12. <u>Imaging and Crystallographic Contrast with a 60 keV Ga+ Scanning Ion Microscope</u>.
    R. Levi-Setti, K. Lam and T.R. Fox. Paper presented by R. Levi-Setti at the 10th Int'l Congress on Electron Microscopy, Hamburg, August 17-24, 1982. Conference Proceedings, pp. 231-232.

13. Same title as Publication (a) 11. Paper presented by R. Levi-Setti at the 29th Int'l Field Emission Symposium, Göteborg, Sweden, August 9-13, 1982.

14. Same title as Publication (a) 13. Paper presented by P.H. La Marche at the Seventh Int. Conference on Applications of Small Accelerators, Denton, Texas, Nov. 1982.

15. Same title as Publication (a) 14. Invited review presented by R. Levi-Setti at the SEM/83 Annual Meeting, Symposium on SIMS - Ion Spectrometry/Microscopy, Dearborn, Michigan, April 1983.

16. Same title as Publication (a) 15. Invited paper presented at the Sixth Int. Conf. on Ion Beam Analysis, Phoenix, Arizona, May 1983.

17. Same title as Publication (a) 16. Paper presented by P.H. La Marche at the 1983 Int. Symposium on Electron, Ion and Photon Beams, Los Angeles, June 1983.

18. Same title as publication (a) 17. Paper presented by R. Levi-Setti at the Santa Clara Conference on Electron Beam, X-Ray, and Ion Beam Techniques for Submicrometer Lithographies III. March, 1984.

19. Same title as publication (a) 18. Paper presented by R. Levi-Setti at the Santa Clara Conference on Electron Beam, X-Ray, and Ion Beam Techniques for Submicrometer Lithographies III. March, 1984.

20. Same title as publication (a) 19. Invited paper presented by R. Levi-Setti at the 31st Int. Field Emission Symposium, Paris. July, 1984.

4. Professional personnel associated with the research effort.

a). UC Personnel

R. Levi-Setti	-	Principal Investigator
T. R. Fox	-	Research Associate, 6/01/1980 to 3/31/82
P. H. La Marche	-	Research Associate, 5/01/1982 to 4/30/84
K. Lam	-	Graduate Student
Y. L. Wang	-	Graduate Student
T. H. Shields	-	Graduate Student

b). HRL Personnel

R. L. Seliger

N. W. Parker

W. P. Robinson

J. W. Ward

APPENDIX 1

DESIGN STUDIES CARRIED OUT

USING THE PROTOTYPES

UC-SIM AND HRL-SIM
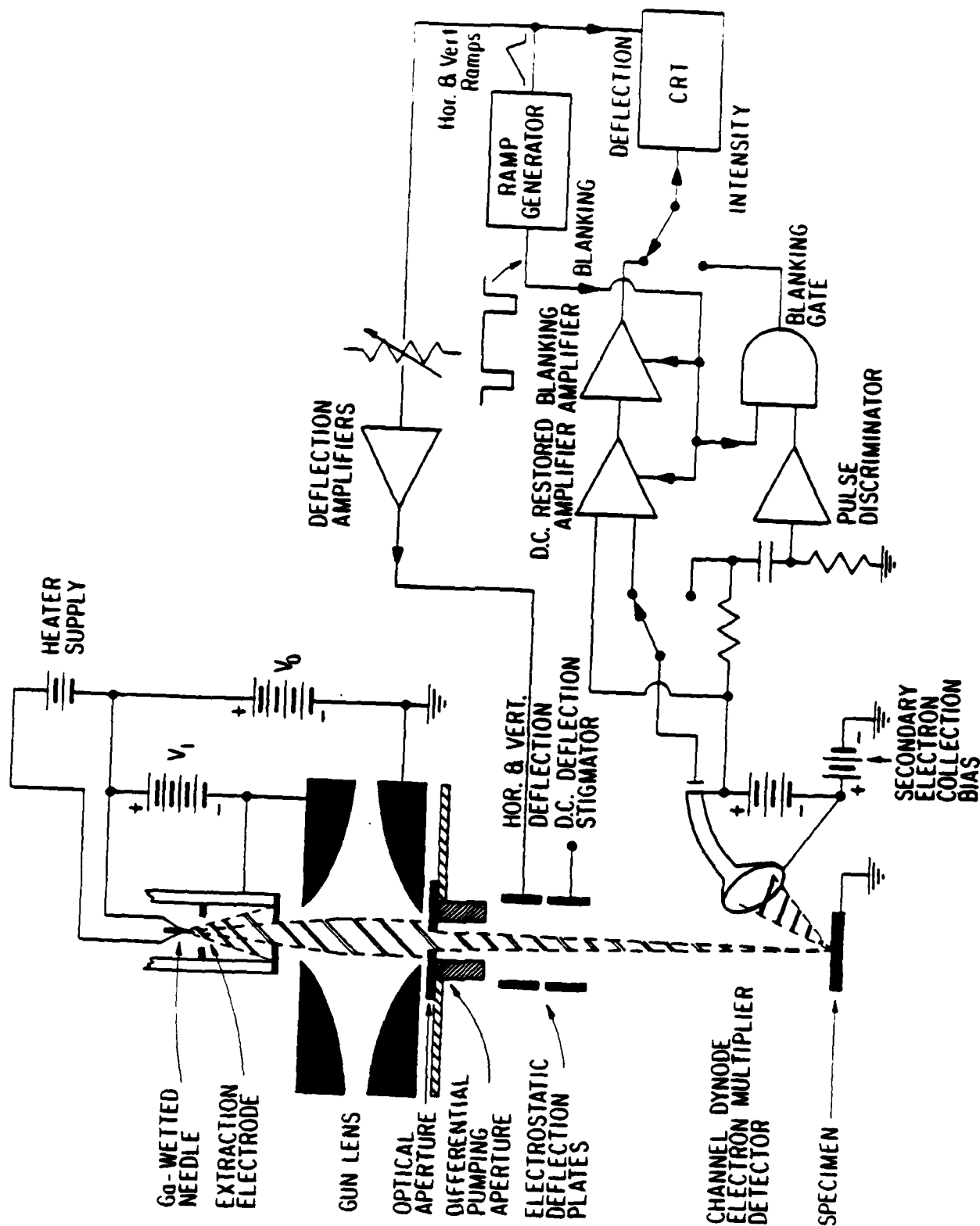
Fig. A1-1   Schematics of the prototype 60 keV UC-SIM.

GA$^+$ MOMENTUM SPECTRA

$^{69}_{35}$GA$^+$ $^{71}_{35}$GA$^+$

V_0 = 800 V

I_t = 2.1 μA

FWHM = 6.6 eV
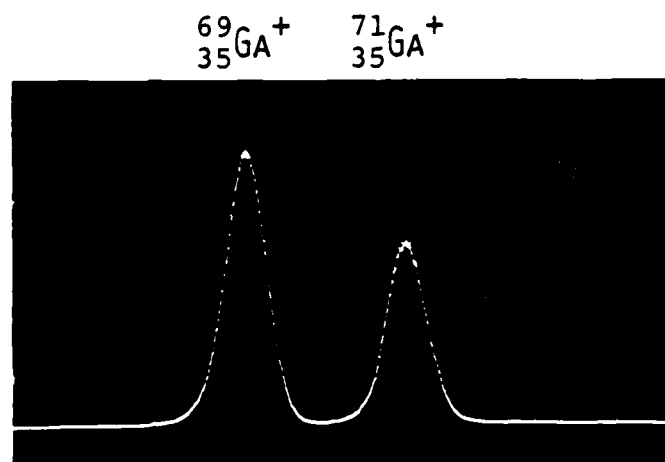
V_0 = 2000 V

I_t = 11 μA

FWHM = 21.4 eV
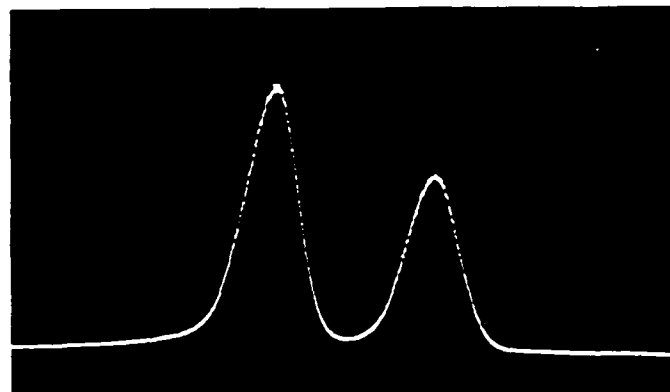
Fig. A1-2

Momentum analysis of gallium ion beam from an EHD liquid metal source installed in the UC-STIM. The gallium ions, extracted at 7 keV, are decelerated to 800 or 2000 eV respectively. The energy resolution is better than 1 eV. The ion energy spread is observed to increase with the source current.
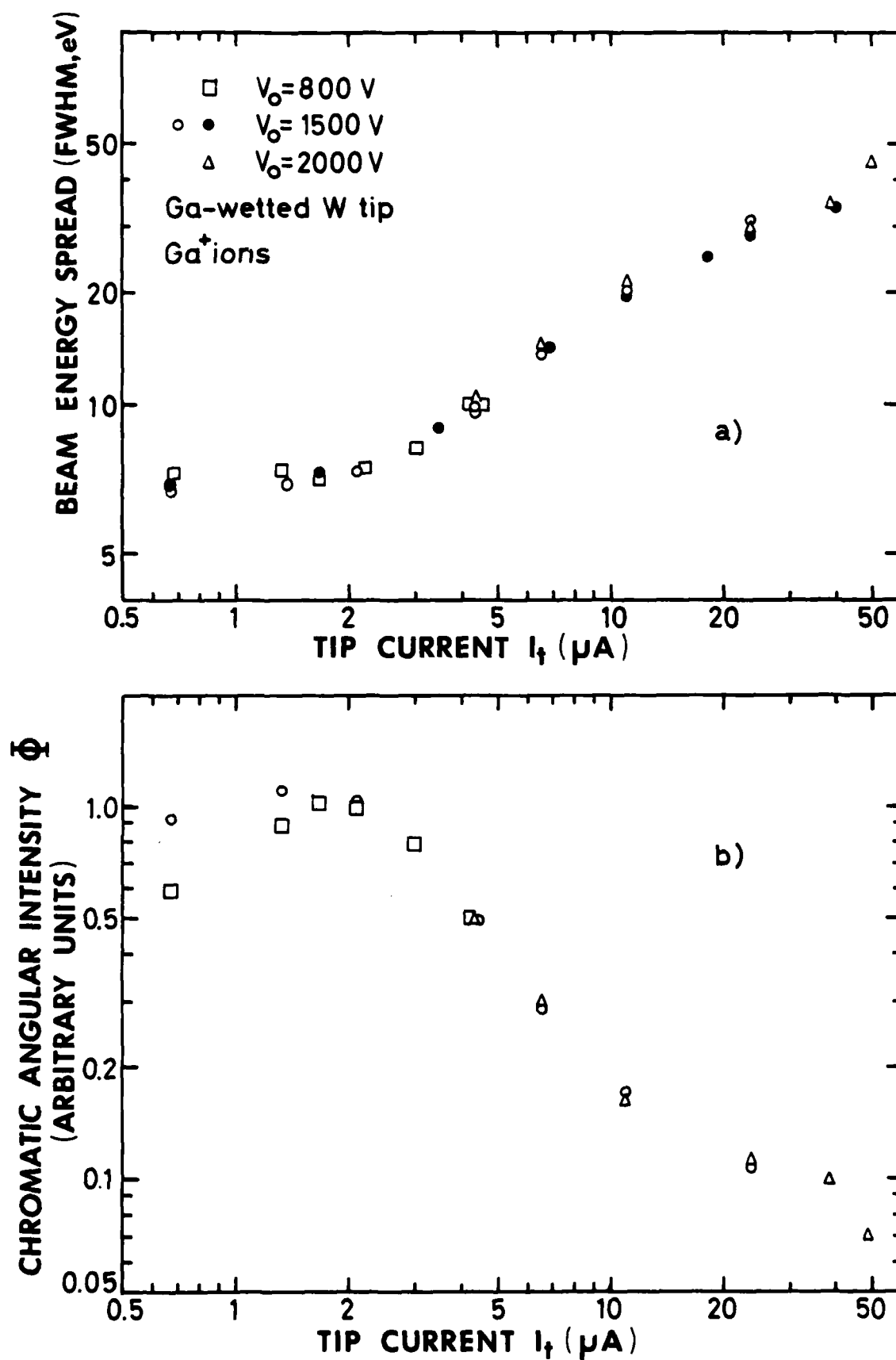
Fig. A1-3 a) Measured energy spreads of Ga$^+$ ions vs. tip current.
b) Normalized chromatic angular intensity Φ vs. tip current. In
a chromatic aberration-limited system, the probe current is pro-
portional to Φ.

GA+ FOCUSED-ION-BEAM IMAGES

INTEGRATED CIRCUITS

UC SIM. PULSE-MODE DISPLAY. FAST SCAN.
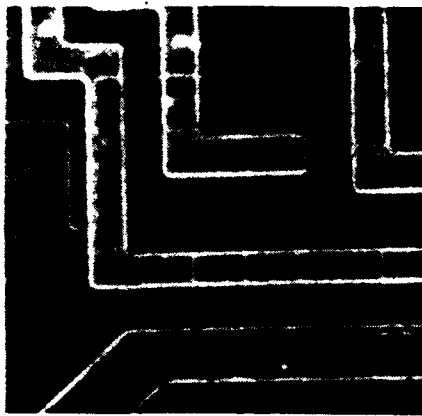
160 µM FULL SCALE.
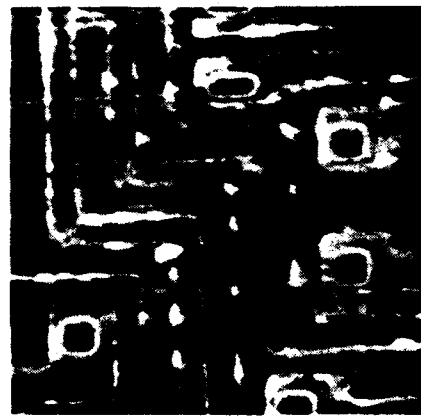
160 µM F.S.
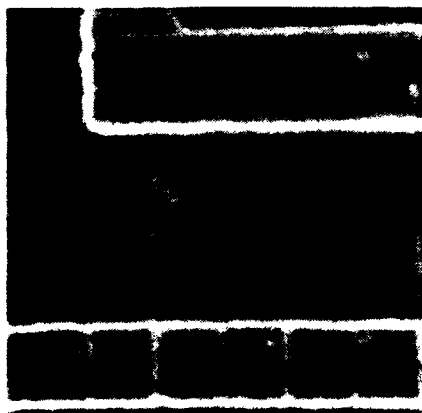
64 µM F.S.
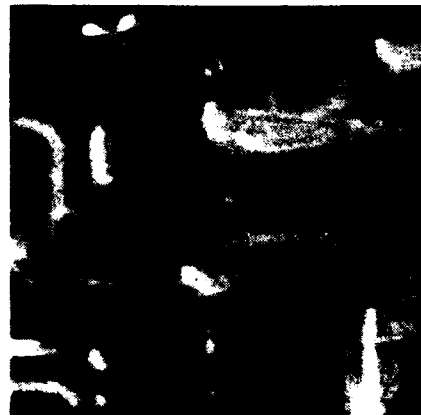
64 µM F.S.

GA$^+$ FOCUSED-ION-BEAM IMAGES
UNCOATED FOSSIL DIATOMS,
UC-SIM, PULSE-MODE DISPLAY, FAST SCAN
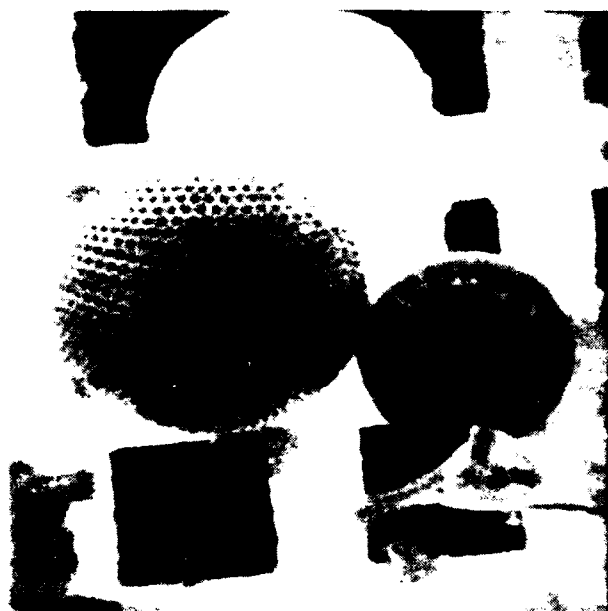
168 µM FULL SCALE

168 µM F.S.
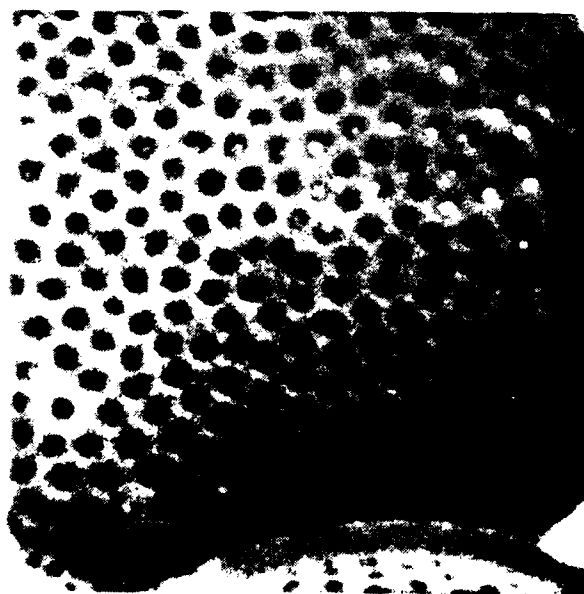
67 µM F.S.
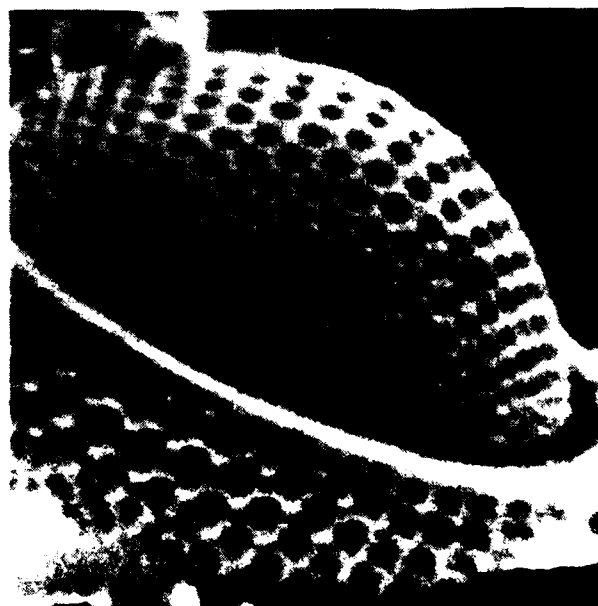
67 µM F.S.

GA$^+$ FOCUSED-ION-BEAM IMAGES
AG-COATED FOSSIL DIATOMS
UC-SIM. ANALOG DISPLAY. FAST SCAN

32 UM FULL SCALE

32 UM F.S.

16 UM F.S.

16 UM F.S.

Ga$^+$ FOCUSED-ION-BEAM IMAGES
UC-SIM. ANALOG DISPLAY. FAST SCAN

Ag CRYSTALS   FOSSIL DIATOM
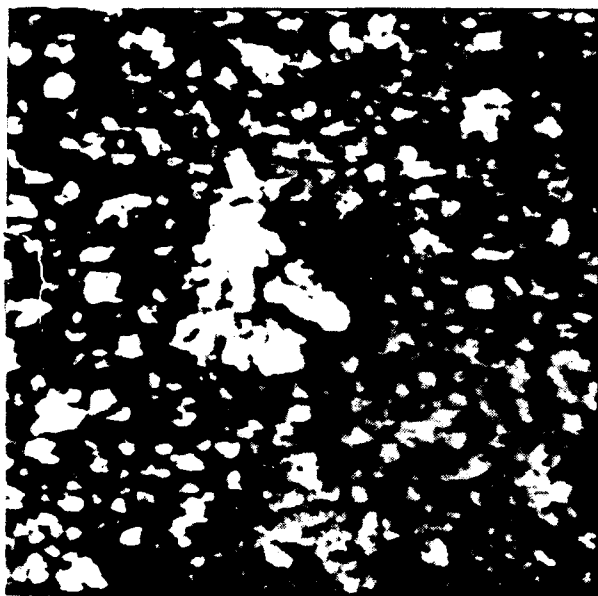
156 µM FULL SCALE   68 µM F.S.
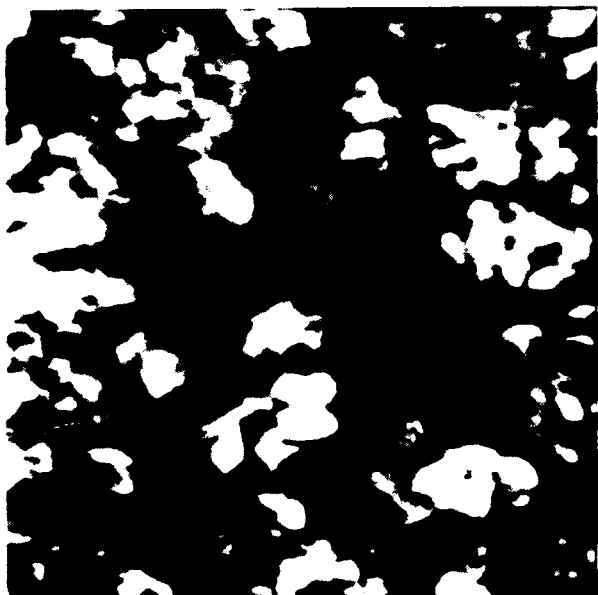
62 µM F.S.   34 µM F.S.

U.C., APRIL 1981 (LEFT) AND MAY 1981 (RIGHT)   FIG. A1-7

Ga$^+$ FOCUSED-ION-BEAM IMAGES
Ag-COATED FOSSIL RADIOLARIAN
UC-SIM. ANALOG DISPLAY. SLOW SCAN
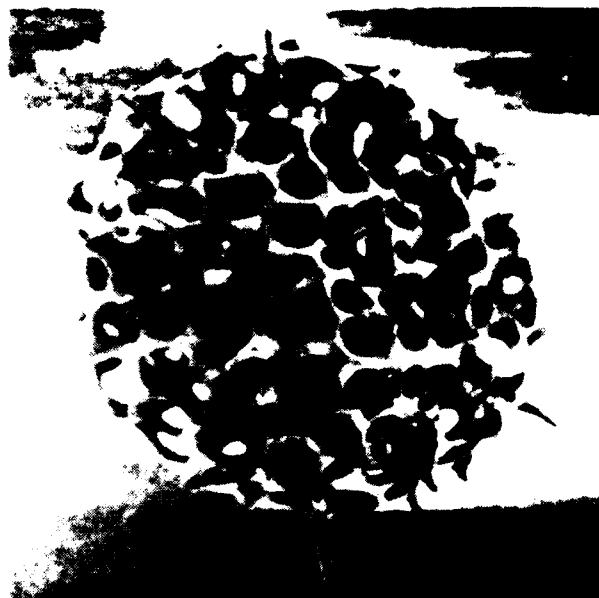
108 UM FULL SCALE

70 UM F.S.

35 UM F.S.

17.5 UM F.S.

U.C., MAY 1981   page 36   FIG. A1-8
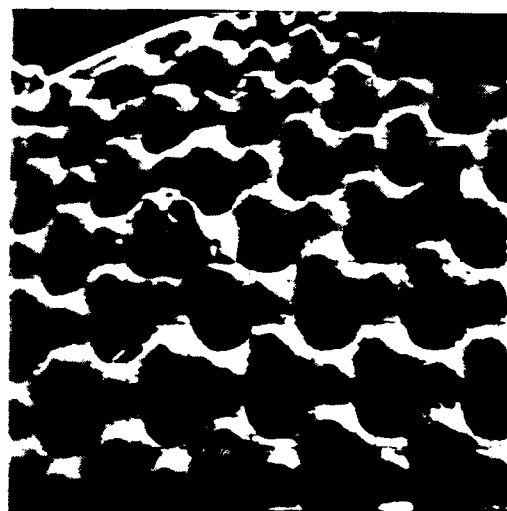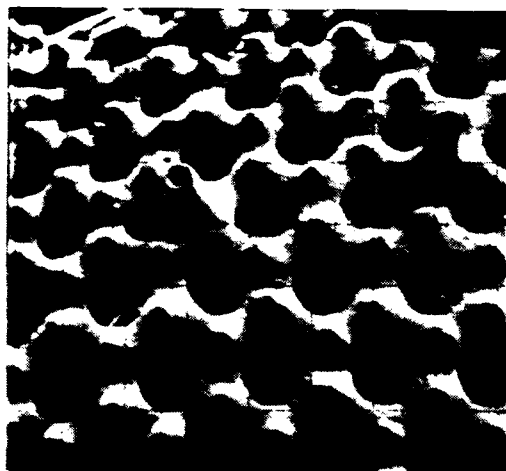
Fig. A1-9

Micrographs of a radiolarians
obtained with secondary electrons
from an 85 keV silicon ion beam
in the HRL-SIM.
Ion source: Au-Si eutectic, oper-
ated at 400° C.
Source current: 8 μA.
Probe current: ≃10^{-10} A.
Display: Analog mode, 1000 lines,
32 sec/frame.
Object material: Ag-coated SiO_2.

Note logo HRL imprinted on object
with ion beam, visible in the two
upper right micrographs.

APPENDIX 2

STUDIES OF SECONDARY ELECTRON AND ION IMAGING

WITH THE UNIVERSITY OF CHICAGO

60 keV Ga+ PROTOTYPE SCANNING ION MICROSCOPE

IMAGING OF SURFACE TOPOGRAPHY

SECONDARY ELECTRON vs

SECONDARY ION IMAGES IN SIM

Ga^+ FOCUSED-ION-BEAM IMAGES
RECRYSTALLIZED, POLISHED, HNO_3-ETCHED COPPER
HIGH DEFINITION IMAGING OF SURFACE TOPOGRAPHY
IMPROVED RESOLUTION 60 keV UC-SIM

SE

76 µM FULL SCALE

38 µM F.S.

SI
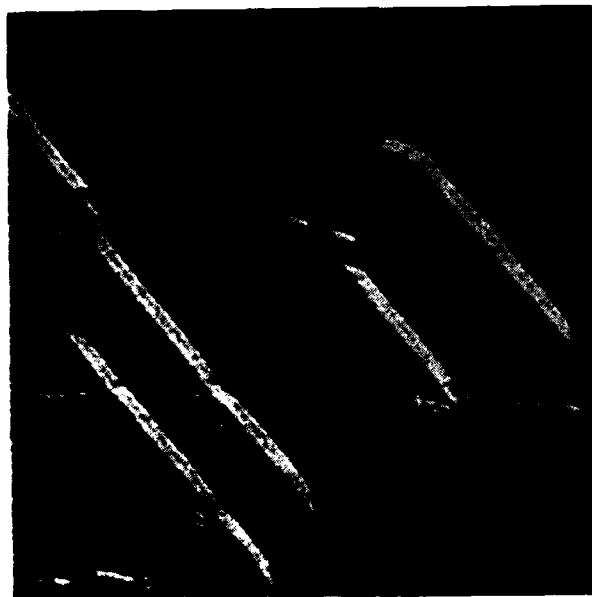
190 µM F.S.

76 µM F.S.

Ga^+ FOCUSED-ION-BEAM IMAGES
UNCOATED EPROM CHIP (INTEL D 2758)
SECONDARY ELECTRON (ANALOG) VS
SECONDARY ION (PULSE MODE, 1.8×10^7 COUNTS) IMAGES
60 KEV UC-SIM

SECONDARY ELECTRON SIGNAL

SECONDARY ION SIGNAL

180 μM FULL SCALE

204 μM F.S.

72 μM F.S.
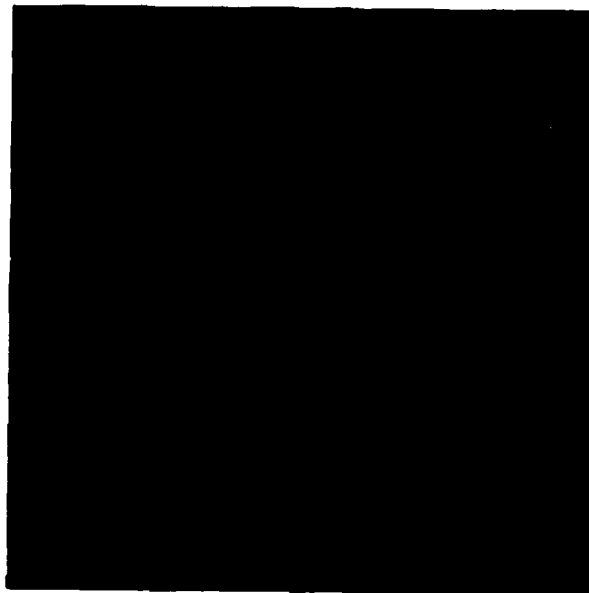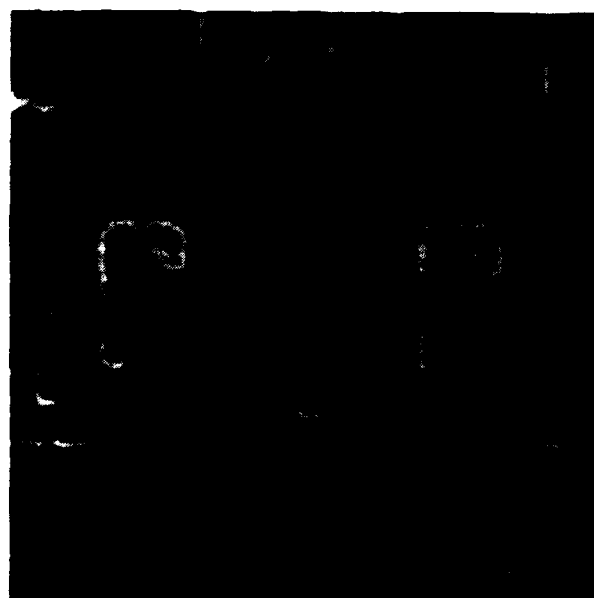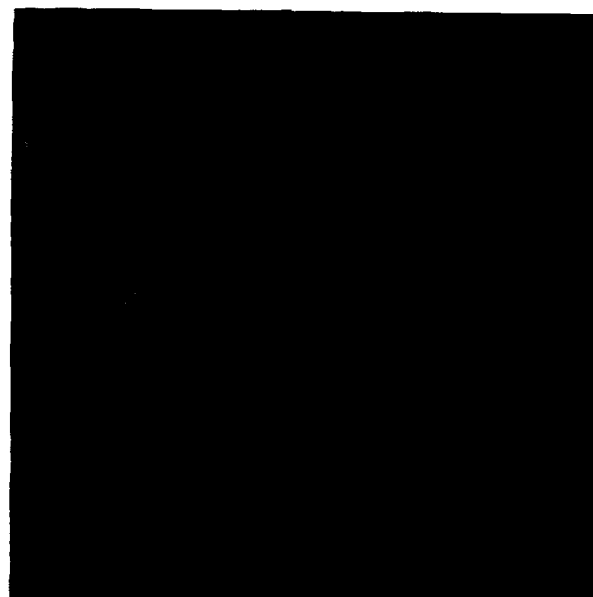
82 μM F.S.

U.C., MARCH 1983 (LEFT) AND APRIL 1983 (RIGHT)

FIG. A2-2

IMAGING OF THREE DIMENSIONAL OBJECTS

SECONDARY ELECTRON vs SECONDARY ION

IMAGES IN SIM

GA$^+$ FOCUSED-ION-BEAM IMAGES
DROSOPHILA MELANOGASTER, UNCOATED
COMPARISON OF SECONDARY ELECTRON VS SECONDARY ION IMAGES
PULSE-MODE, 6×10^6 COUNTS DISPLAYED
60 KEV UC-SIM
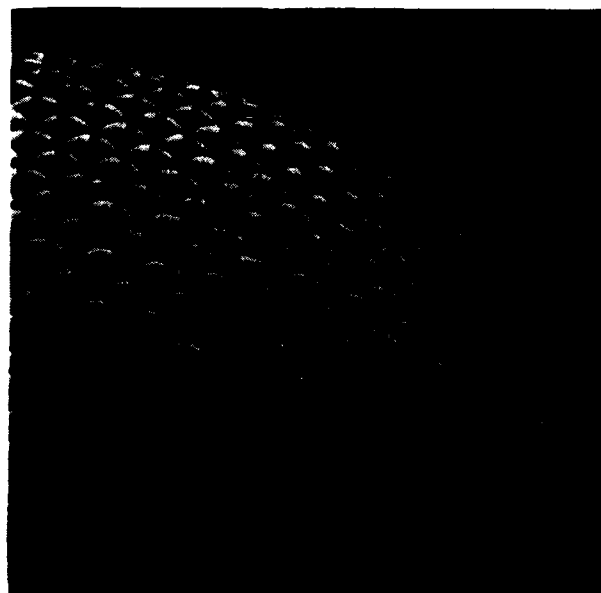
SECONDARY ELECTRON SIGNAL   SECONDARY ION SIGNAL

187 μM FULL SCALE   187 μM F.S.

75 μM F.S.   75 μM F.S.
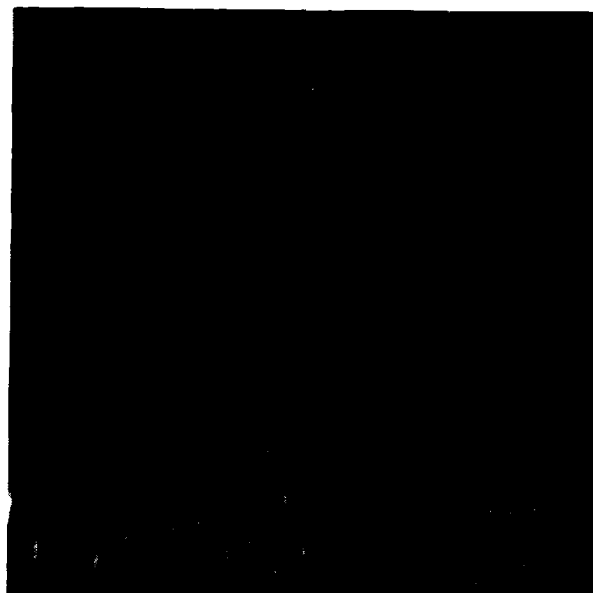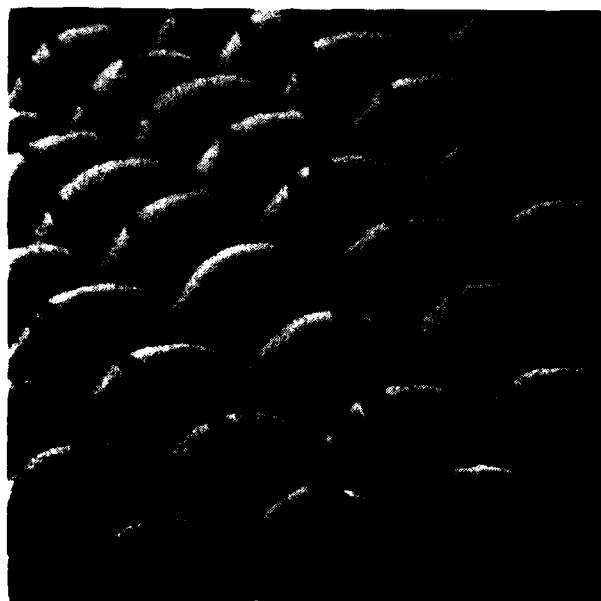
GA$^+$ FOCUSED-ION-BEAM IMAGES
CACOXENITE (IRON PHOSPHATE, HYDRATED)
COMPARISON OF SECONDARY ELECTRON VS SECONDARY ION IMAGES
PULSE MODE, 9×10^6 COUNTS DISPLAYED
60 KEV UC-SIM

SECONDARY ELECTRON SIGNAL

SECONDARY ION SIGNAL

440 µM FULL SCALE
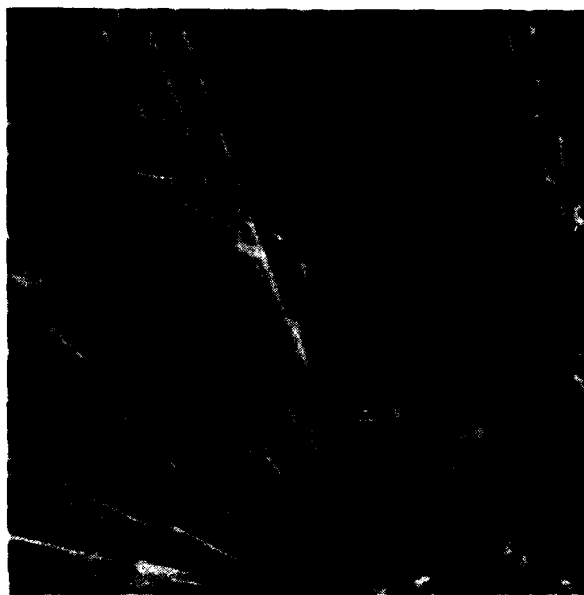
440 µM F.S.

88 µM F.S.

88 µM F.S.

SECONDARY ION IMAGING OF

INSULATORS IN SIM

Ga$^+$ FOCUSED-ION-BEAM IMAGES
FOSSIL DIATOMS (SiO_2)
IMAGING WITH POSITIVE SECONDARY IONS
IMPROVED RESOLUTION 60 keV UC-SIM
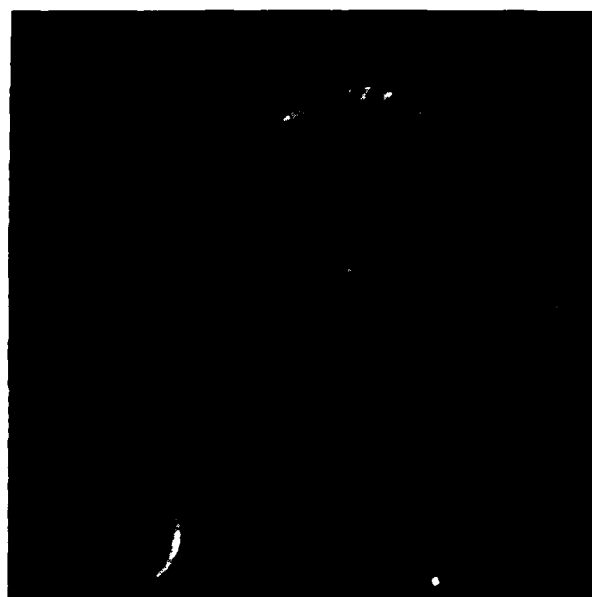
190 μM FULL SCALE   190 μM F.S.
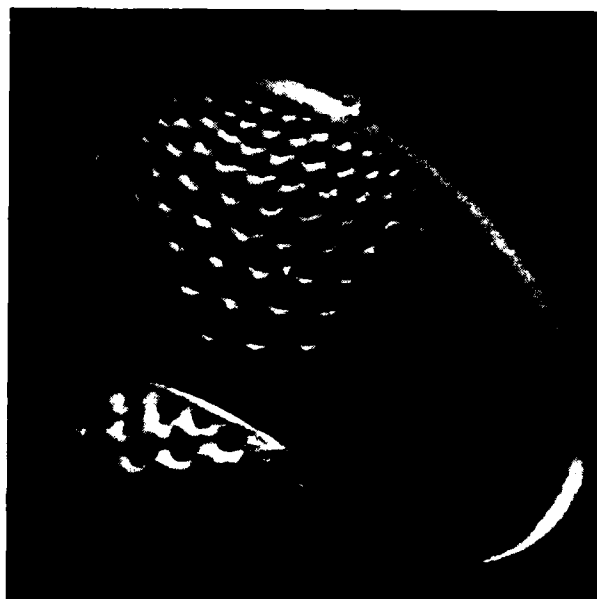
76 μM F.S.   76 μM F.S.
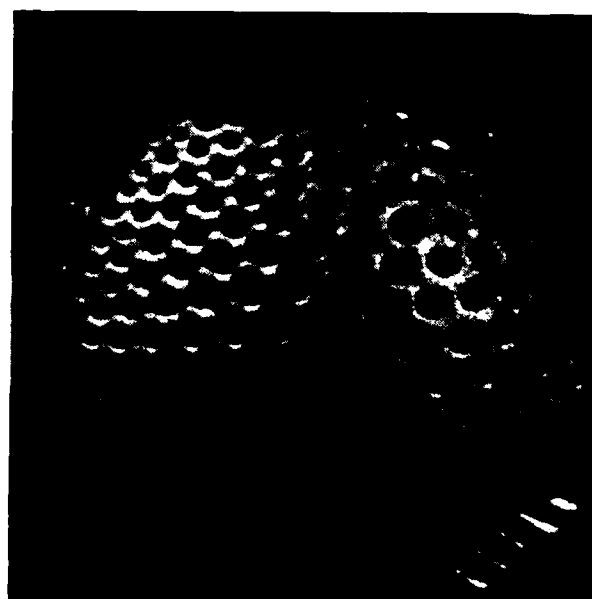
Ga$^+$ FOCUSED-ION-BEAM IMAGES
DROSOPHILA MELANOGASTER, UNCOATED
SECONDARY ION SIGNAL
IMPROVED RESOLUTION 60 keV UC-SIM
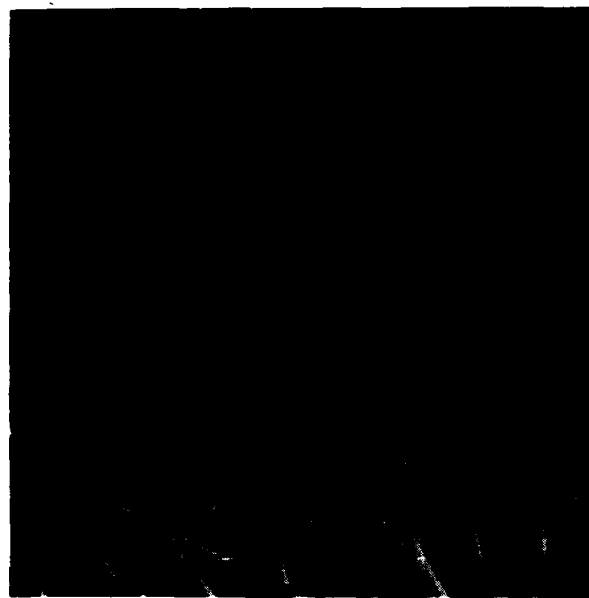
187 μM FULL SCALE
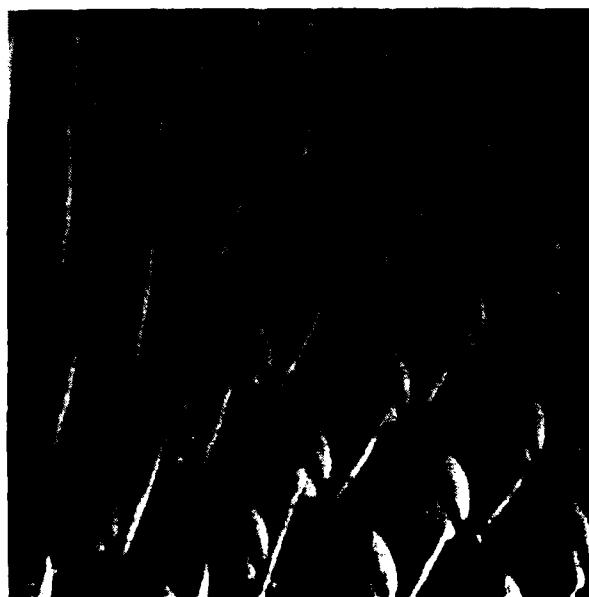
75 μM FULL SCALE

GA$^+$ FOCUSED-ION-BEAM IMAGES
CACOXENITE (IRON PHOSPHATE, HYDRATED)
SECONDARY ION SIGNAL
60 KEV UC-SIM

440 μM FULL SCALE
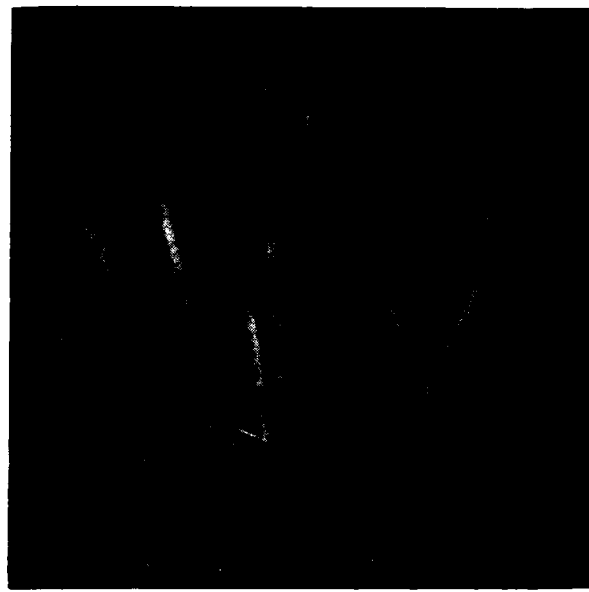
440 μM F.S.

220 μM F.S.
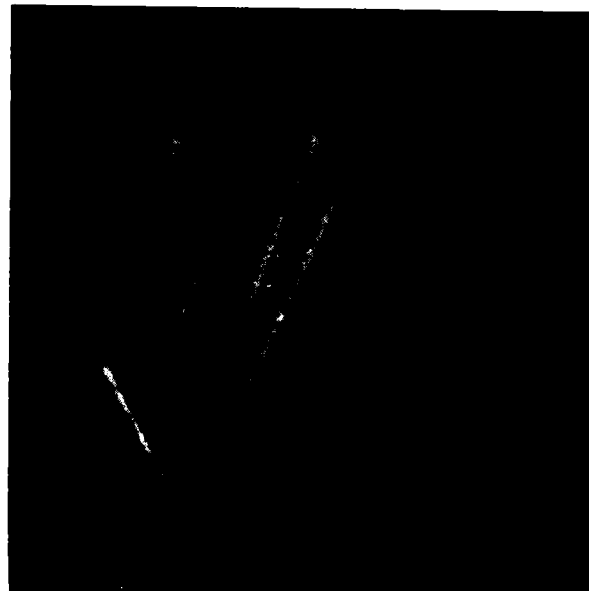
220 μM F.S.

GA$^+$ FOCUSED-ION-BEAM IMAGES
UNCOATED HUMAN ERYTHROCYTES, CRITICAL POINT DRIED
DISAPPEARANCE OF CHARGING EFFECTS UNDER GA$^+$ IMPLANT
55 KV UC-SIM

INITIAL IMAGE
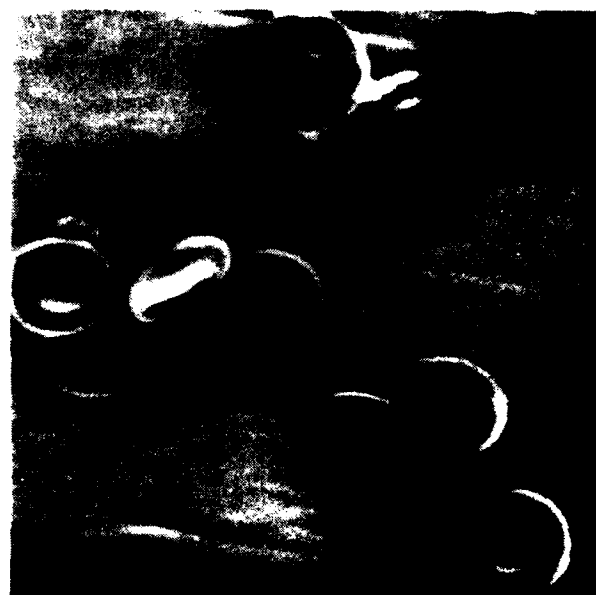
AFTER 7.3×10^{15} IONS/CM^2

36 μM FULL SCALE
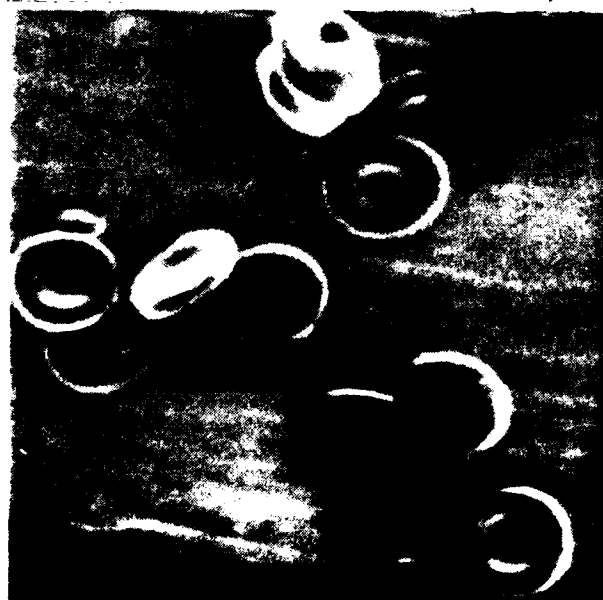
AFTER 1.7×10^{16} IONS/CM^2
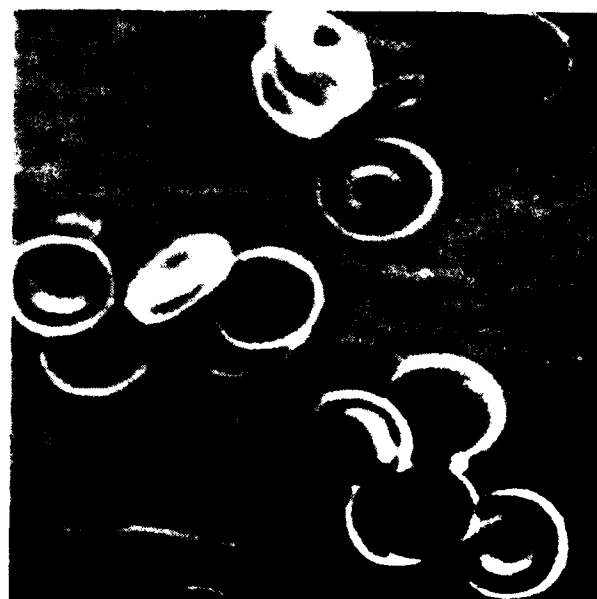
AFTER 2.9×10^{16} IONS/CM^2

Ga$^+$ FOCUSED-ION-BEAM IMAGES
UNCOATED HUMAN ERYTHROCYTES, CRITICAL POINT DRIED
SIM vs SEM IMAGING (AFTER Ga$^+$ IMPLANT)

55 kV UC-SIM
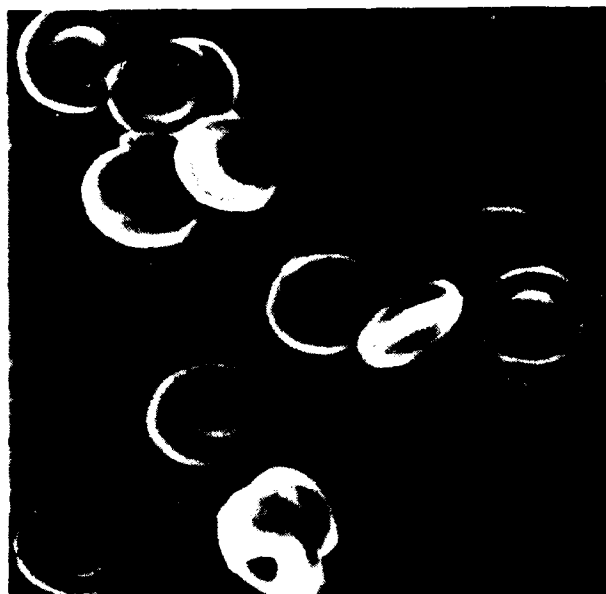
10 kV HITACHI HFS-2 SEM
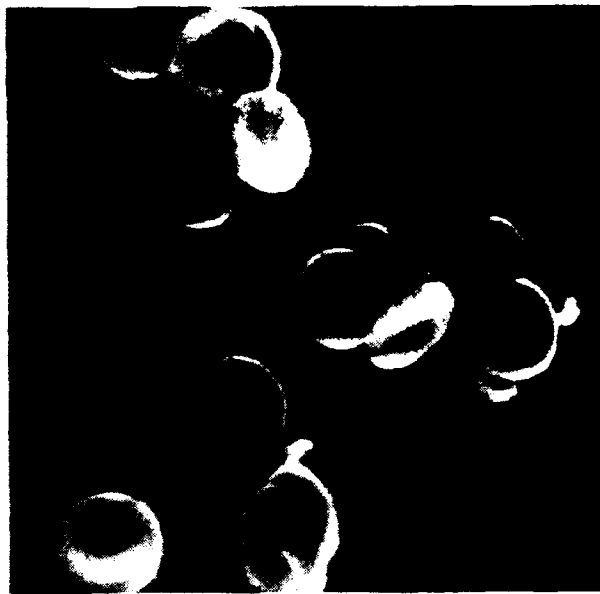
36 μM FULL SCALE

36 μM F.S.
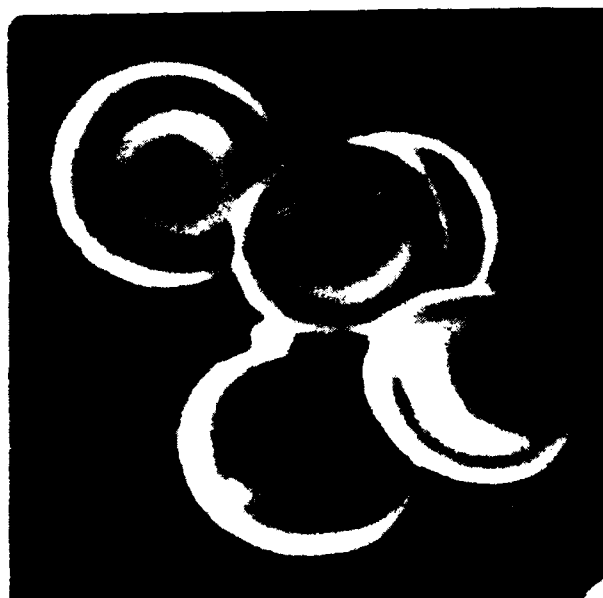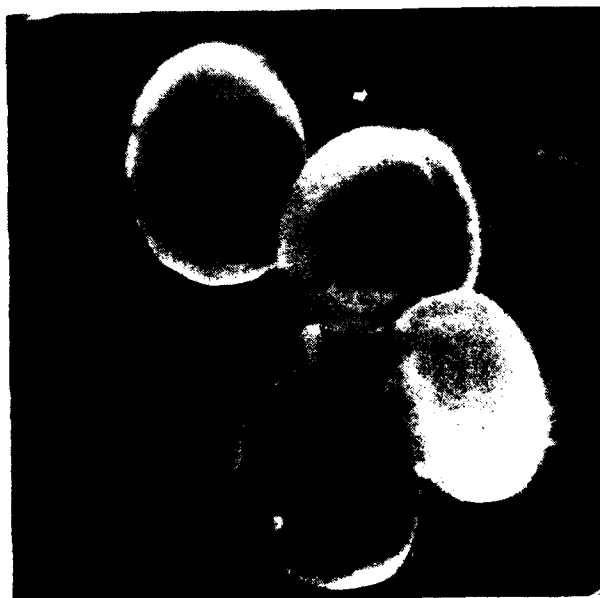
18 μM F.S.

18 μM F.S.

Ga$^+$ FOCUSED-ION-BEAM IMAGING
UNCOATED EPROM CHIP (INTEL D 2758)
SIM IMAGING (UNAFFECTED BY SURFACE CHARGING)
VS. SEM IMAGING

60 KV UC-SIM

25 KV HITACHI HFS-2 SEM

72 μM FULL SCALE

72 μM F.S.

36 μM F.S.

36 μM F.S.

U.C., MARCH 1982   page 51   FIG. A2-10
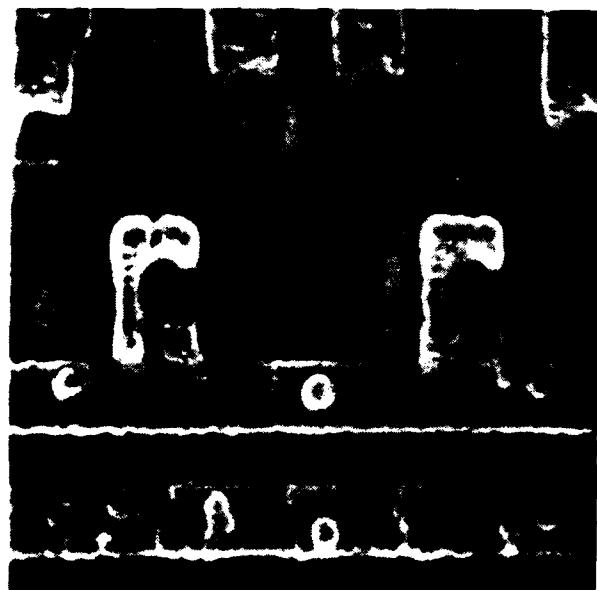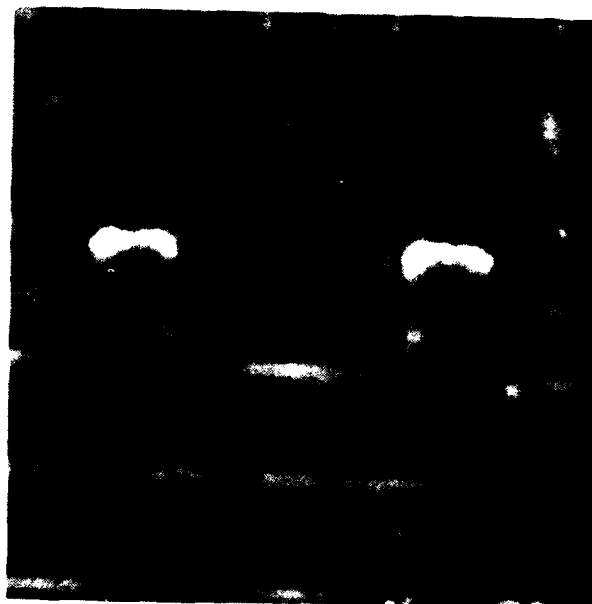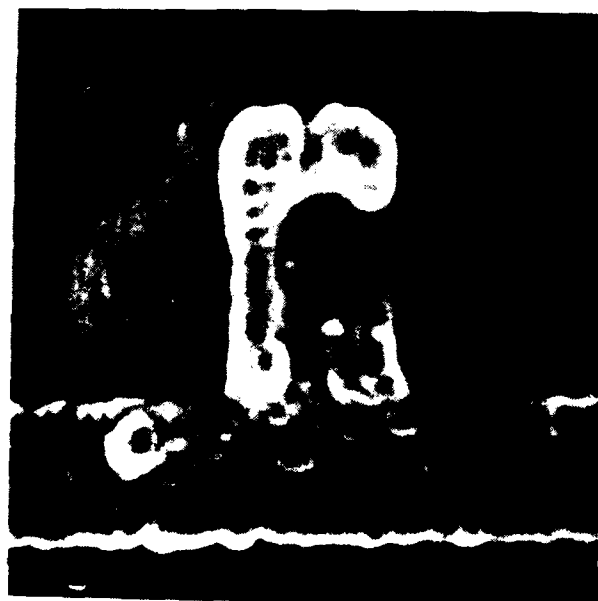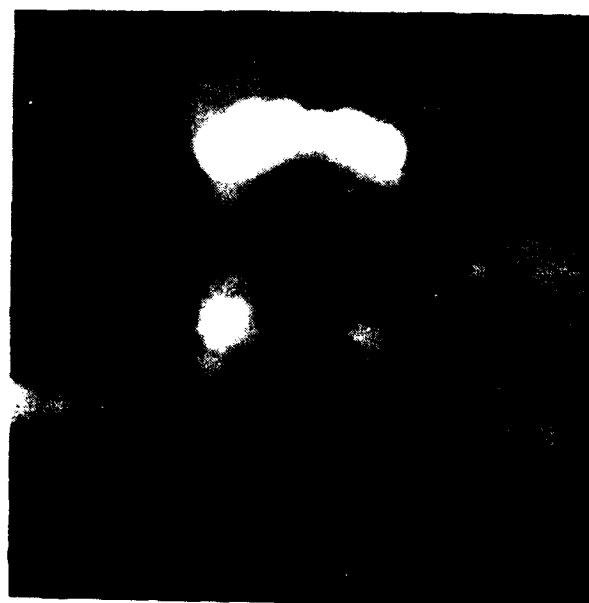
UNCOATED EPROM CHIP (INTEL D 2758)
SEM IMAGING (AFFECTED BY SURFACE CHARGING OF PASSIVATION LAYER)
VS. SEM IMAGING OF AREAS Ga^+-IMPLANTED DURING SIM IMAGING
25 KV HITACHI HFS-2 SEM

No Ga^+ IMPLANT

AFTER SIM SCAN

72 μM FULL SCALE

72 μM F.S.

36 μM F.S.
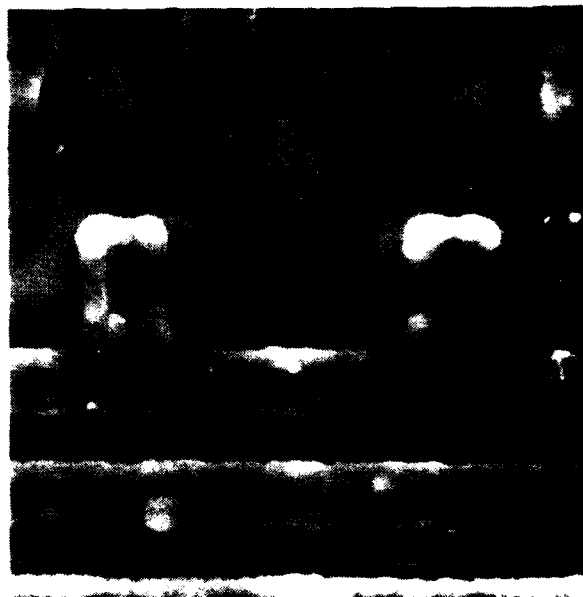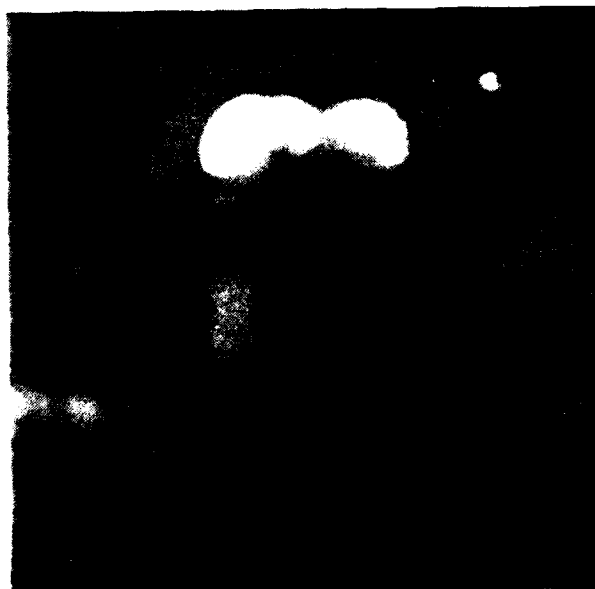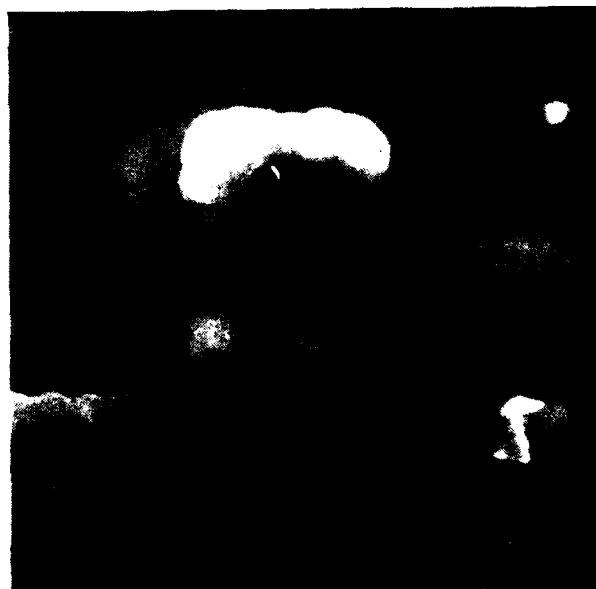
36 μM F.S.

Z-CONTRAST IN

SIM ISE IMAGES

vs. SEM IMAGES

Ga^+ FOCUSED-ION-BEAM IMAGES
PASSIVATED INTEGRATED CIRCUITS
ALUMINUM METALLIZATION ON SiO_2

60 keV UC-SIM
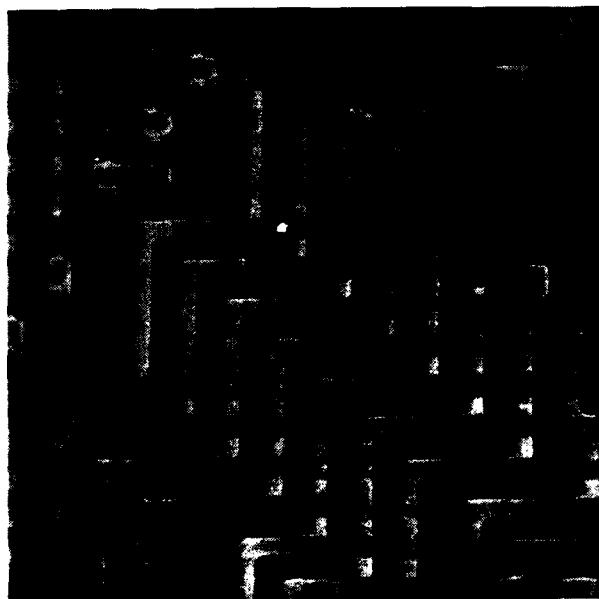
25 keV HITACHI HFS-2 SEM
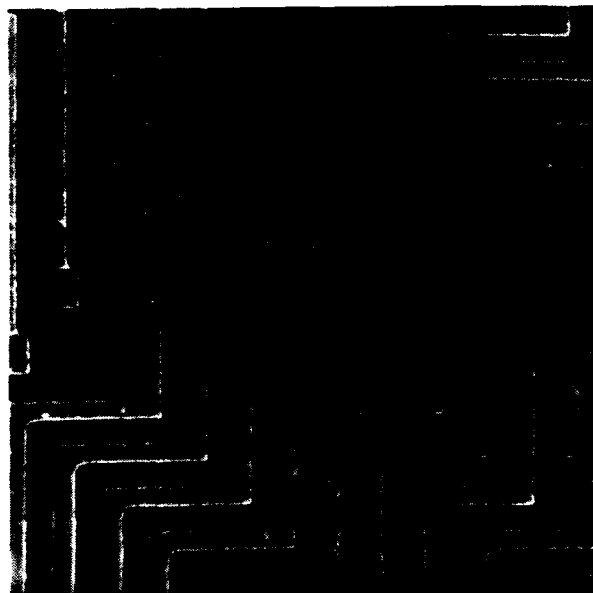
180 μM FULL SCALE
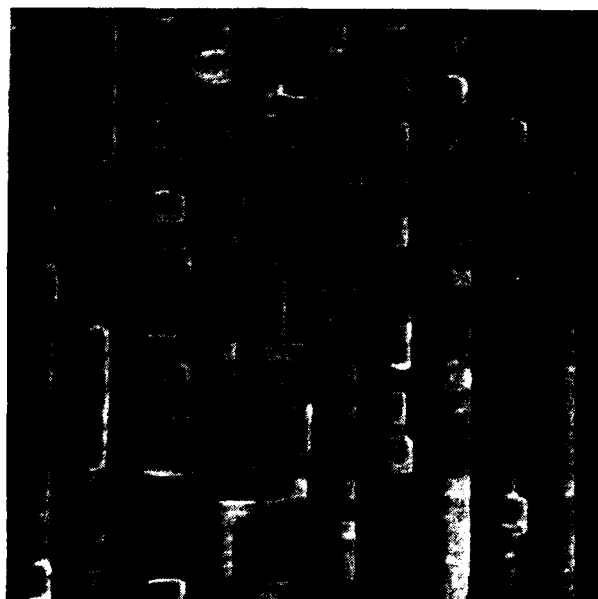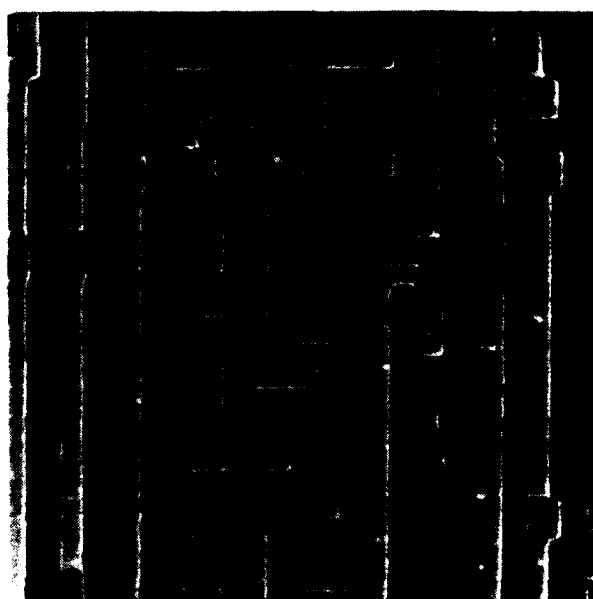
180 μM F.S.

180 μM F.S.

180 μM F.S.

Ga$^+$ FOCUSED-ION-BEAM IMAGES
ELEMENTAL CONTRAST IN SECONDARY ELECTRON
IMAGES FROM ION VS. ELECTRON BEAM SCANS

320 µM FULL SCALE   Au on Fe   320 µM F.S.
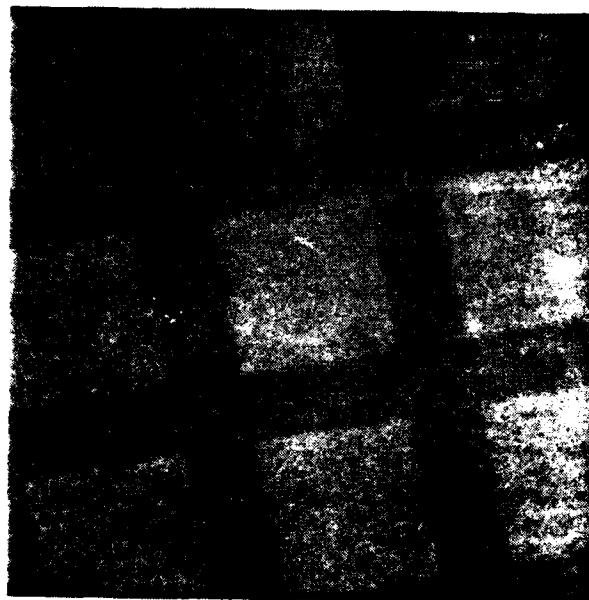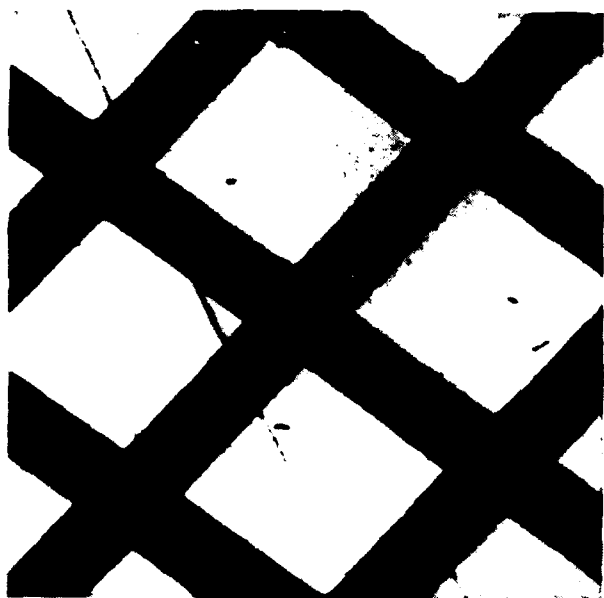
320 µM F.S.   Ag on Fe   320 µM F.S.
60 keV UC -SIM   10 keV COATES & WELTER SEM
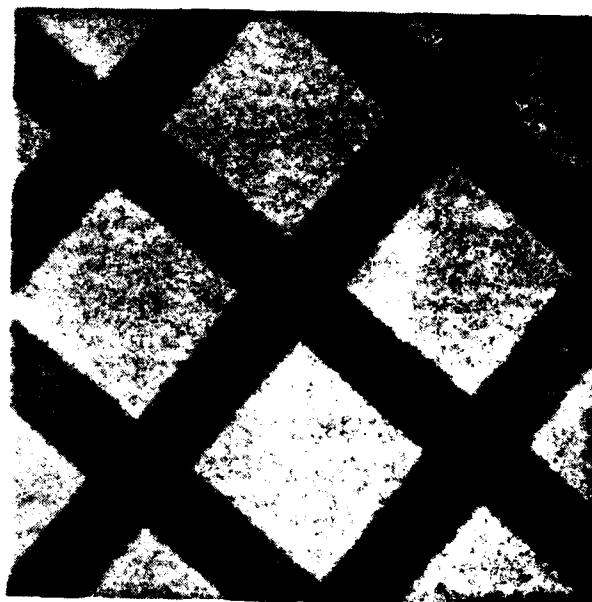
CRYSTALLOGRAPHIC CONTRAST

DUE TO PRIMARY ION CHANNELLING IN METALS

CORRELATION OF SECONDARY ELECTRON

AND ION EMISSION

Ga$^+$ FOCUSED-ION-BEAM IMAGES
RECRYSTALLIZED, POLISHED, HNO$_3$-ETCHED BRASS
EVOLUTION OF SECONDARY ELECTRON IMAGE
UNDER CONTINUOUS RASTER ION BOMBARDMENT
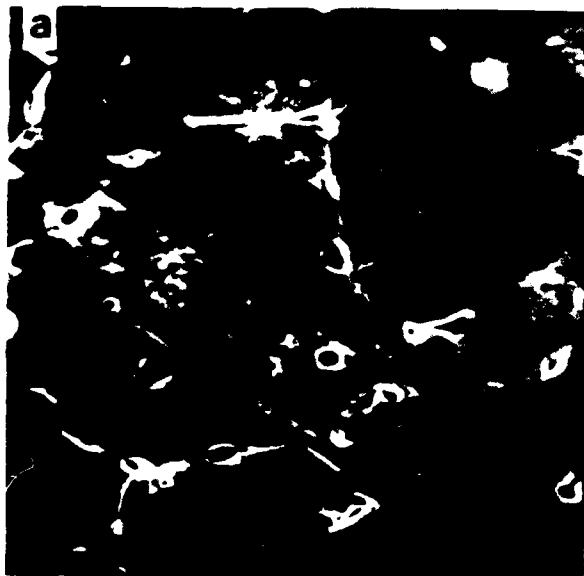
160 μM FULL SCALE
ELAPSED TIME: 0
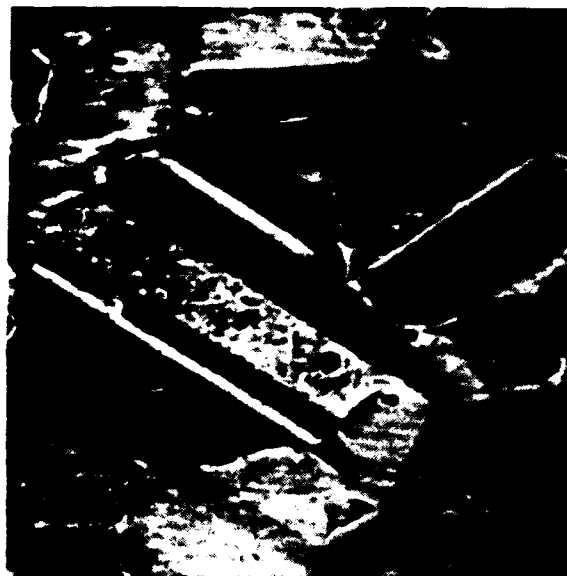
160 μM F.S.
ELAPSED TIME: 10 MIN.
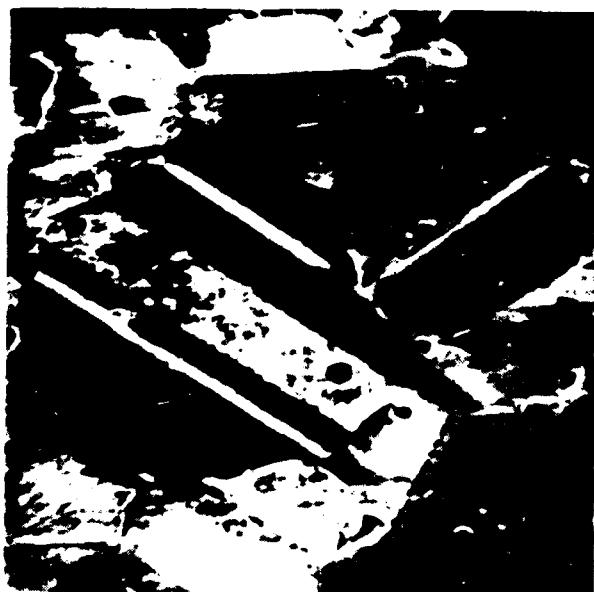
160 μM FULL SCALE
ELAPSED TIME: 15 MIN.

64 μM F.S.
AFTER 200 MIN. AT 160 UM F.S.

GA$^+$ FOCUSED-ION-BEAM IMAGES
RECRYSTALLIZED, POLISHED, HNO$_3$-ETCHED BRASS
CRYSTALLOGRAPHIC CONTRAST IN SECONDARY ELECTRON
SIM IMAGES VS. SURFACE TOPOGRAPHY IN SEM IMAGES

64 µM FULL SCALE
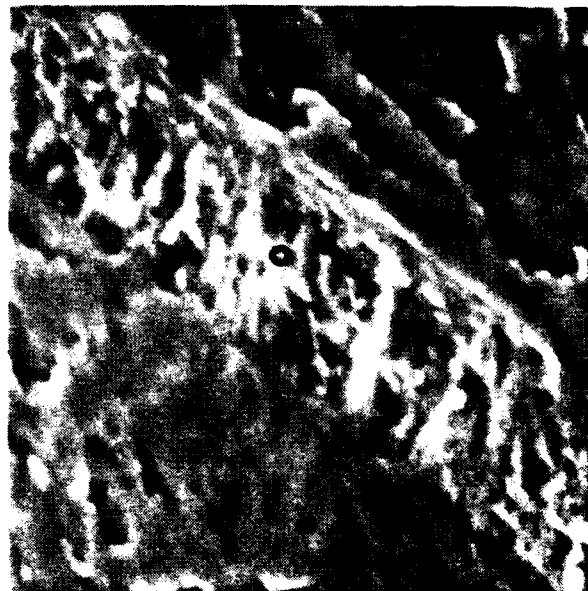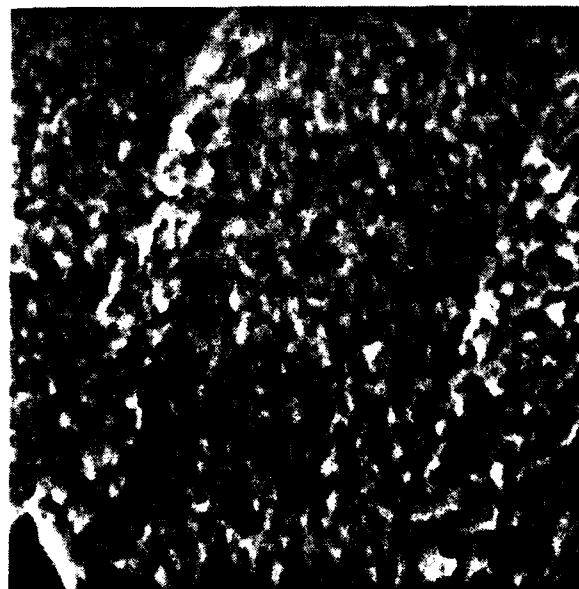
13 µM F.S.

64 µM F.S.
60 KEV UC-SIM

15 µM F.S.
10 KEV COATES & WELTER SEM

U.C. AUGUST 1981   page 58   FIG. A2-15

Ga$^+$ FOCUSED-ION-BEAM IMAGES
RECRYSTALLIZED, POLISHED, HNO$_3$-ETCHED COPPER
SECONDARY ELECTRON IMAGES FROM ION VS. ELECTRON BEAM SCANS

180 μM FULL SCALE
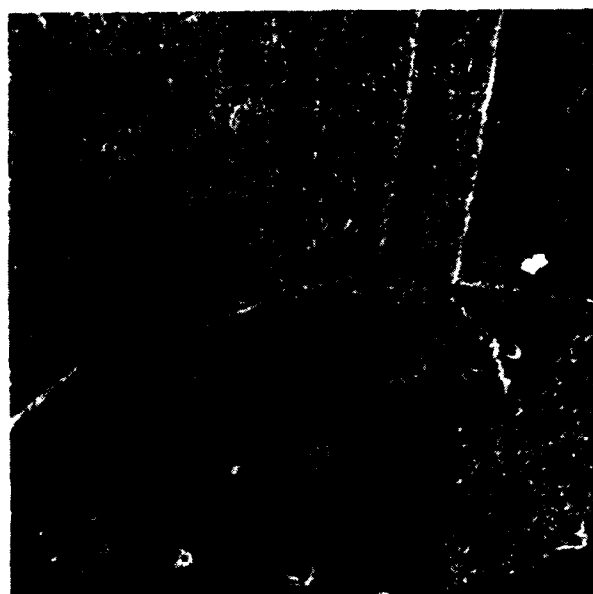
180 μM F.S.

180 μM F.S.

60 KEV UC-SIM

180 μM F.S.

25 KEV HITACHI HFS-2 SEM

Ga$^+$ FOCUSED-ION-BEAM IMAGES
RECRYSTALLIZED, POLISHED, HNO$_3$-ETCHED COPPER
CONTRAST REVERSALS DUE TO PRIMARY ION-CHANNELLING
SECONDARY ELECTRON IMAGES, 60 keV UC-SIM

NORMAL INCIDENCE   10^0 NORTH-SOUTH TILT

180 µM FULL SCALE   180 µM F.S.

180 µM F.S.   180 µM F.S.

Ga$^+$ FOCUSED-ION-BEAM IMAGES
RECRYSTALLIZED, POLISHED, HNO$_3$-ETCHED COPPER
CONTRAST REVERSALS DUE TO PRIMARY ION-CHANNELLING
COMPARISON OF SE vs SI IMAGES, 60 kV UC-SIM

NORMAL INCIDENCE   10° NORTH-SOUTH TILT

SE

360 μM FULL SCALE   360 μM F.S.

SI

360 μM F.S.   360 μM F.S.

U.C, JUNE 1982   page 61   FIG. A2-18

Ga$^+$ FOCUSED-ION-BEAM IMAGES
RECRYSTALLIZED, POLISHED, HNO$_3$-ETCHED COPPER
CONTRAST REVERSALS DUE TO PRIMARY ION-CHANNELLING
COMPARISON OF SE vs SI IMAGES, 60 kV UC-SIM

NORMAL INCIDENCE   10^0 NORTH-SOUTH TILT

SE

360 µM FULL SCALE   360 µM F.S.

SI
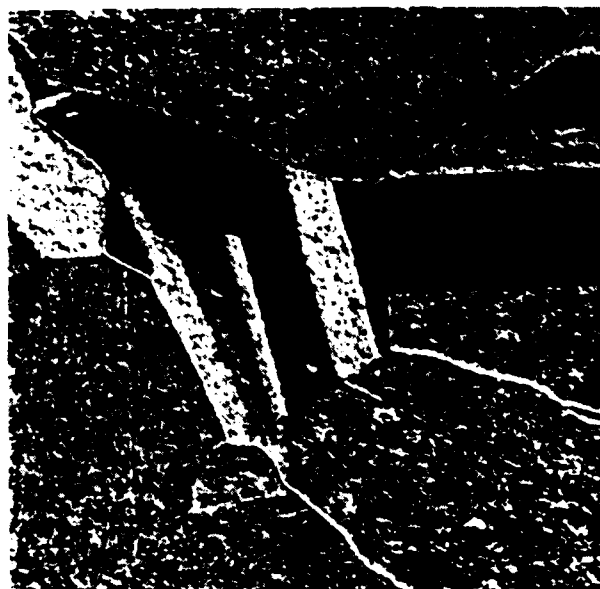
360 µM F.S.   360 µM F.S.

Ga$^+$ FOCUSED-ION-BEAM IMAGES
RECRYSTALLIZED, POLISHED, HNO$_3$-ETCHED COPPER
CONTRAST REVERSALS DUE TO PRIMARY ION CHANNELLING
CORRELATION OF SE vs SI EMISSION
IMPROVED RESOLUTION 60 keV UC-SIM

NORMAL INCIDENCE   10° NORTH-SOUTH TILT

SE

75 µM FULL SCALE

SI
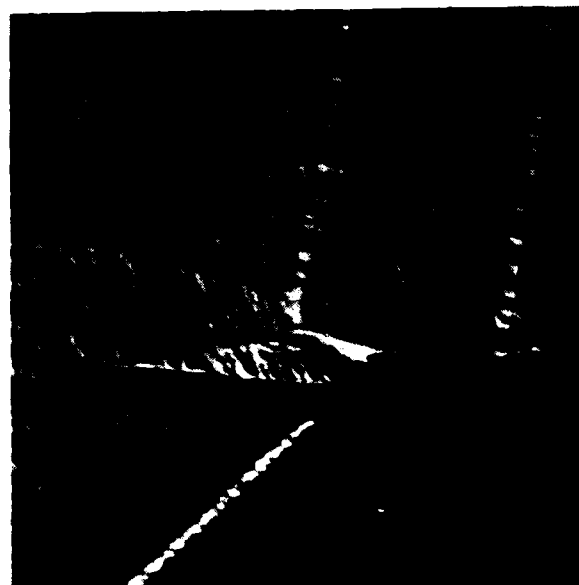
Ga^+ FOCUSED-ION-BEAM IMAGES
RECRYSTALLIZED, POLISHED, HNO_3-ETCHED COPPER
CONTRAST REVERSALS DUE TO PRIMARY ION CHANNELLING
CORRELATION OF SE vs SI EMISSION
IMPROVED RESOLUTION 60 keV UC-SIM

NORMAL INCIDENCE 10^0 NORTH-SOUTH TILT

SE
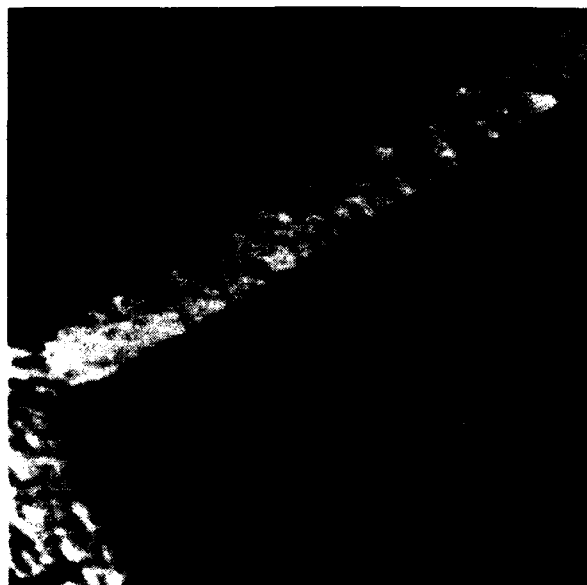
37 µM FULL SCALE

SI
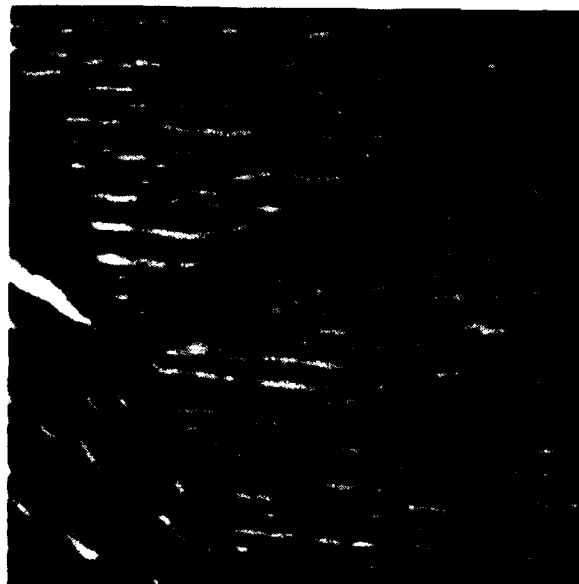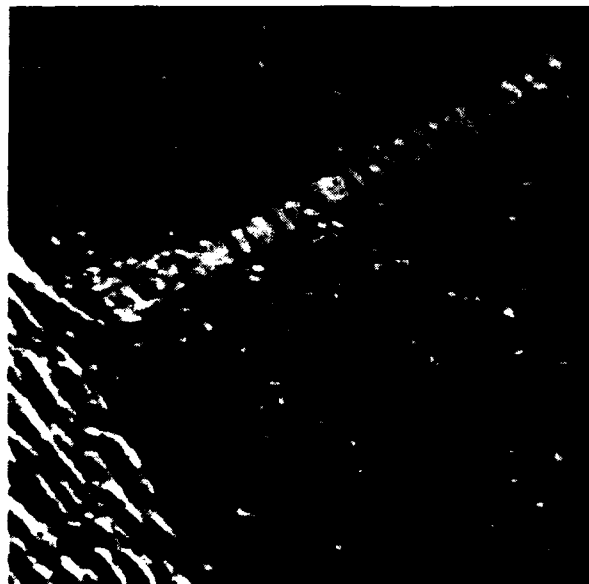
CRYSTALLOGRAPHIC CONTRAST

IN CRYSTALLINE SILICON

Ga$^+$ FOCUSED-ION-BEAM IMAGES
RECRYSTALLIZED, POLISHED, NaOH-ETCHED SILICON
ORIENTATION DEPENDENCE OF CRYSTALLOGRAPHIC CONTRAST,
DUE TO PRIMARY ION-CHANNELLING, IN SE, SIM IMAGES

NORMAL INCIDENCE   10^0 NORTH-SOUTH TILT

340 μM FULL SCALE   340 μM F.S.

340 μM F.S.   340 μM F.S.

Ga$^+$ FUCUSED-ION-BEAM IMAGES
RECRYSTALLIZED, POLISHED, NaOH-ETCHED SILICON
EFFECT OF DIFFERENTIAL AMORPHISATION ON ION-CHANNELLING CONTRAST
OBSERVED AT NORMAL INCIDENCE IN SE, SIM IMAGES

170 µM FULL SCALE
DOSE: 2.5 x 10^{13} IONS/CM^2

170 µM F.S.
AFTER 1.5 x 10^{14} IONS/CM^2

340 µM F.S.
DOSE: 6 x 10^{12} IONS/CM^2

340 µM F.S.
AFTER 7.5 x 10^{14} IONS/CM^2

GA$^+$ FOCUSED-ION-BEAM IMAGES
RECRYSTALLIZED, POLISHED, NaOH-ETCHED SILICON
ORIENTATION-INDEPENDENT CONTRAST DUE TO PREFERENTIAL
OXIDATION OF (III) SURFACES IN SE, SIM IMAGES

NORMAL INCIDENCE
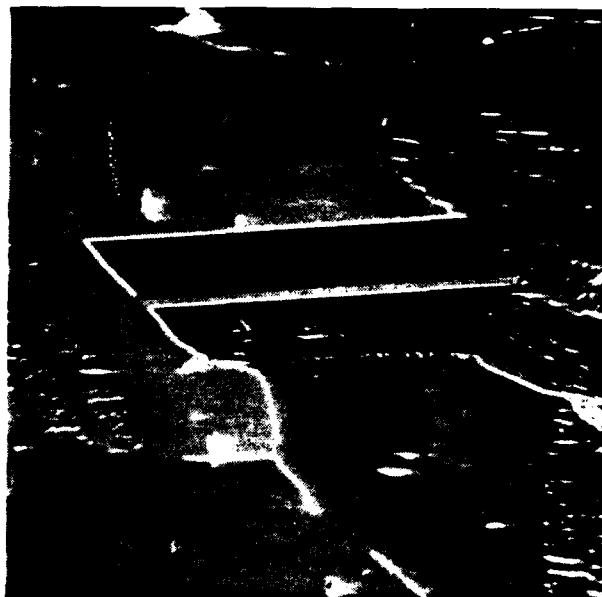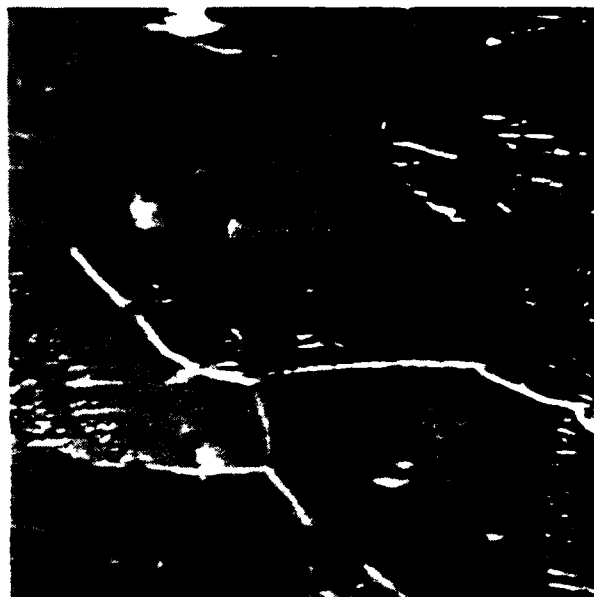
10° NORTH-SOUTH TILT

180 µM FULL SCALE

180 µM F.S.

180 µM F.S.

180 µM F.S.

Ga[+] FOCUSED-ION-BEAM IMAGES
RECRYSTALLIZED, POLISHED, NaOH-ETCHED SILICON
CRYSTALLOGRAPHIC CONTRAST IN SE, SIM IMAGES,
VS. SURFACE TOPOGRAPHY IN SEM

180 μM FULL SCALE
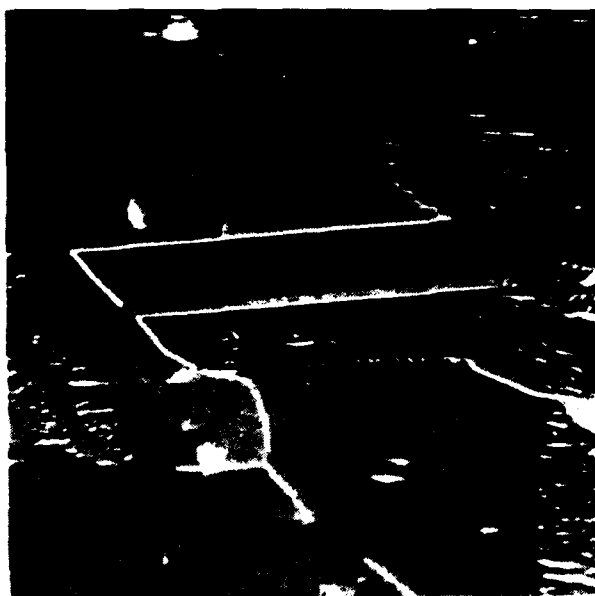
180 μM F.S.

180 μM F.S.
60 KEV UC-SIM
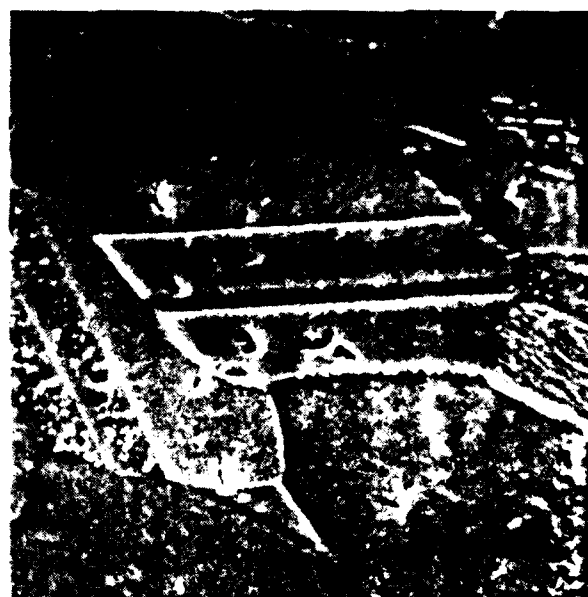
180 μM F.S.
25 KEV HITACHI HFS-2 SEM

GA+ FOCUSED-ION-BEAM IMAGING AND ETCHING
RECRYSTALLIZED, POLISHED, HNO₃-ETCHED COPPER
CORRELATION OF ION-CHANNELING EFFECTS
IN SE, SI EMISSION AND SPUTTERING

GA+
SIM
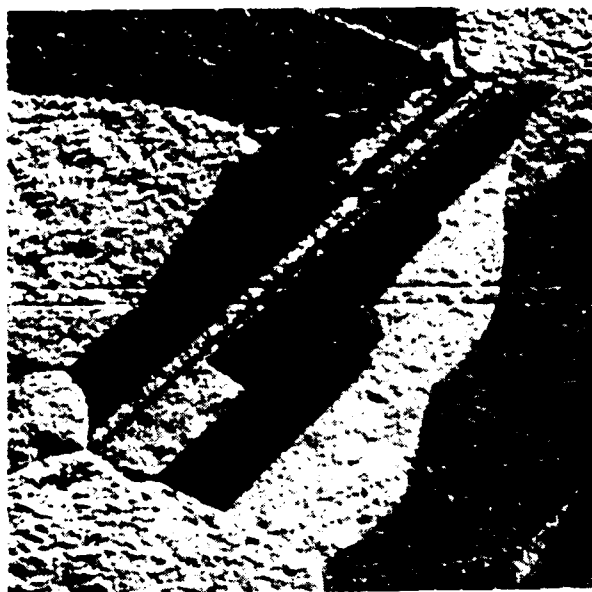
180 µM FULL SCALE,
SI IMAGE
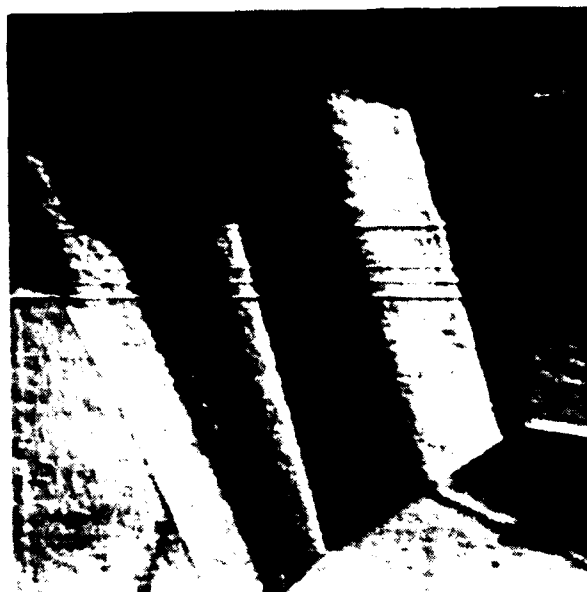
180 µM FULL SCALE,
SE IMAGE

SEM
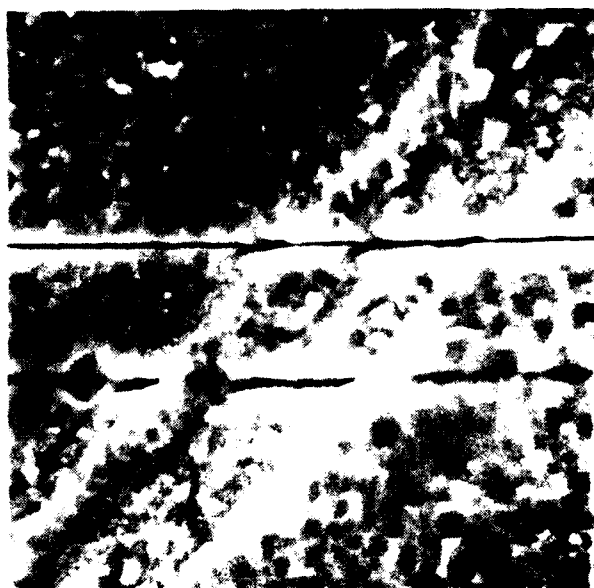
17 µM F.S.

17 µM F.S.

TOTAL ION-BEAM WRITING DOSE OF
2.9×10^{18} IONS/CM^2, IN:
TOP LINE: SINGLE SCAN
BOTTOM LINE: 100 SCANS

ION-BEAM WRITING DOSES ARE:
LINE 1: 3.1×10^{17} IONS/CM^2
LINE 2: 7.8×10^{17} IONS/CM^2
LINE 3: 1.2×10^{18} IONS/CM^2
LINE 4: 3.1×10^{18} IONS/CM^2

ION-CHANNELLING EFFECTS

ON THE SPUTTERING RATES

OF CRYSTALLINE MATERIALS

Ga$^+$ FOCUSED-ION-BEAM IMAGING AND ETCHING
NaOH-etched EFG silicon
SPUTTERING EXPERIMENTS BY DIRECT ION-BEAM-WRITING

60 keV UC-SIM | 25 keV HITACHI HFS-2 SEM

SE

72 μM FULL SCALE

72 μM F.S., UNCOATED

SI

72 μM F.S.
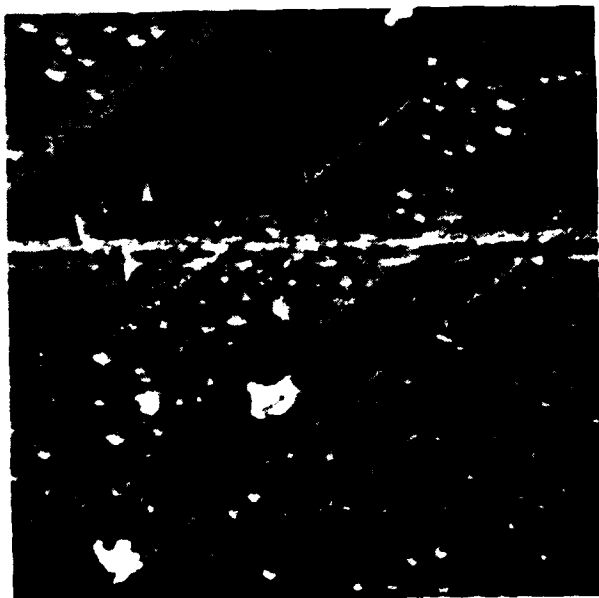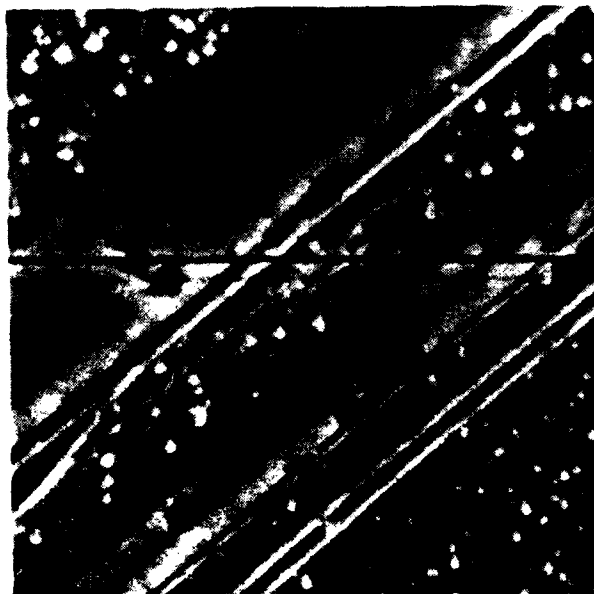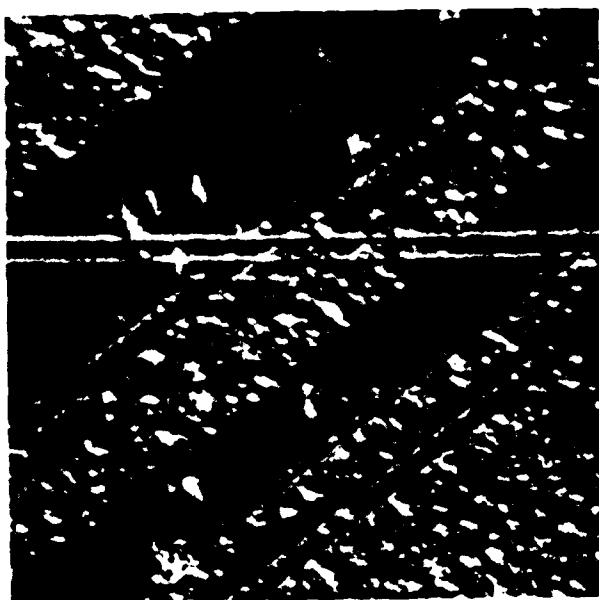
17 μM F.S., Pt-COATED

ION BEAM WRITING DOSES ARE:
LINE 1: 6.8×10^{18} IONS/CM^2
2: 2.0×10^{18} IONS/CM^2
3: 8.5×10^{17} IONS/CM^2
4: 4.2×10^{17} IONS/CM^2

APPENDIX 3

UC-HRL SIM/SIMS

MICROPROBE DESIGN AND REALIZATION
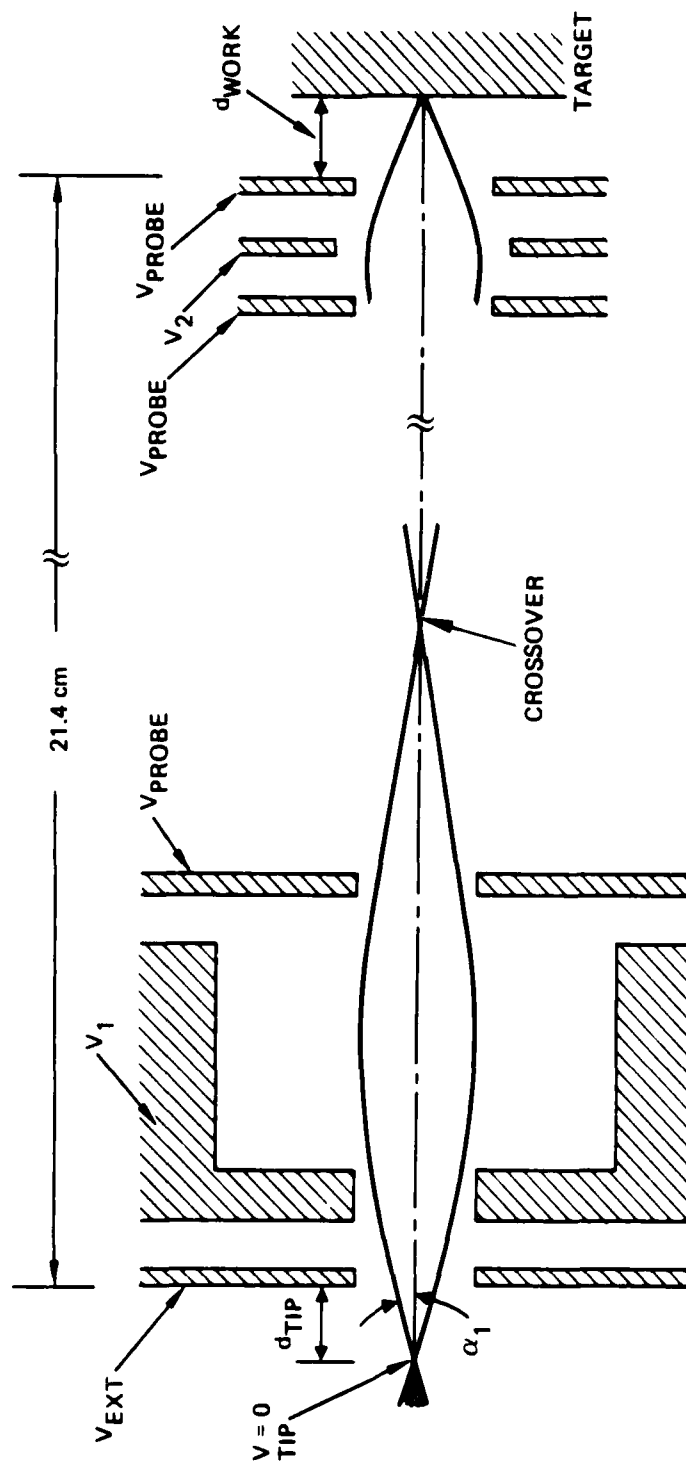
10674—3

Fig. A3-1   Schematic Drawing of High Resolution Focusing Column

10674−2

GFI SOURCE (H_2^+)

$V_{PROBE} = 60$ kV

$\Delta V = 2V$

$d_{WORK} = 5.6$ cm

$= 2.7$ cm

$= 1.2$ cm

$V_{EXT} = 5$ kV

$= 30$ kV

d_{SPOT}, Å

α_1, rad
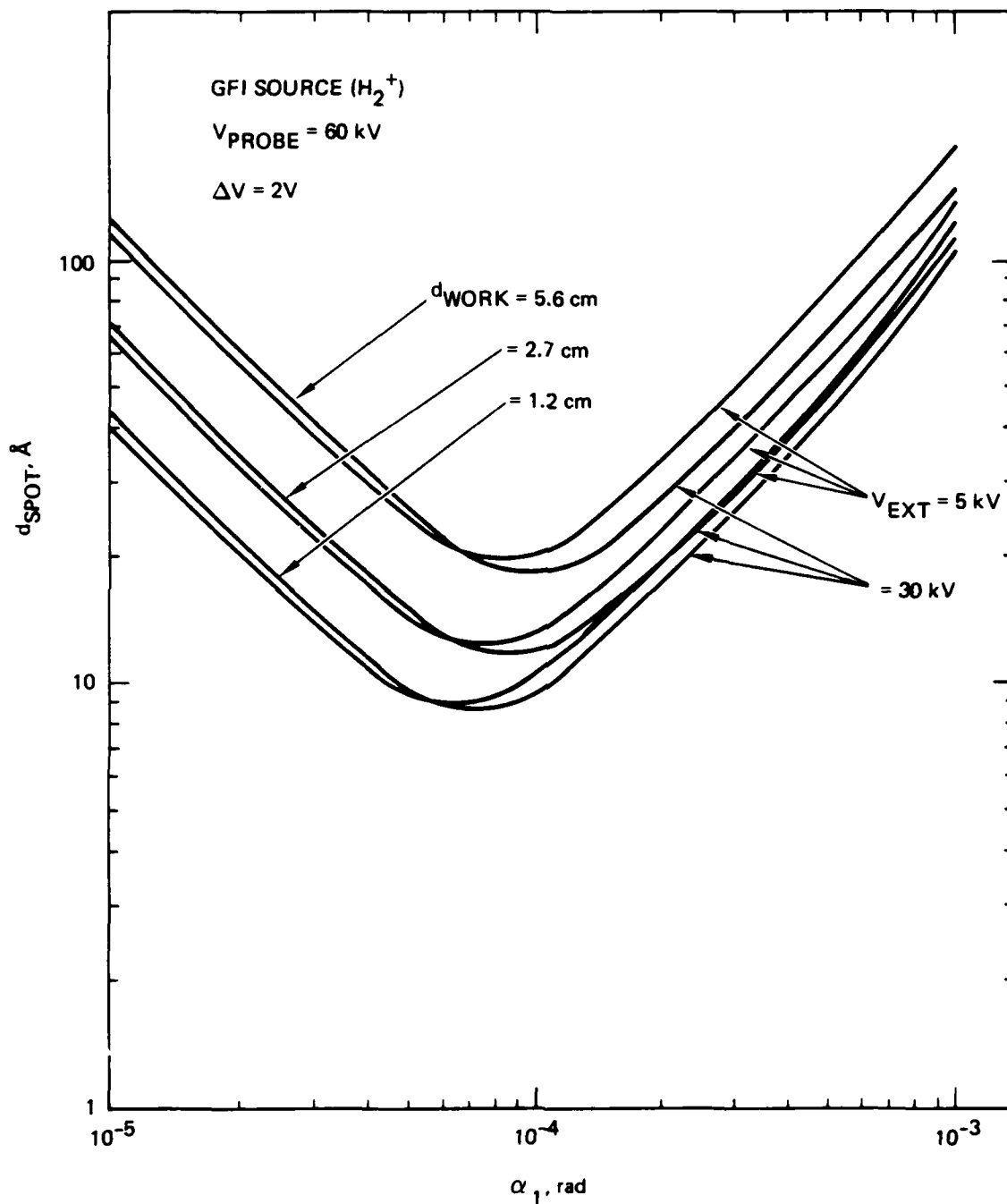
Fig. A3-2   Spot size as a function of aperture half-angle for GFI source
omitting effect of virtual source size. At $V_{EXT} = 5$ kV, the
overall magnification of the system ranges between ~0.1 and ~0.4,
increasing with d_{WORK}. At $V_{EXT} = 30$ kV, such range becomes
~0.3 - 0.7.

10674—1
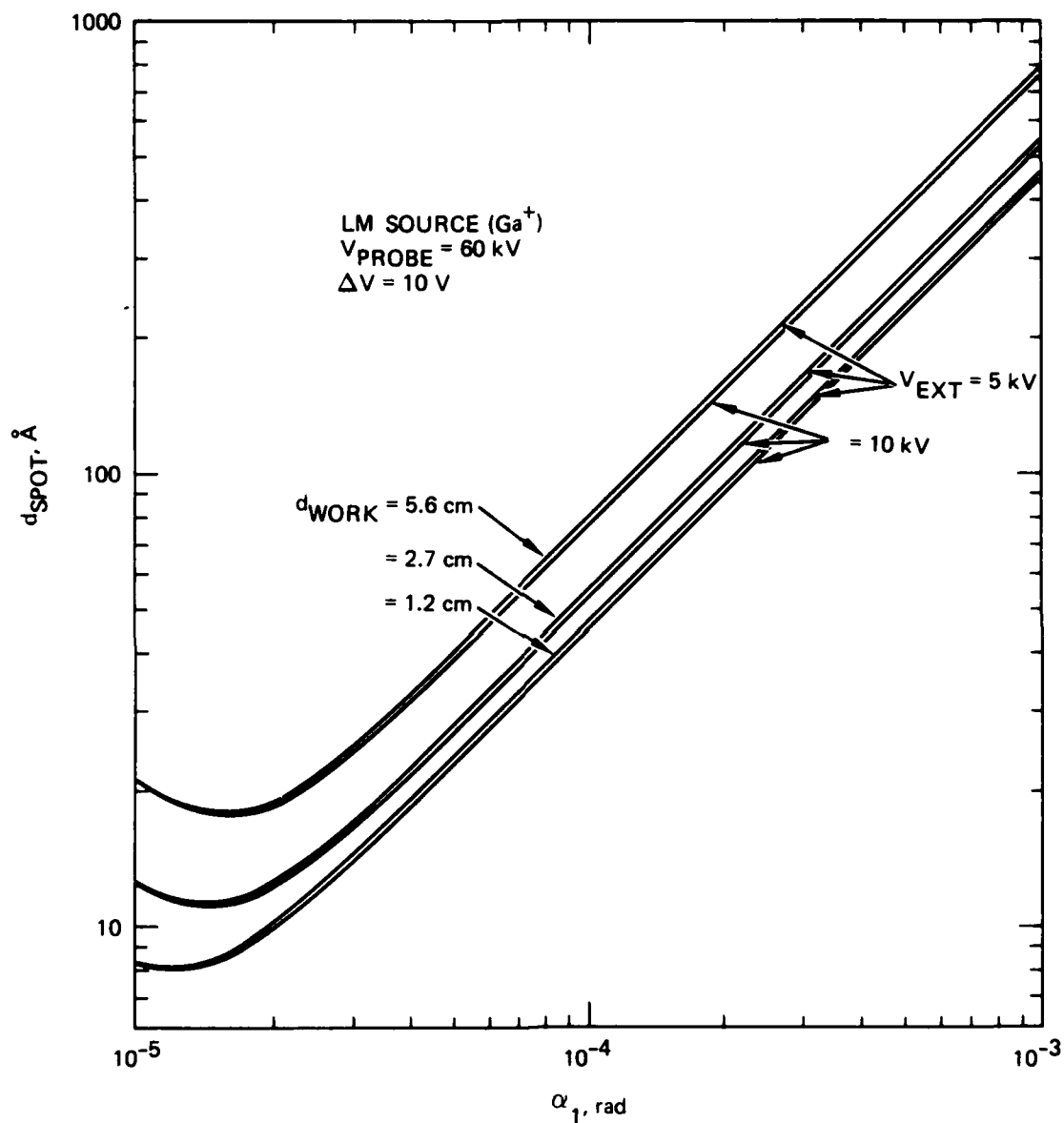
Fig. A3-3 Spot size as a function of aperture half-angle for LM source omitting effect of virtual source size. At V_{EXT} = 5 kV, the overall magnification of the system ranges between ∿0.1 and ∿0.4, increasing with d_{WORK}. At V_{EXT} = 30 kV, such range becomes ∿0,3 - 0.7.
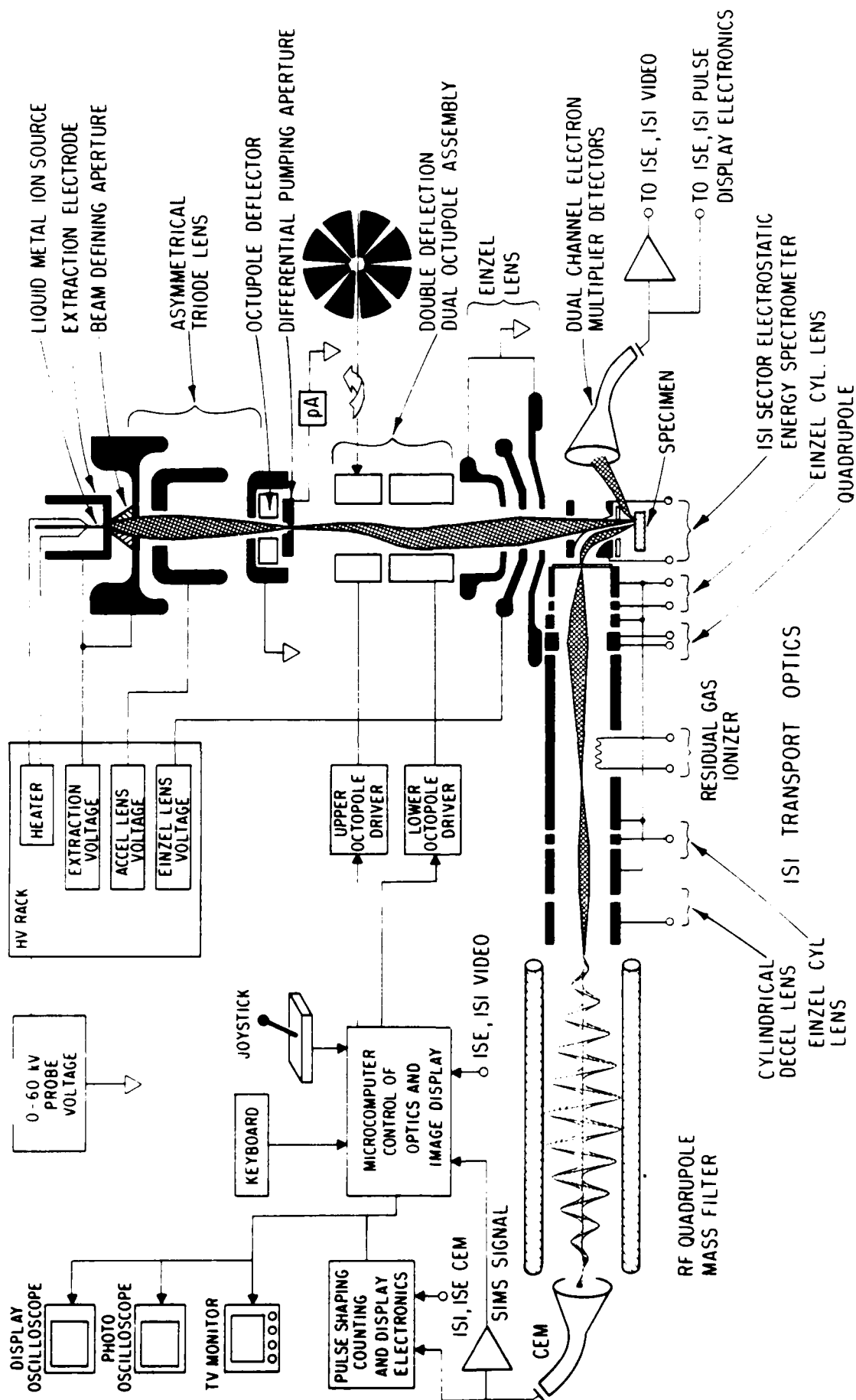
Fig. A3-4 Block diagram of UC-HRL microprobe system.
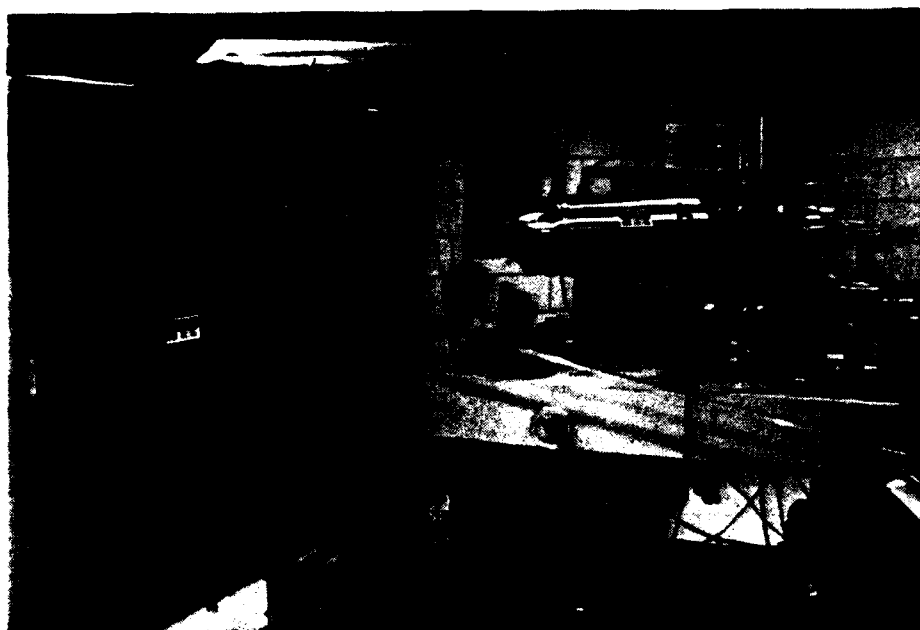
Fig. A3-5 Views of UC-HRL microprobe system.

a. High voltage electronics rack
b. SIM vacuum chamber
c. 450 ℓ/s ion pump (one of two)
d. Newport Corp. vibration isolation airlegs
e. Computer controller with CRT's, 8" floppy disk drives, keyboard and joystick
f. Raster scan controller
g. Imaging CRT's
h. Control electronics for Extra-Nuclear quadrupole mass analyzer
i. ATS control electronics
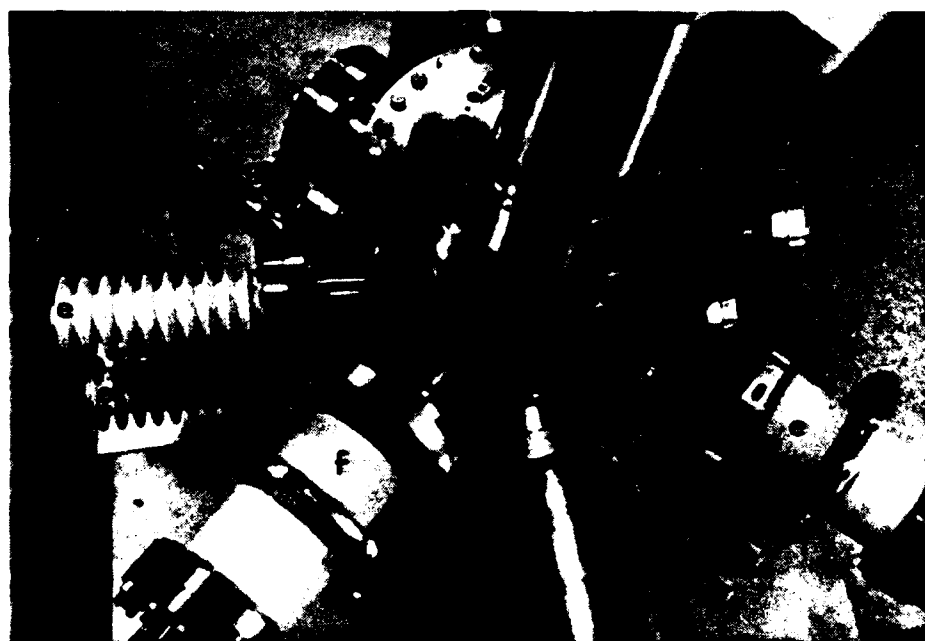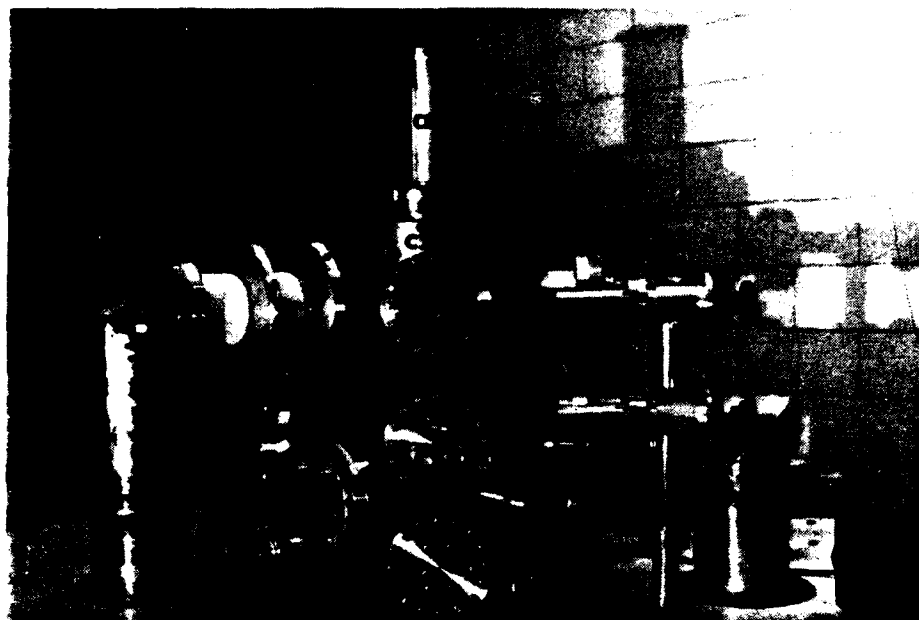
Fig. A3-6 Details of the mechanical construction of the UC-HRL microprobe.

    a. Dewer for gas field ionization source
    b. Roughing pump manifold
    c. View ports
    d. Micrometers controlling x, y and z position of sample stage
    e. Lens high voltage feedthroughs
    f. Liquid Metal Ion Source (LMIS) heater feedthrough
    g. Specimen insertion chamber

Fig. A3-7 Ion Microprobe Layout

Fig. A3-8 Microprobe Chamber Layout
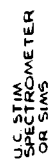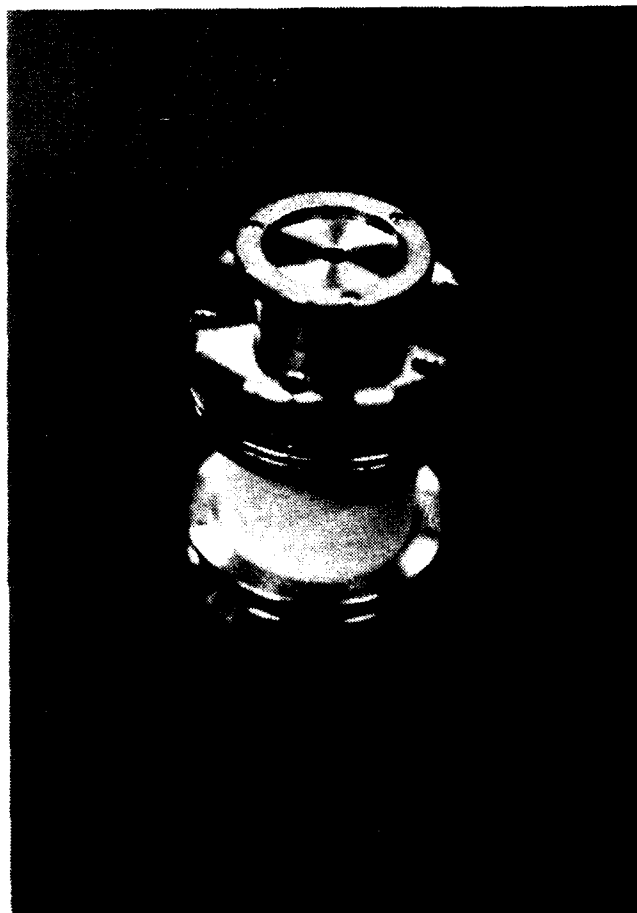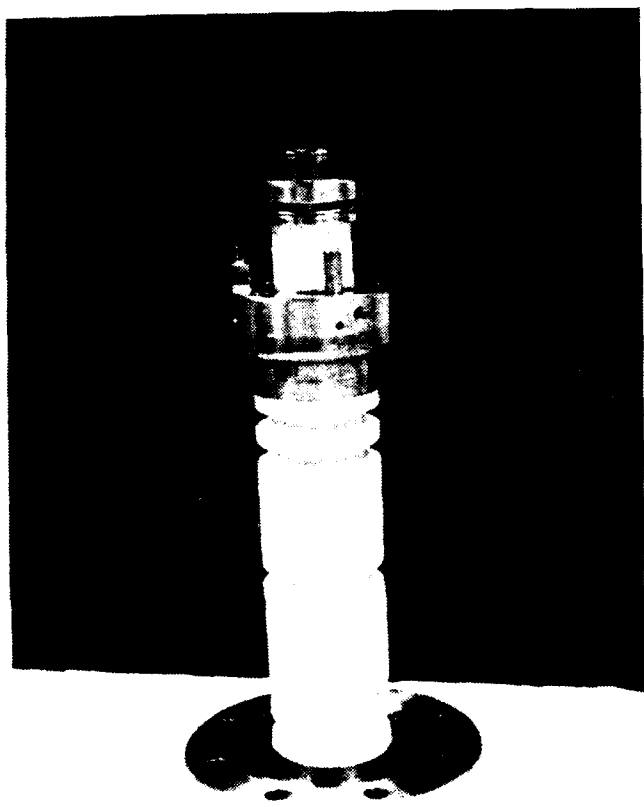
Fig. A3-9 Liquid metal ion source assembly mounted on a 60 kV insulator
(left), and close-up view of the source tantalum housing and
extraction aperture (right).
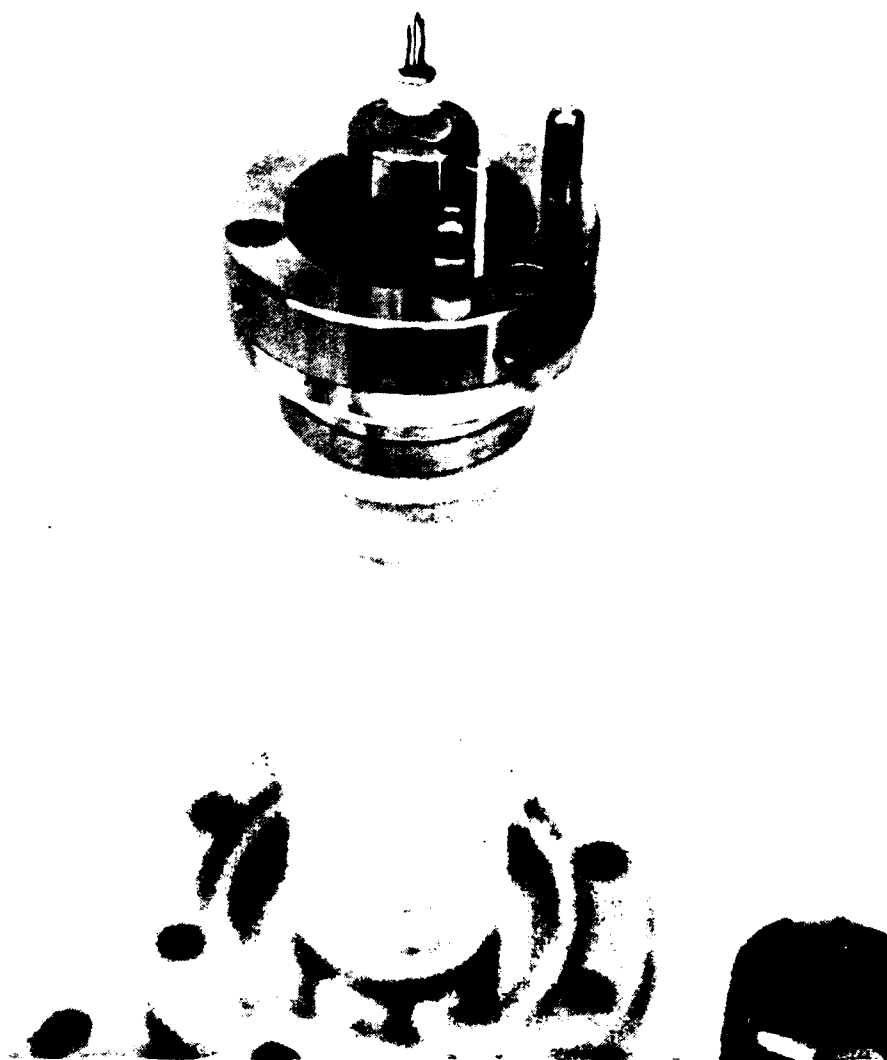
Fig. A3-10 Close-up view of liquid metal ion source in
           mounting, with extraction electrode removed.
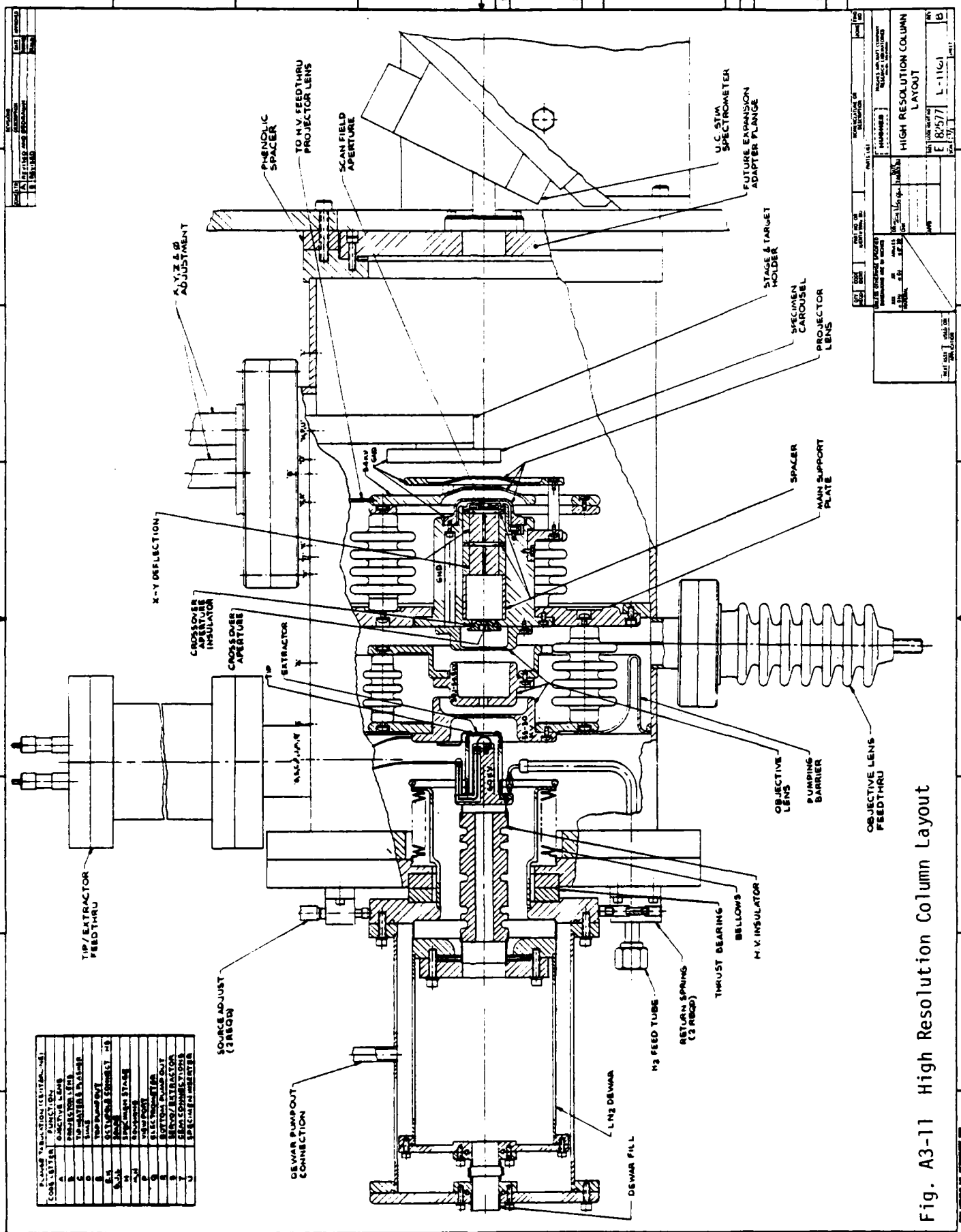
Fig. A3-11 High Resolution Column Layout
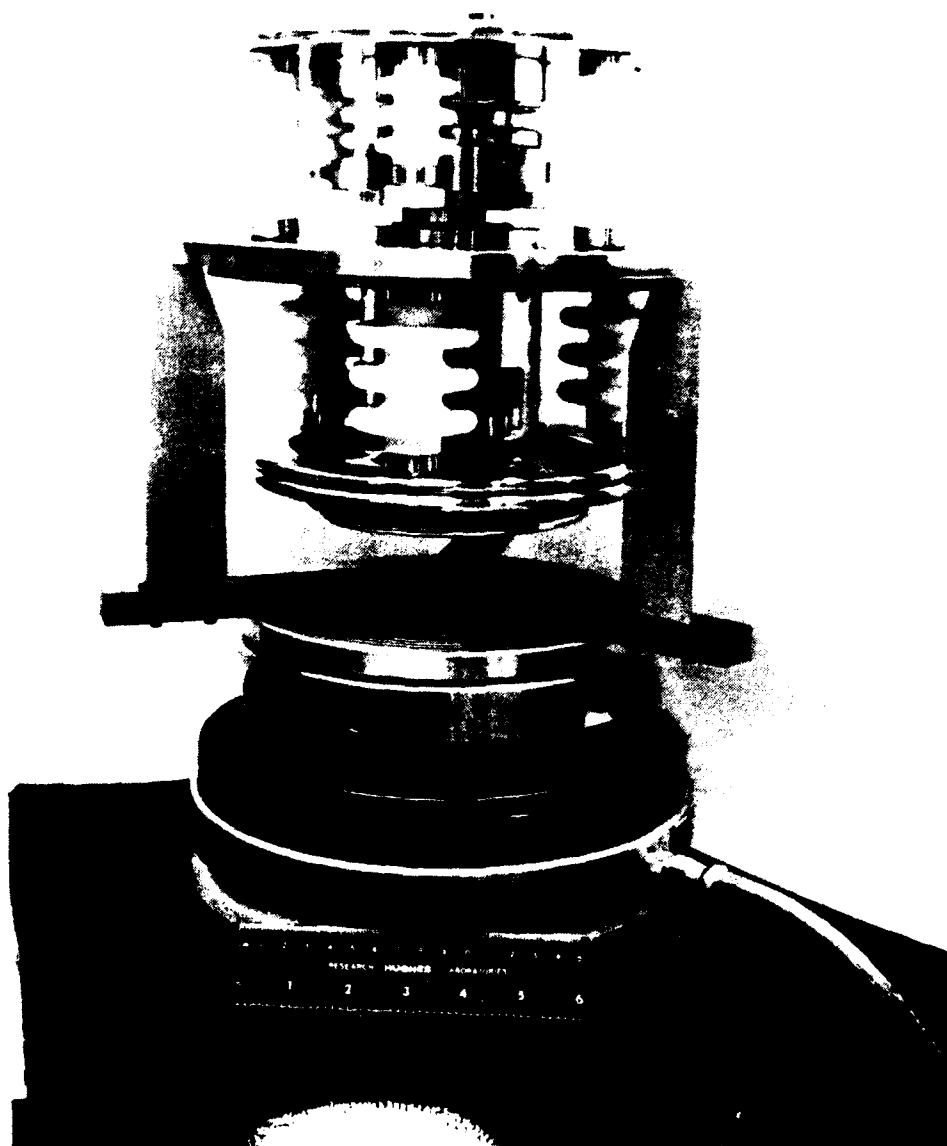
Fig. A3-12 Optical column mounted on rotary table for re-alignment.
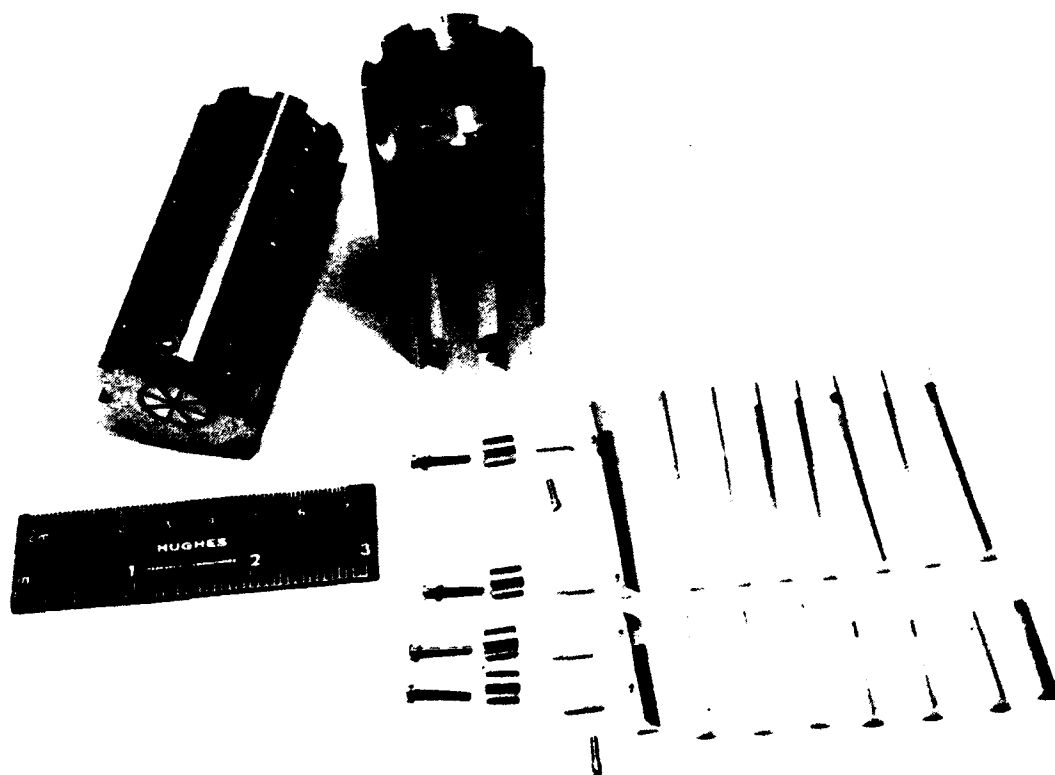
Fig. A3-13 Electrostatic octupoles assembly and octupole parts.
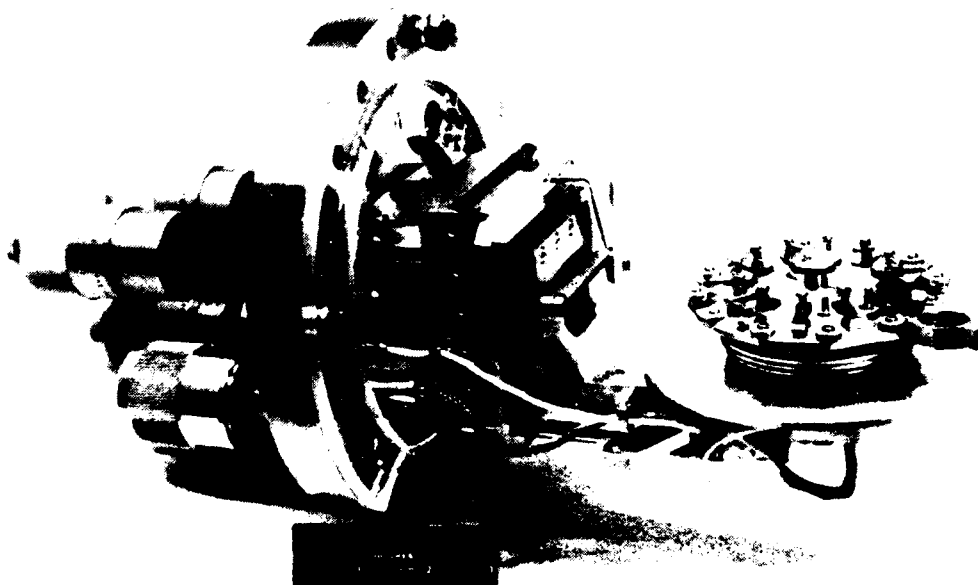
Fig. A3-14   Specimen stage and motions.
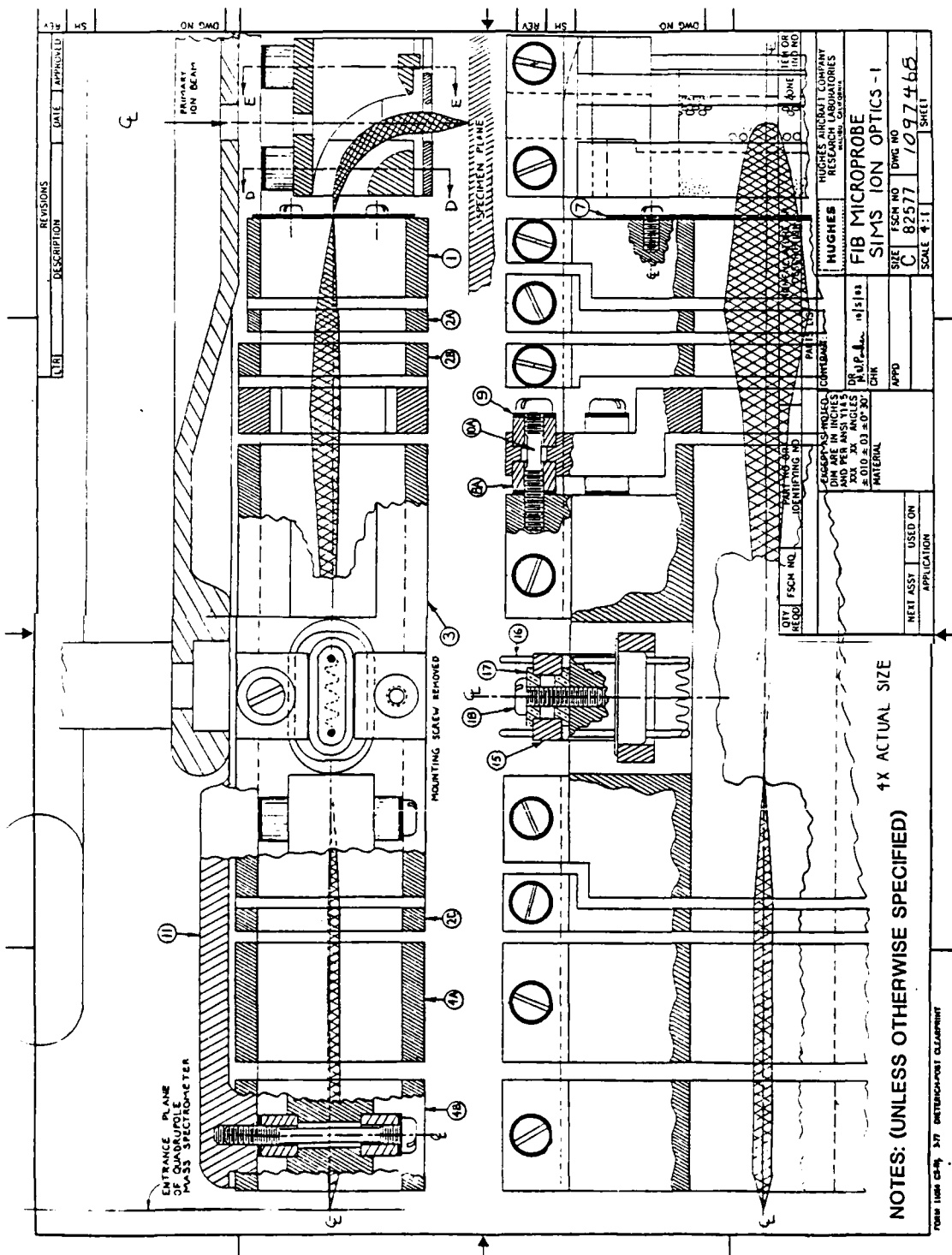
Fig. A3-15 Mechanical drawing of the ISI Analyzer and Transport System (ATS).

Fig. A3-16 ISI Analyzer and Transport System (ATS), together with ISI and ISE Channel Electron Multiplier detectors (CEM) for topographic imaging.

    a.   Channel electron multiplier detectors
    b.   ISI energy analyzer
    c.   ISI transport system

page 89
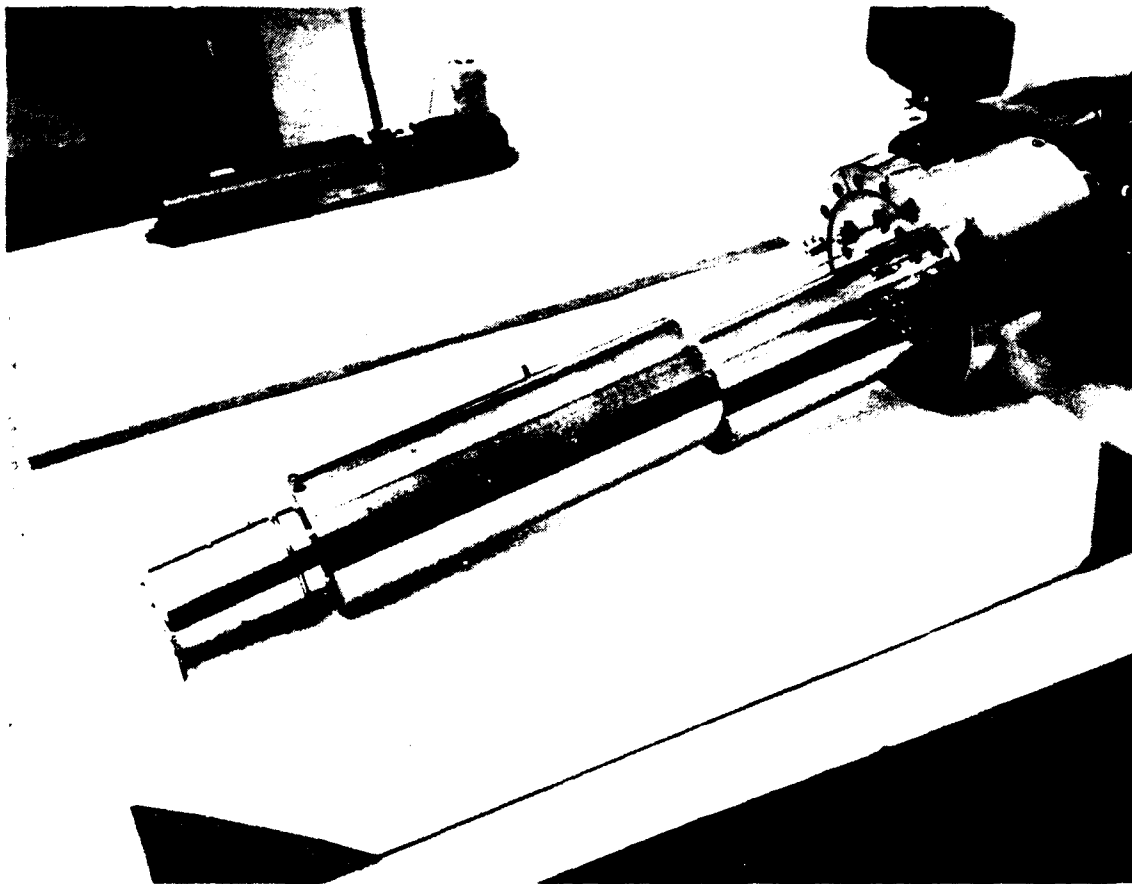
Fig. A3-17   Secondary ion quadrupole mass filter.
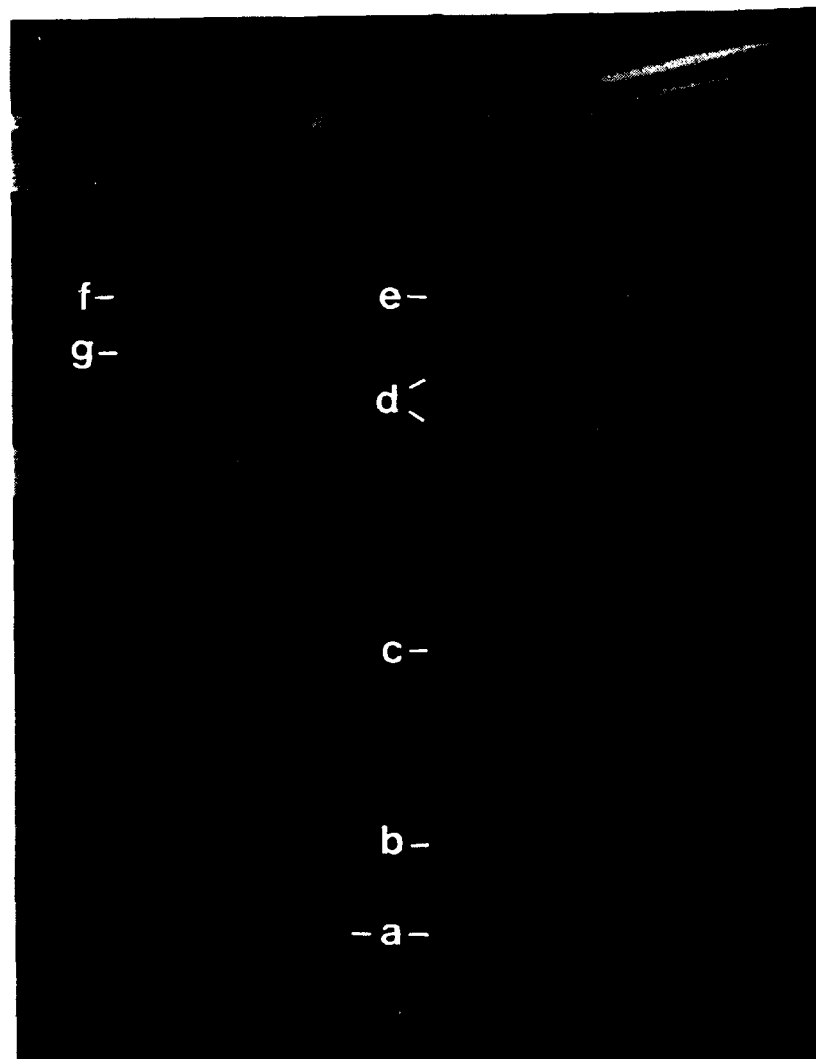
Fig. A3-18 High Voltage Electronics Rack

a. Ion pump power supplies.

b. 30 kV positive power supply for internal bias of the rack.

c. 30 kV positive acceleration power supply.

d. 30 kV negative power supplies for lenses.

e. 30 kV negative power supply for extraction of beam.

f. Low voltage power supply for heating of source

g. Digital ammeter to measure source current.

APPENDIX 4

PERFORMANCE EVALUATION

OF THE UC HRL-HIGH RESOLUTION

SCANNING ION MICROPROBE

A. PROBE DIAMETER AND

PROBE CURRENT STUDIES,

UC-HRL SIM

END

FILMED

DTIC
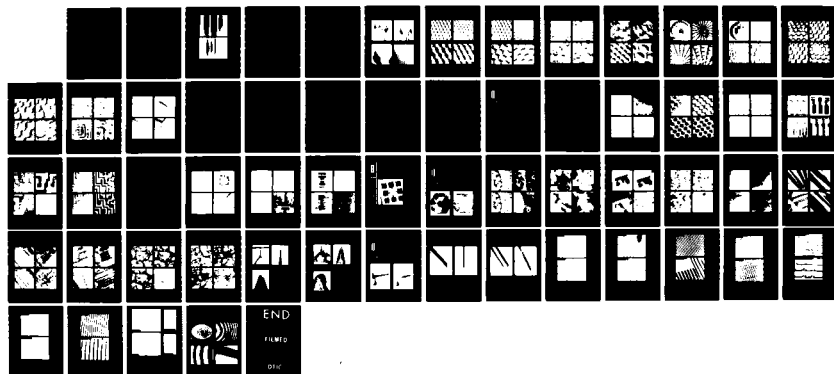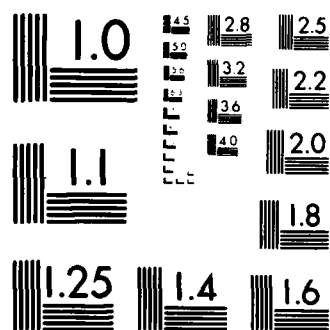
MICROCOPY RESOLUTION TEST CHART

NATIONAL BUREAU OF STANDARDS-1963 A
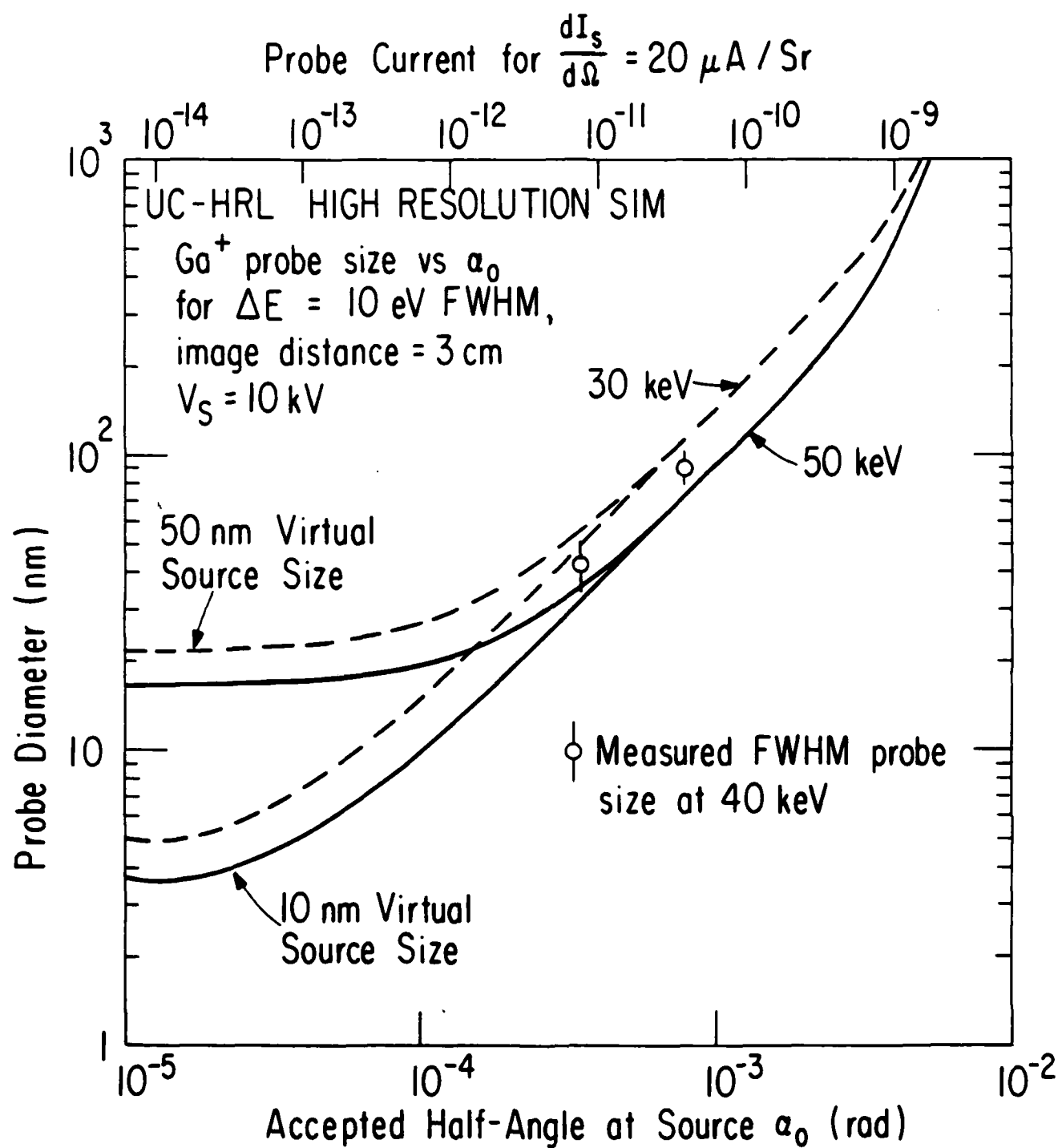
Fig. A4-1 Probe diameter versus beam acceptance half-angle at the source.
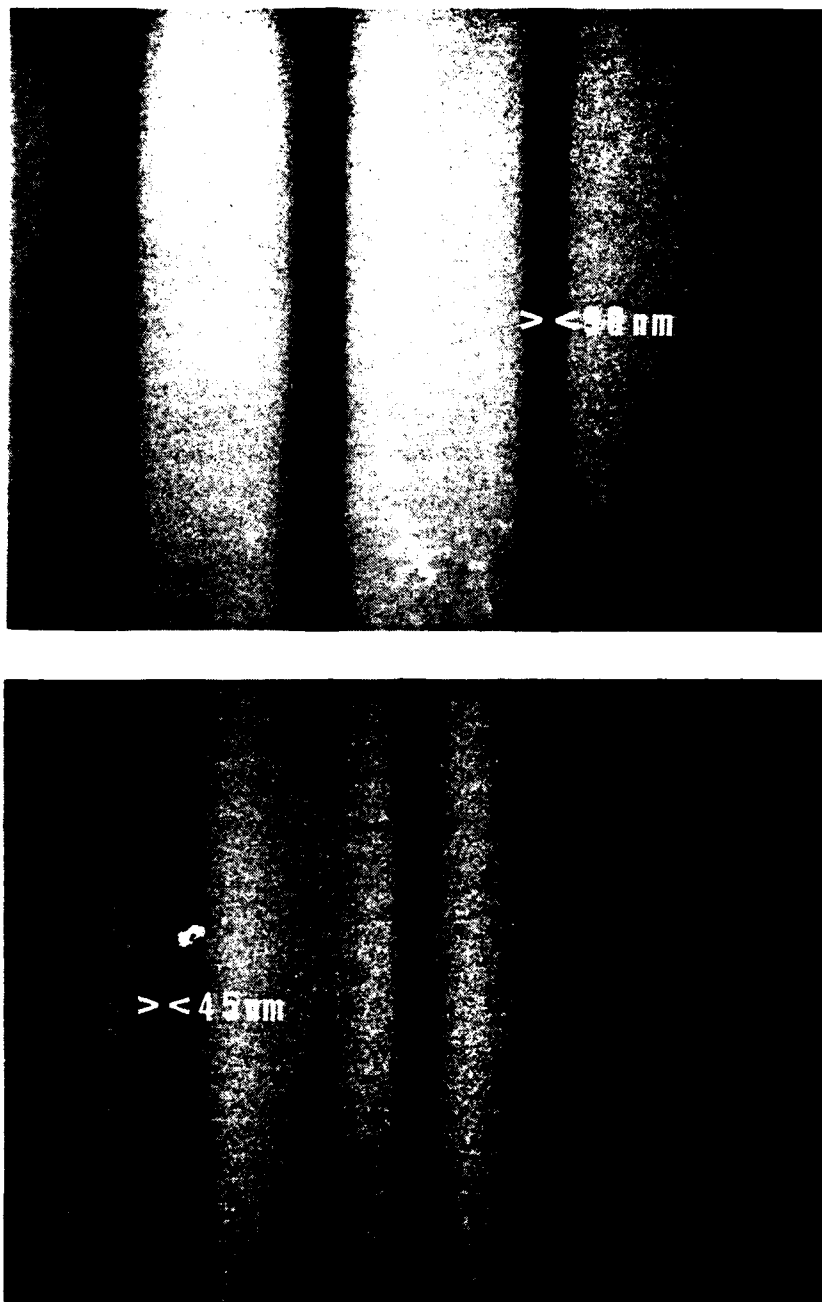
Fig. A4-2 Lines written on Au-coated Si wafers. SEM micrographs.

a). 25 μm beam aperture. 14 pA beam current. Doses of, from
left to right, 4.5×10^{-7} C/cm, 1.5×10^{-7} C/cm, 4.5×10^{-8} C/cm.

b). 12.5 μm beam aperture. 3.5 pA beam current. Doses of, from
left to right, 1.1×10^{-7}, 4×10^{-8}, 1.1×10^{-8} C/cm.
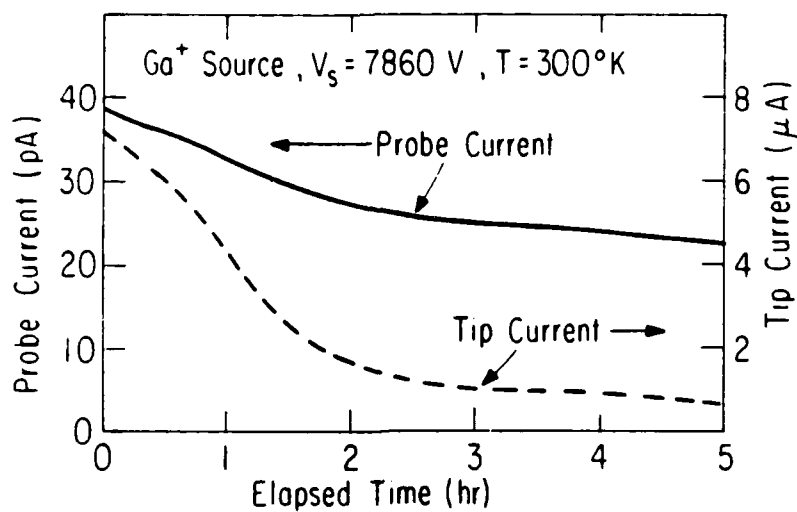
Fig. A4-3a   Plot of the time evolution of the
source current I_s and probe current I_p,
for a 5 hr. run at constant extraction
voltage.
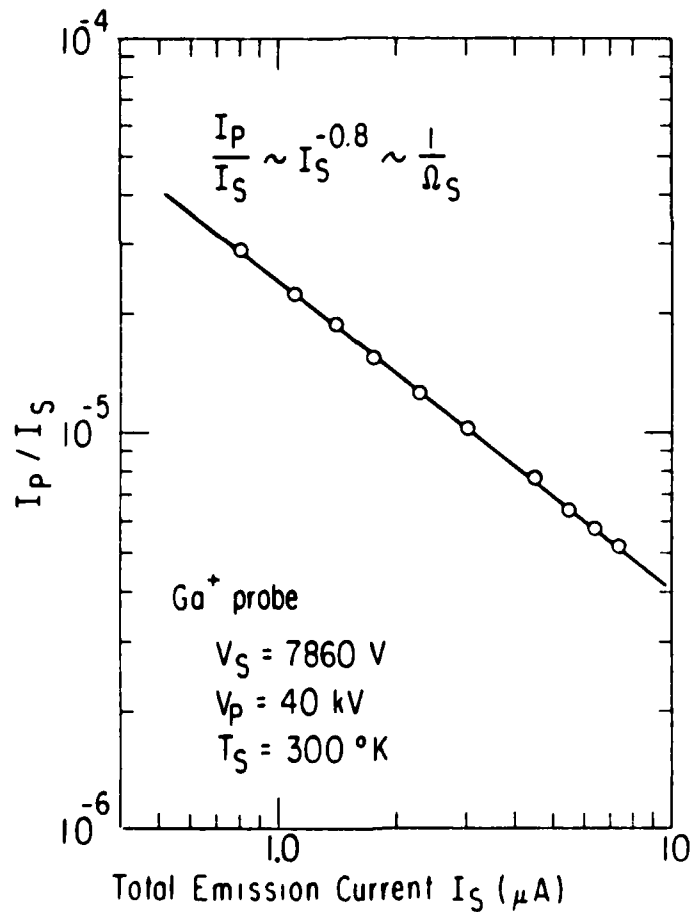
Fig. A4-3b   Transmission ratio I_s/I_p vs. I_s
obtained from the data in Fig. 3.   The
plot indicates an expansion of the solid
angle Ω_s of source emission proportional
to $I_s^{0.8}$.

B. IMAGING PERFORMANCE OF UC-HRL SIM

SECONDARY ELECTRONS AND

SECONDARY ION IMAGES

Ga⁺ FOCUSED-ION-BEAM IMAGES
DROSOPHILA MELANOGASTER, UNCOATED
SECONDARY ELECTRON SIGNAL, PULSE-MODE DISPLAY
UC-HRL SIM (39 keV Ga⁺ IONS)

1710 μM FULL SCALE

855 μM F.S.

427 μM F.S.

213 μM F.S.

U.C., Nov. 1983   page 98   FIG. A4-4
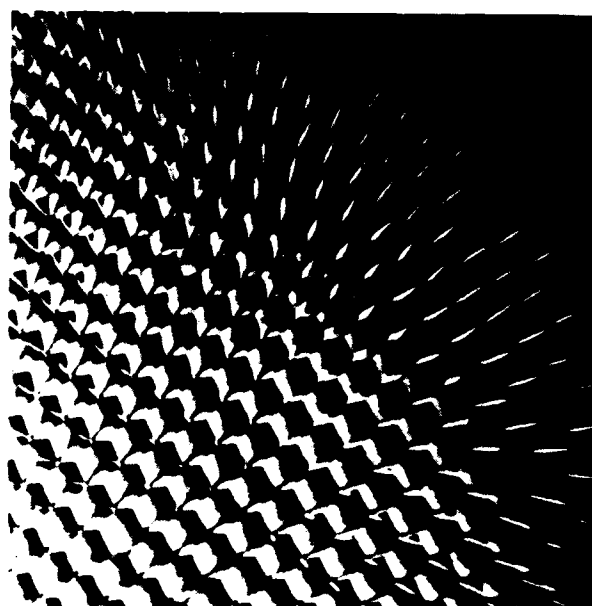
GA⁺ FOCUSED-ION-BEAM IMAGES
DROSOPHILA MELANOGASTER, UNCOATED
ISE vs ISI IMAGES, (PULSE-MODE DISPLAY)
UC-HRL SIM (39 KEV GA⁺ IONS)

ISE

ISI
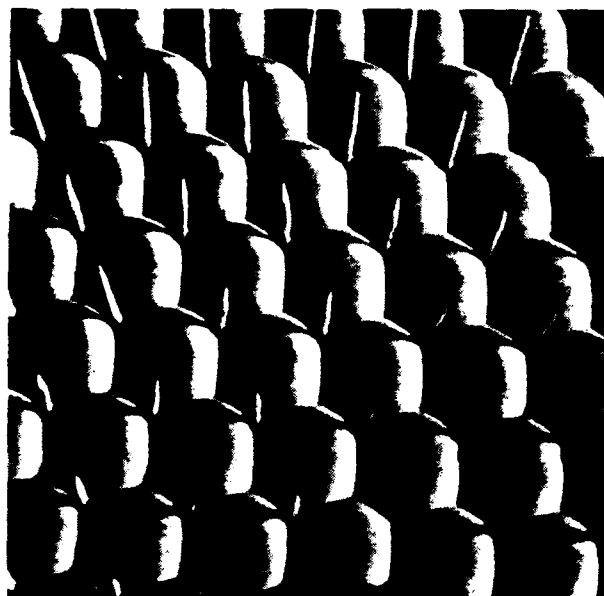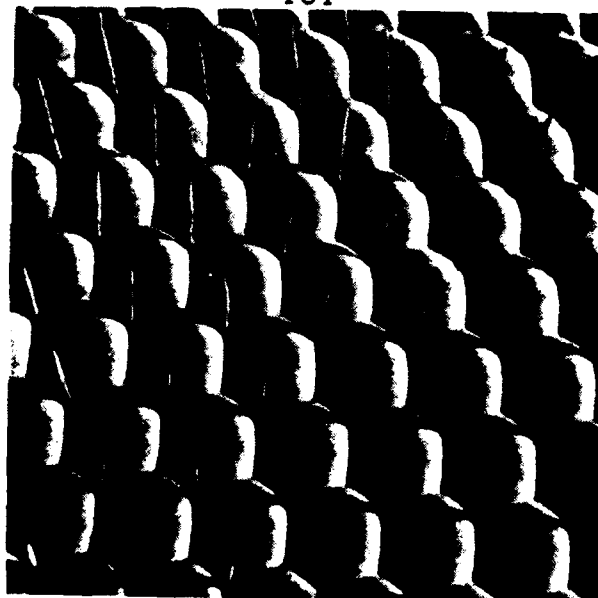
90 μM FULL SCALE

100 μM F.S.

45 μM F.S.

50 μM F.S.

Ga⁺ FOCUSED-ION-BEAM IMAGES

Ga^+ FOCUSED-ION-BEAM IMAGES
DROSOPHILA MELANOGASTER, UNCOATED
ISE IMAGES, PULSE-MODE VS. ANALOG VIDEO DISPLAY
UC-HRL SIM (39 KEV Ga^+ IONS)
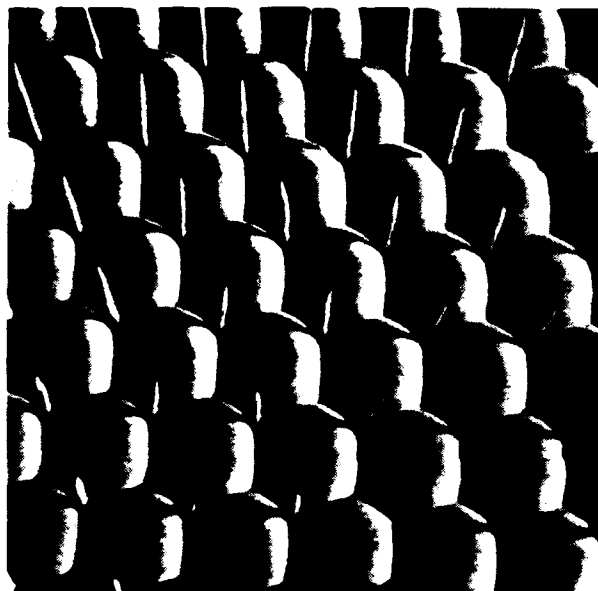
PULSE-MODE

ANALOG-MODE

90 μM FULL SCALE
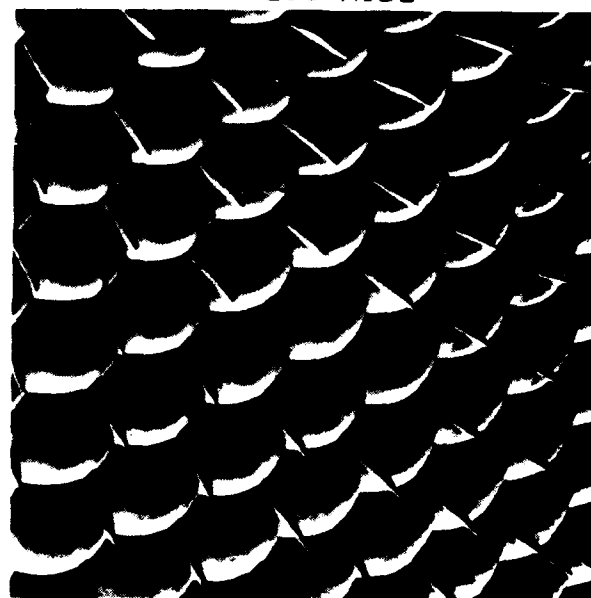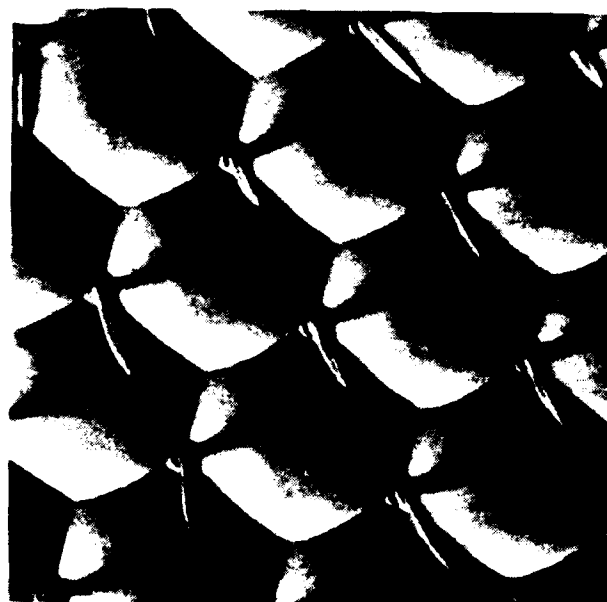
90 μM F.S.

45 μM F.S.

45 μM F.S.

Ga^+ FOCUSED-ION-BEAM IMAGES
HUMAN ERYTHROCYTES, CRITICAL POINT DRIED, UNCOATED
ISE vs ISI IMAGES, (ANALOG -MODE DISPLAY)
UC-HRL SIM (39 KEV Ga^+ IONS)

ISE   ISI

50 µM FULL SCALE

25 µM FULL SCALE

U.C., Nov. 1983   page 101   FIG. A4-7

GA^+ FOCUSED-ION-BEAM IMAGES
ISE IMAGES OF MINERALS, UNCOATED
UC-HRL SIM (39 KEV GA^+ IONS)

PYRITE ON $CACO_3$ — PYRITE

450 µM FULL SCALE
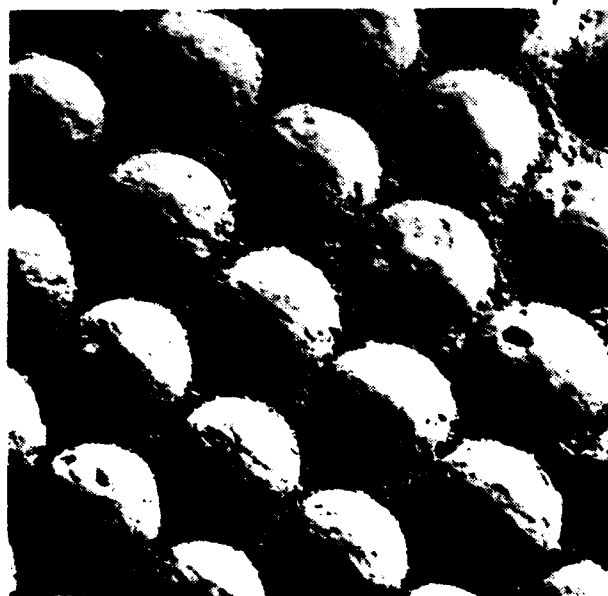
$CACO_3$ — 900 µM FULL SCALE — $CACO_3$
(TRILOBITE EYE) — (TRILOBITE EYE)

Ga^+ FOCUSED-ION-BEAM IMAGES
FOSSIL DIATOMS (SiO_2), UNCOATED
SECONDARY ELECTRON SIGNAL (PULSE MODE DISPLAY)
UC-HRL SIM (39 KEV Ga^+ IONS)
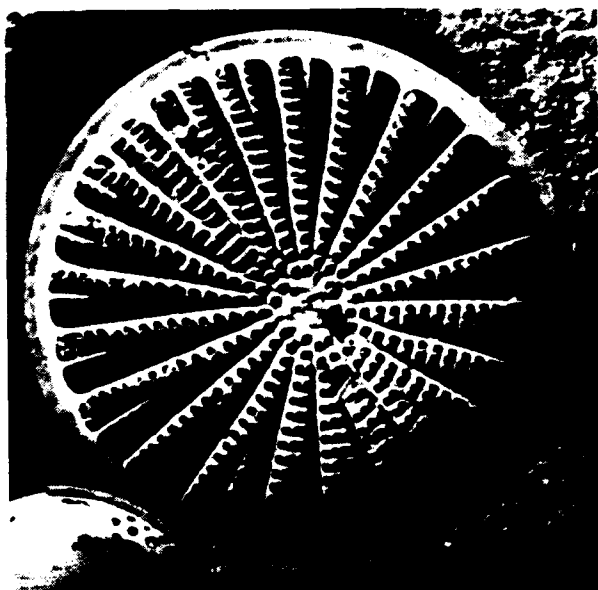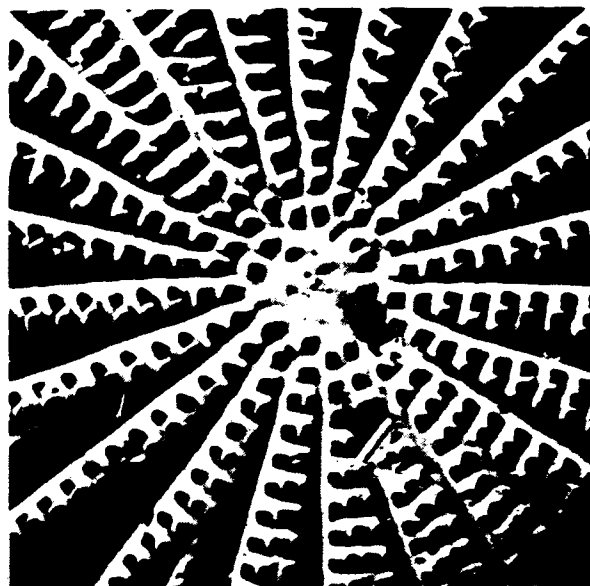
200 μM FULL SCALE

100 μM F.S.
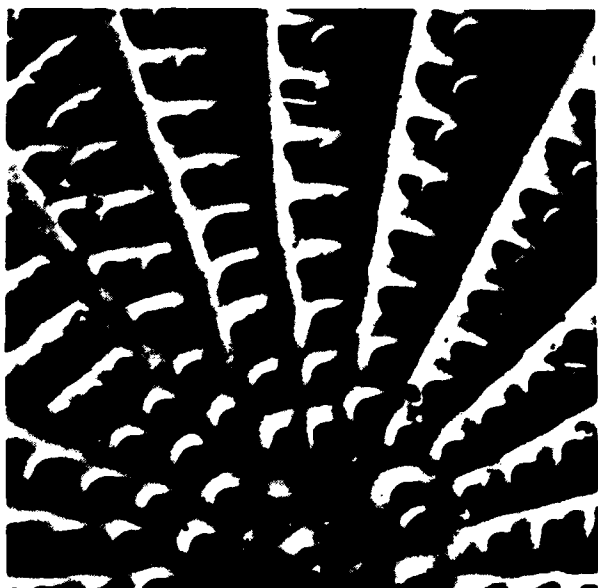
50 μM F.S.

25 μM F.S.

Ga$^+$ FOCUSED-ION-BEAM IMAGES
FOSSIL DIATOM (SiO$_2$), UNCOATED
SECONDARY ELECTRON SIGNAL (PULSE MODE DISPLAY)
UC-HRL SIM (39 KEV Ga$^+$ IONS)
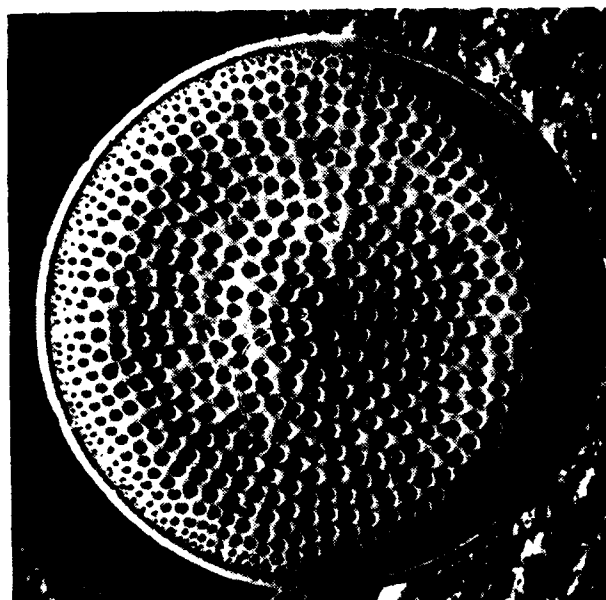
100 µM FULL SCALE
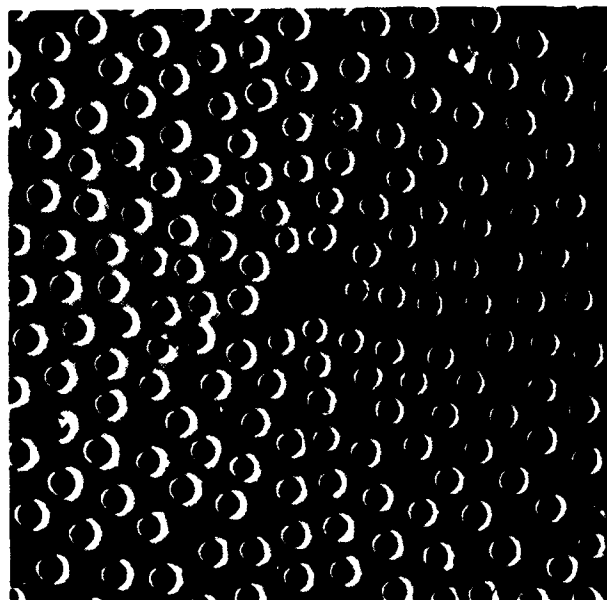
50 µM F.S.
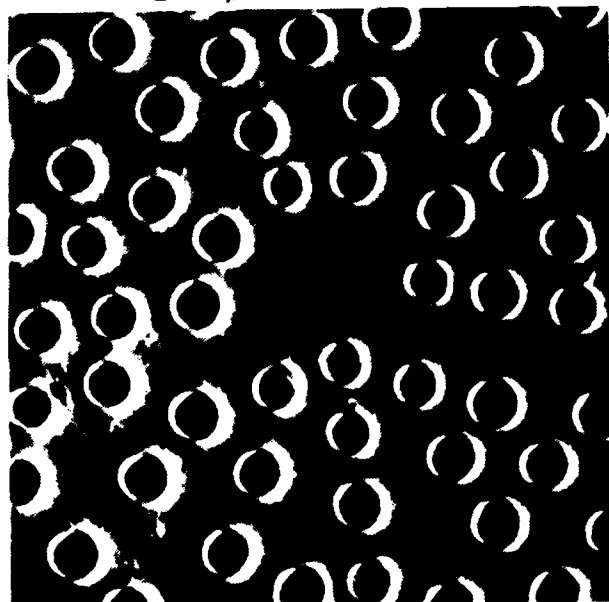
25 µM F.S.
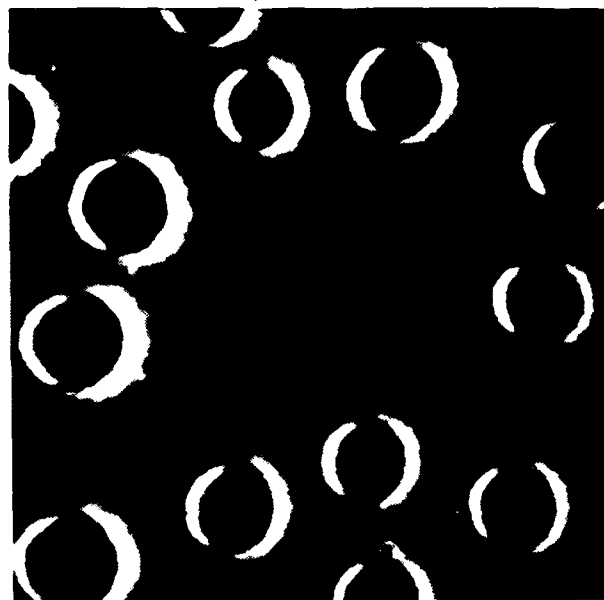
12.5 µM F.S.

Ga⁺ FOCUSED-ION-BEAM IMAGES
FOSSIL DIATOM (SiO_2), UNCOATED
ISI IMAGES OF PROGRESSIVE EROSION BY ION BOMBARDMENT
UC-HRL SIM (39 KEV Ga⁺ IONS)

1×10^{15} IONS/CM^2
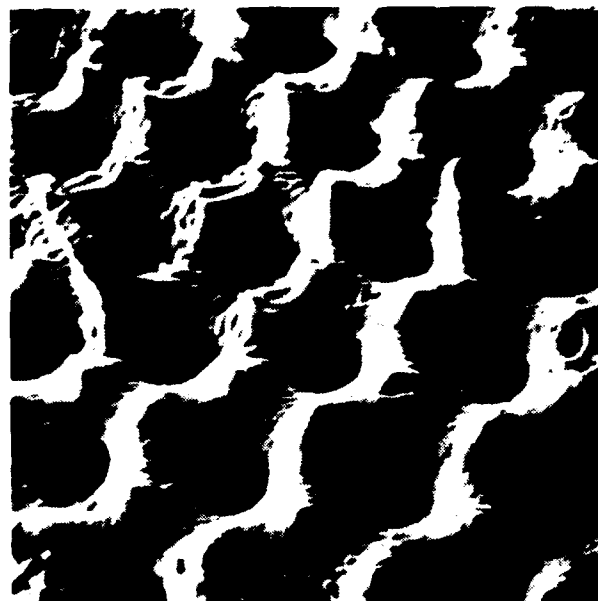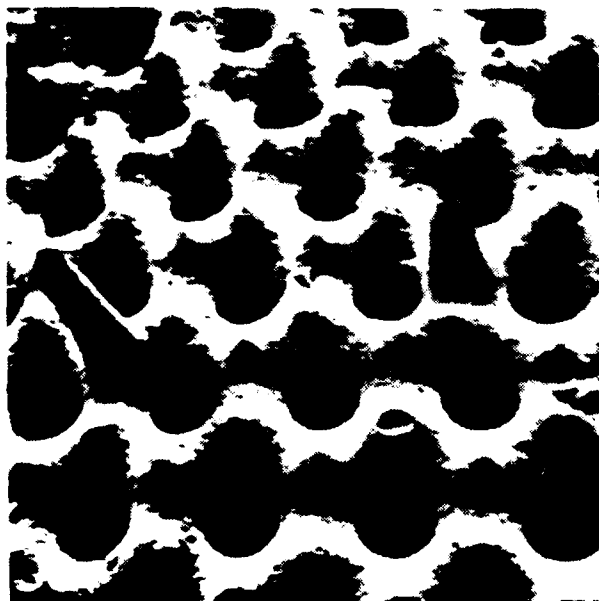
25 µM FULL SCALE

$3 \times 10^{16} - 5 \times 10^{17}$ IONS/CM^2

U.C., FEB. 1984   page 105   FIG. A4-11
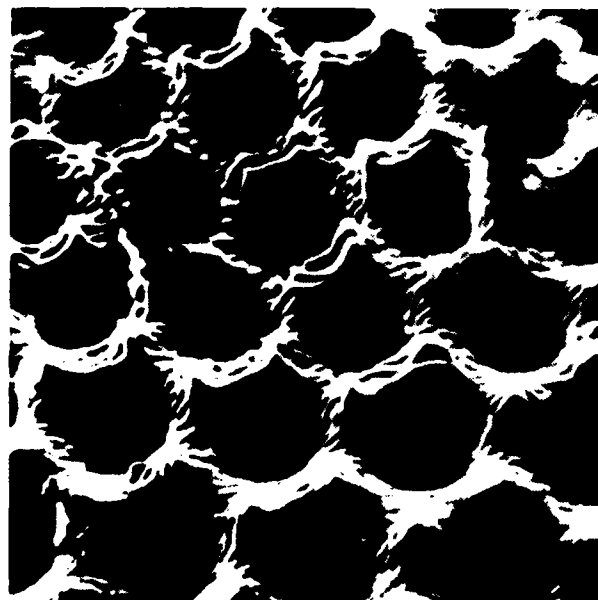
Ga$^+$ FOCUSED-ION-BEAM IMAGES
FOSSIL DIATOM (SI)$_2$), UNCOATED
ISI IMAGES OF PROGRESSIVE EROSION BY ION BOMBARDMENT
UC-HRL SIM (39 KEV Ga$^+$ IONS)

5×10^{15} IONS/CM^2 1×10^{17} IONS/CM^2

12.5 μM FULL SCALE

1×10^{17} IONS/CM^2 5×10^{17} IONS/CM^2

U.C., FEB. 1984   page 106   FIG. A4-12
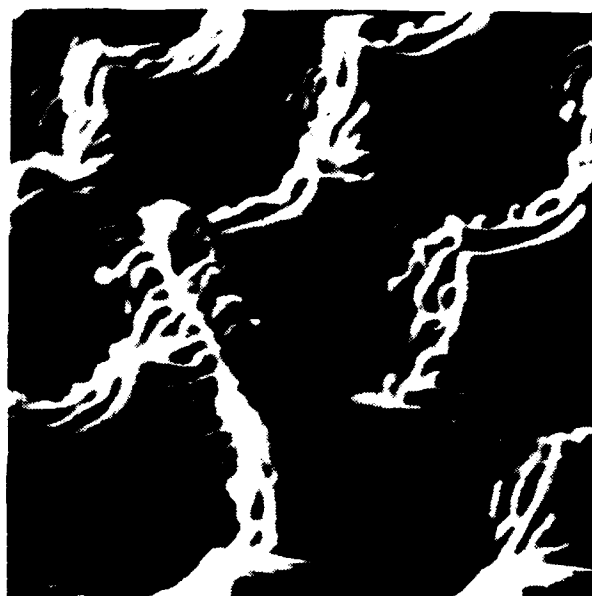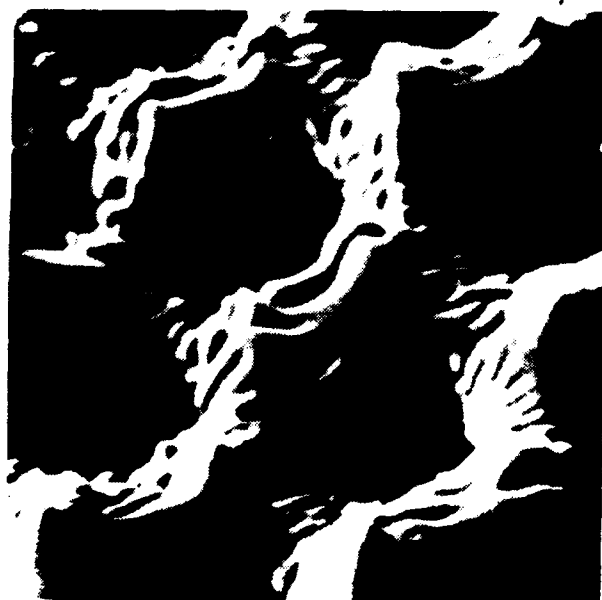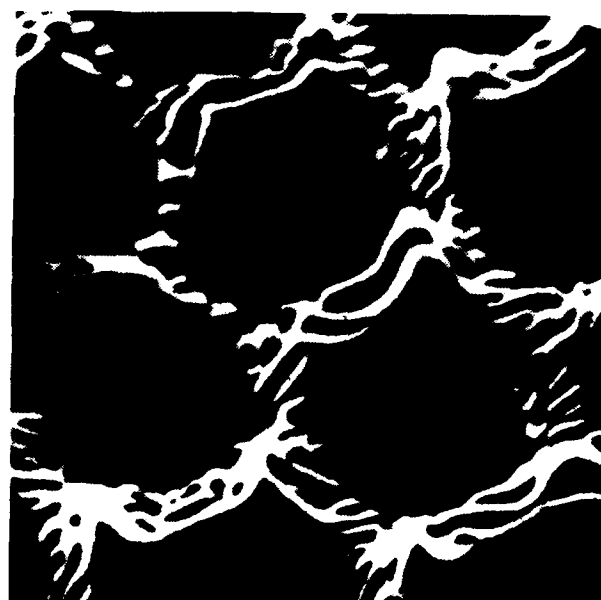
Ga$^+$ FOCUSED-ION-BEAM IMAGES
ISE IMAGES OF INTEGRATED CIRCUITS
UC-HRL SIM (39 keV Ga$^+$ IONS)
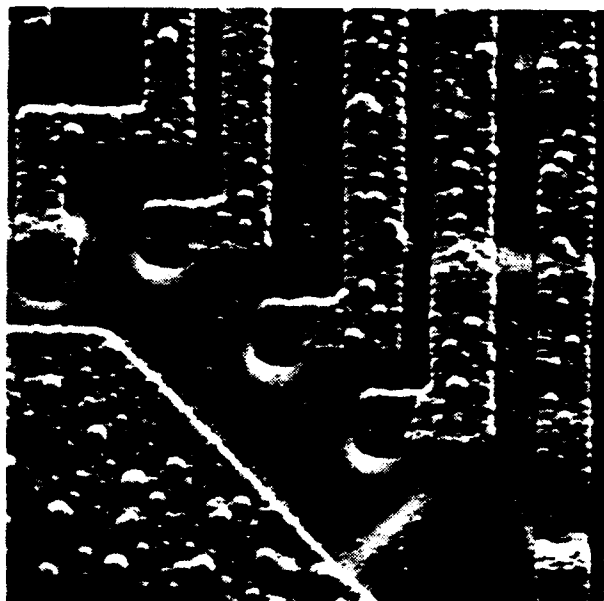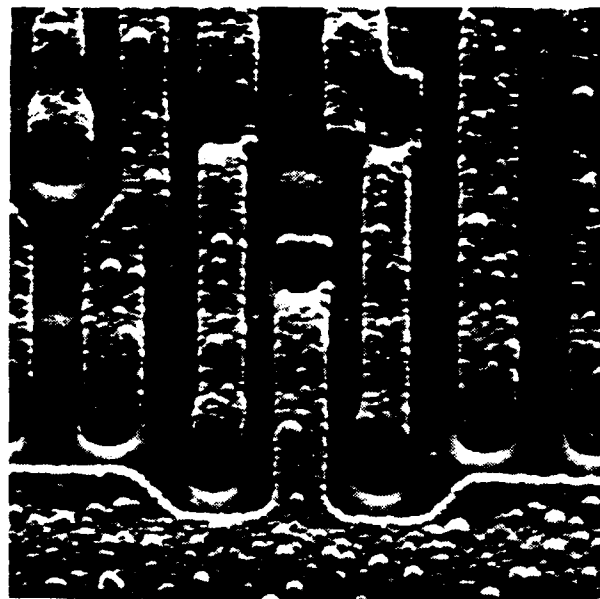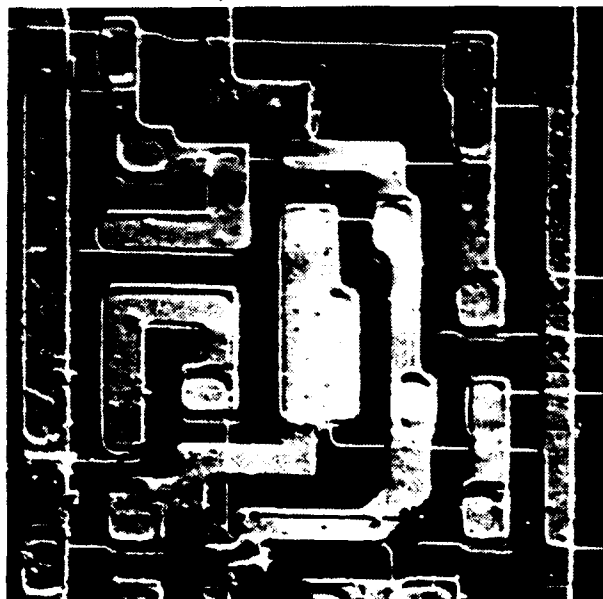
200 μM FULL SCALE

200 μM F.S.

100 μM FULL SCALE

50 μM F.S.
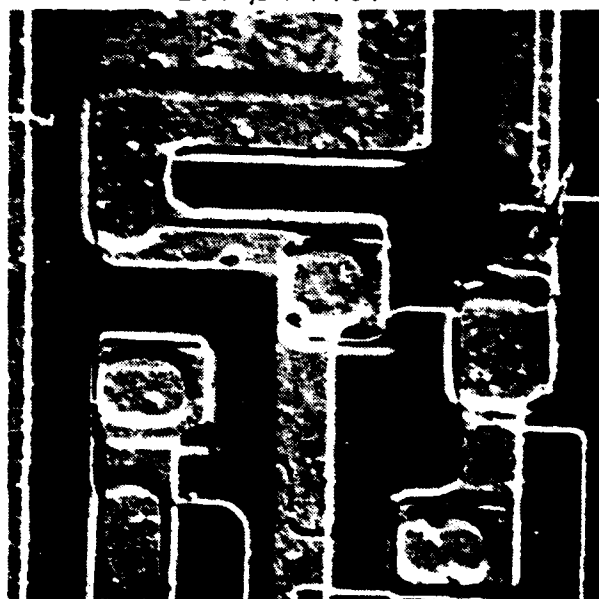
Ga$^+$ FOCUSED -ION-BEAM IMAGES
RECRYSTALLIZED, POLISHED, HNO$_3$-ETCHED COPPER
CRYSTALLOGRAPHIC CONTRAST IN ISE AND ISI IMAGES
UC-HRL SIM (39 keV Ga$^+$ IONS)

ISE   ISI

50 µM FULL SCALE
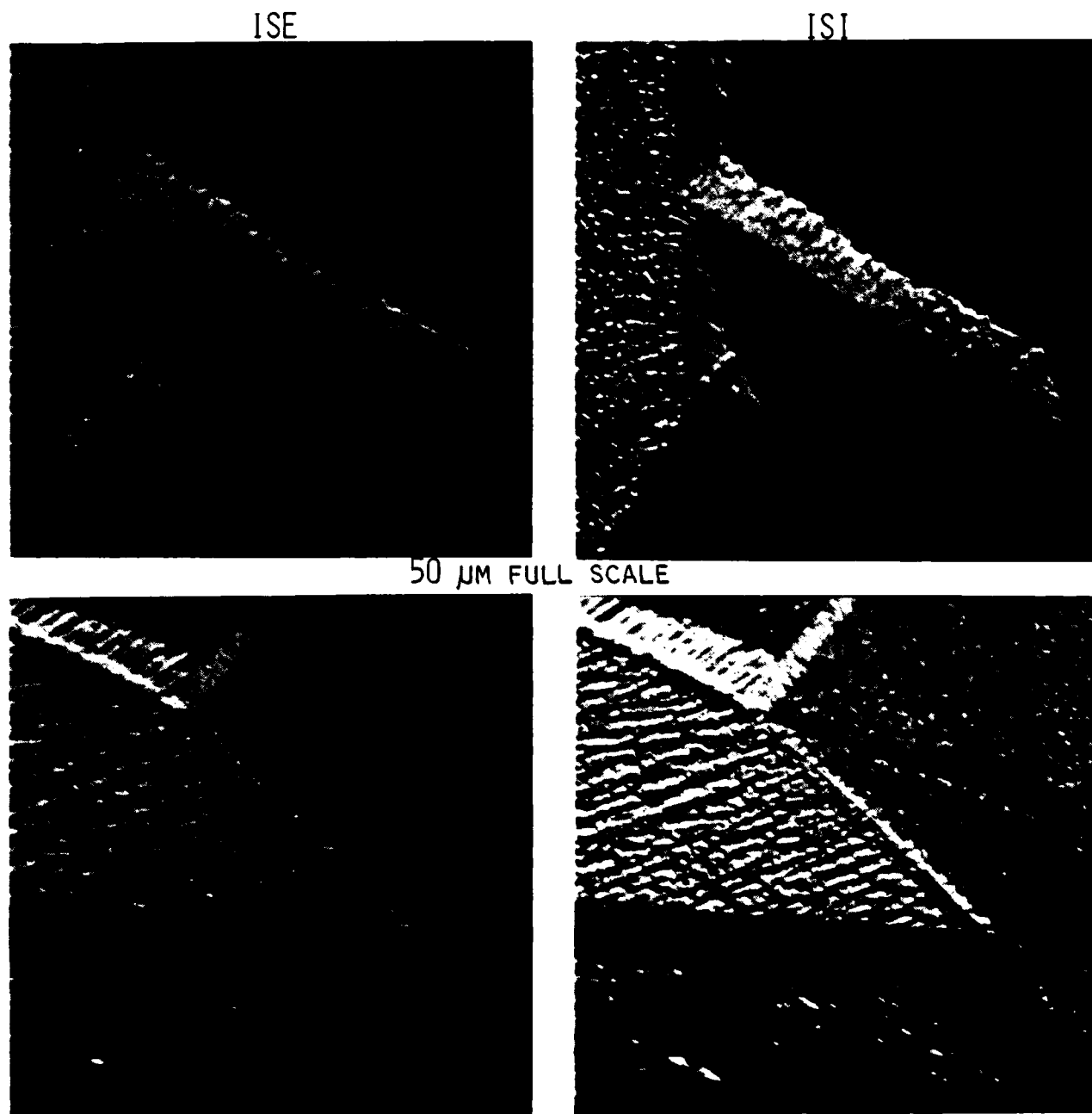
C. SIMS MICROANALYSIS

PERFORMANCE OF UC-HRL SIM:

MASS SPECTRA
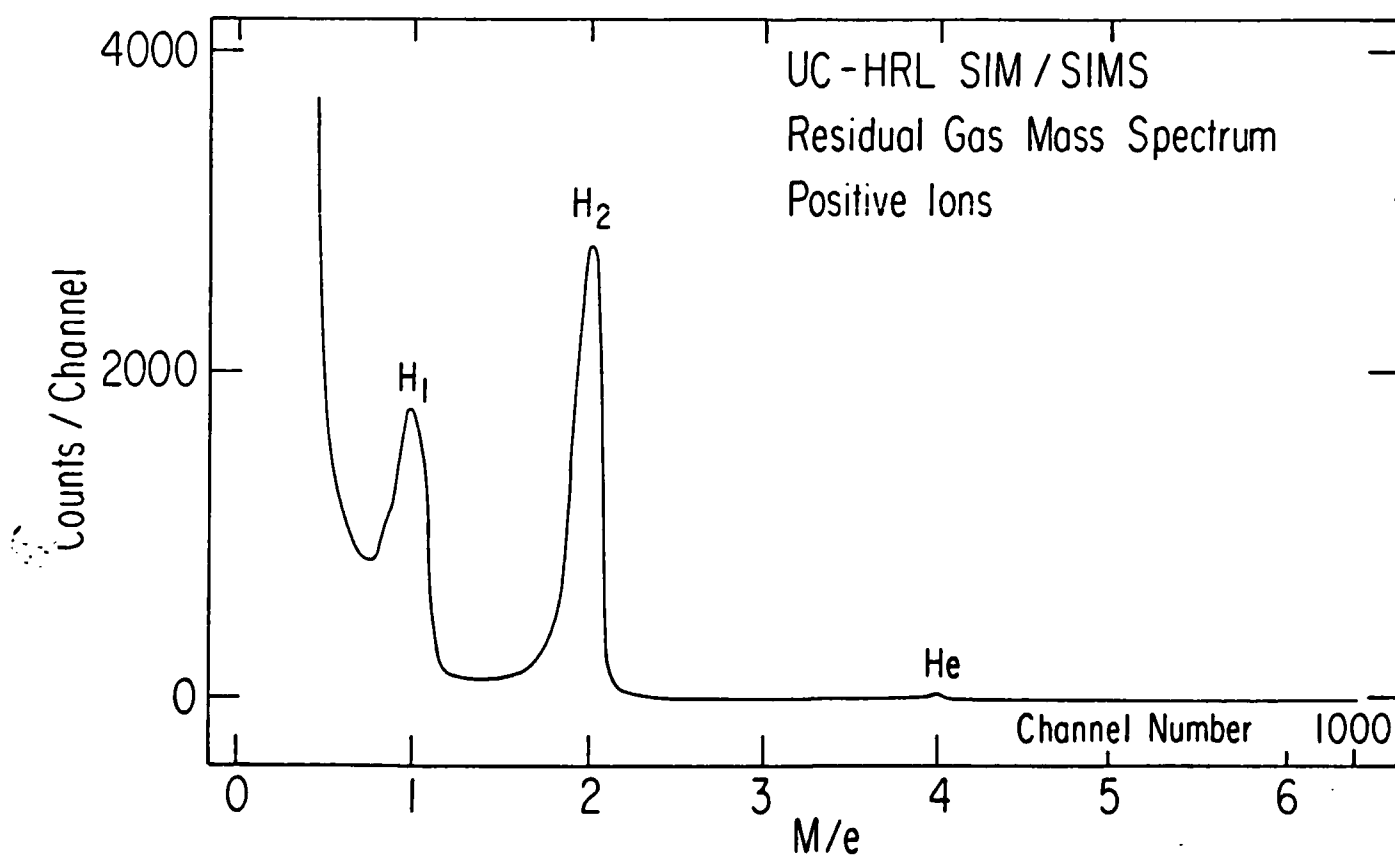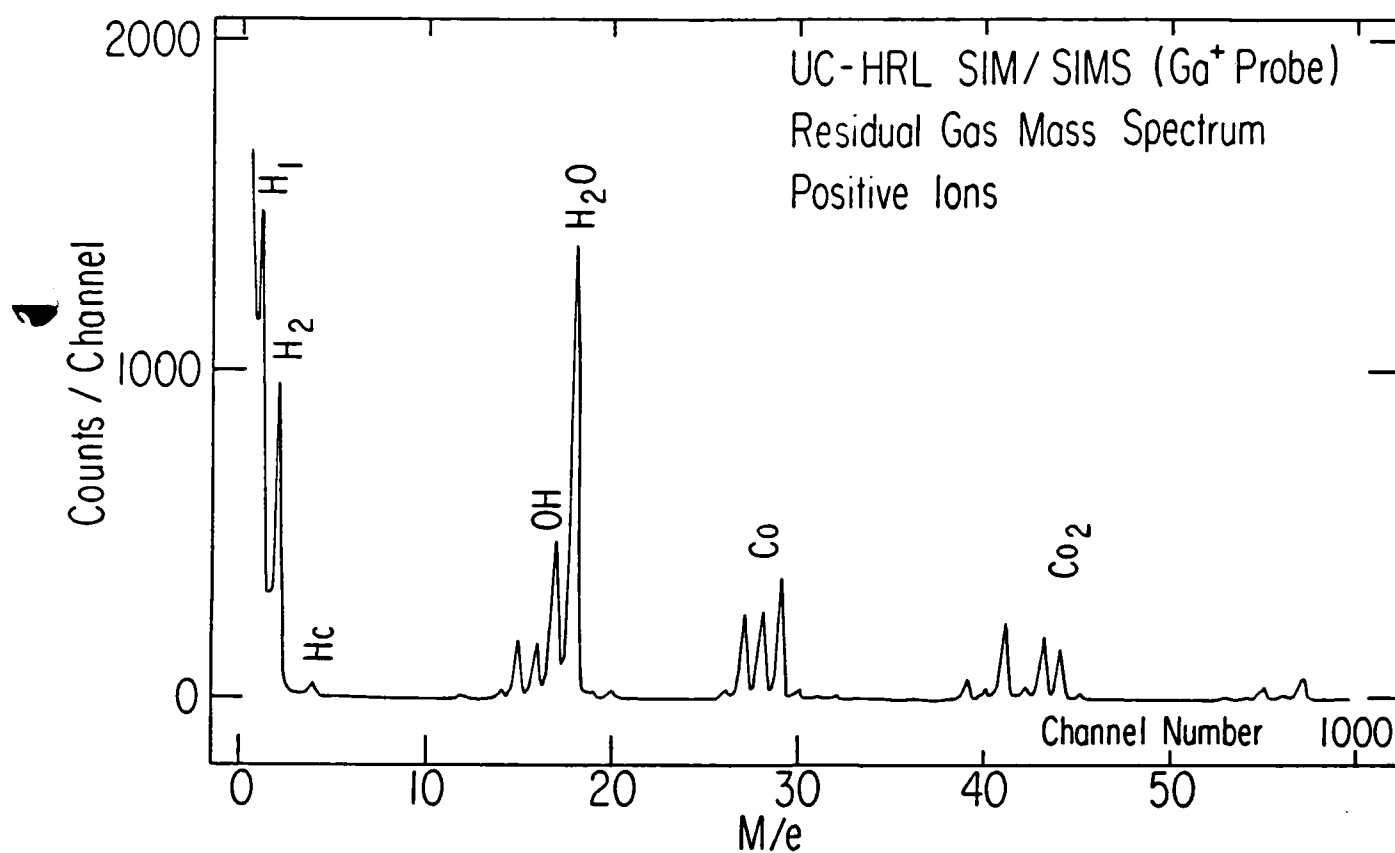
Fig. A4-15 Mass spectrum of the residual gas in the vacuum chamber.
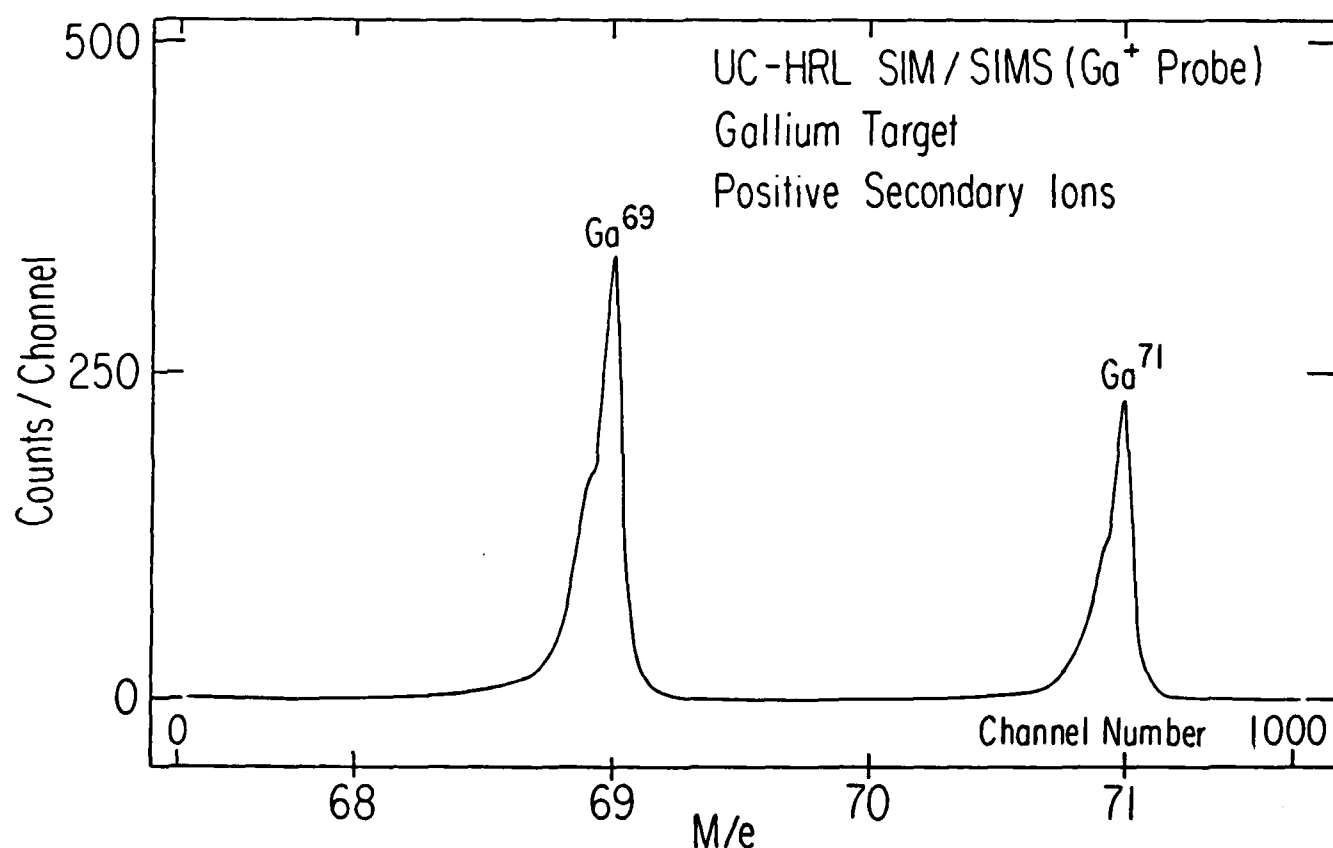
Fig. A4-16 Mass spectrum of gallium.
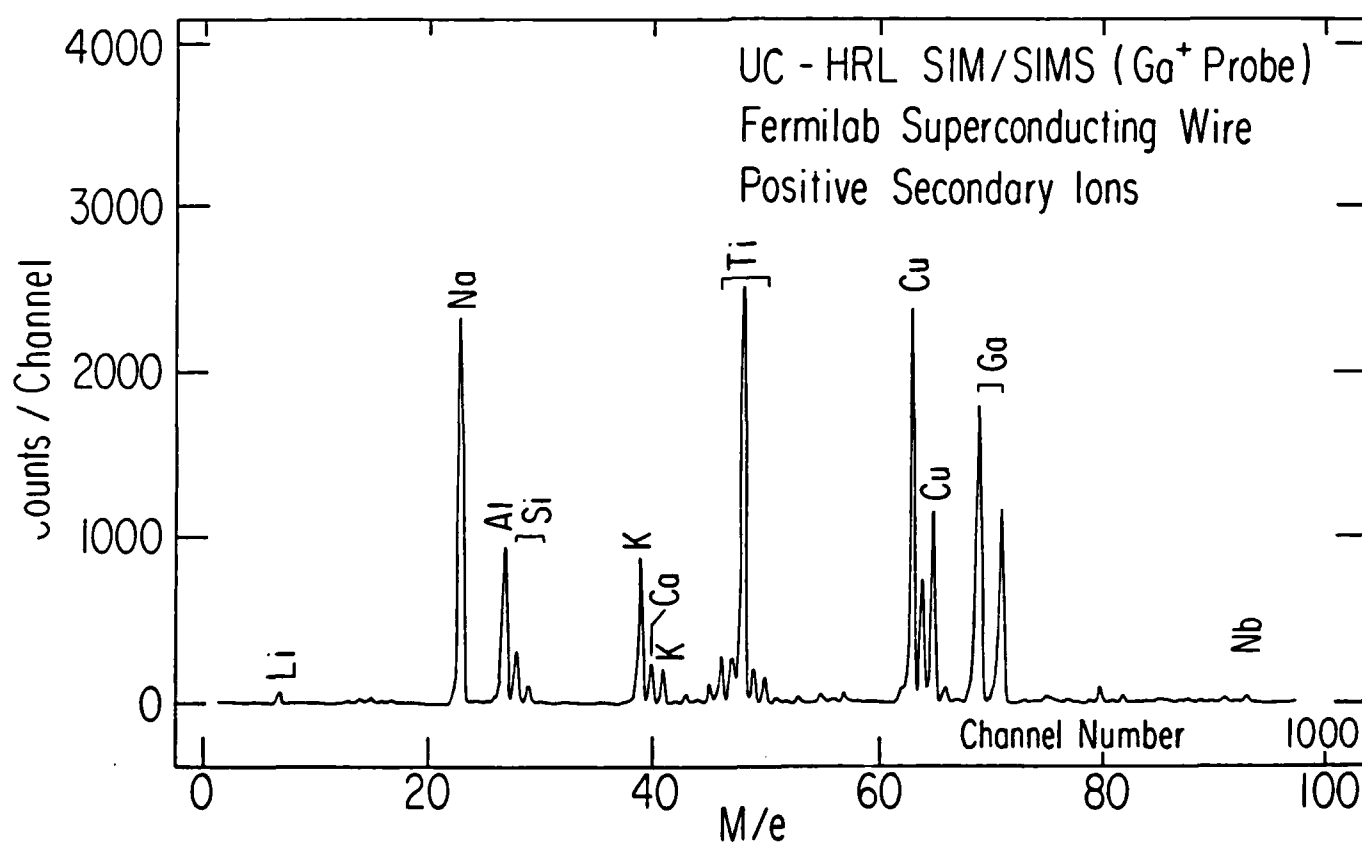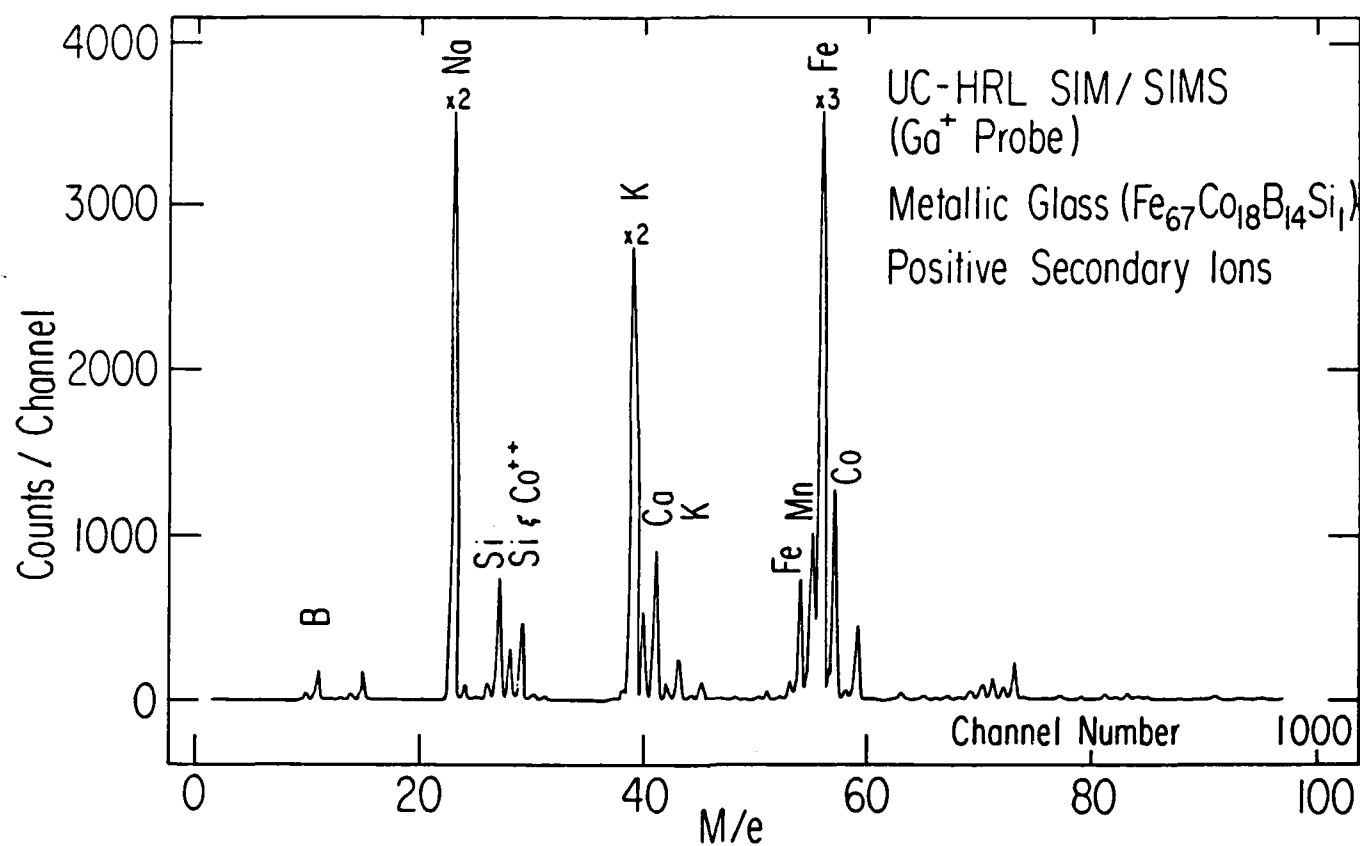
Fig. A4-17 Mass spectrum of (a) metallic glass, (b) superconducting wire.
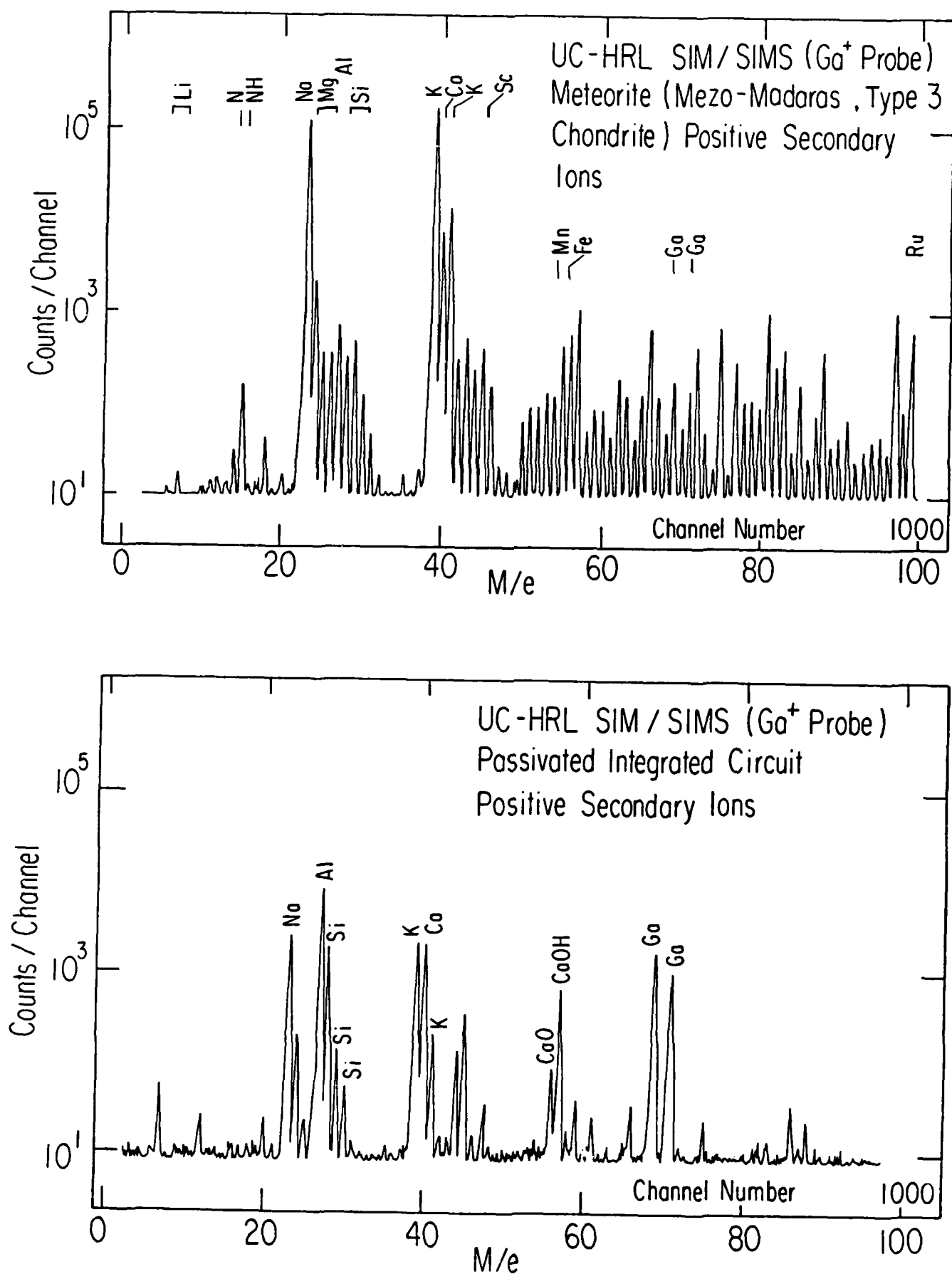
Fig. A4-18 Mass spectrum of (a) meteorite, (b) integrated circuit.

SPECTRUM OF A GaAs SUBSTRATE TAKEN BY FIB-SIMS

14316 1
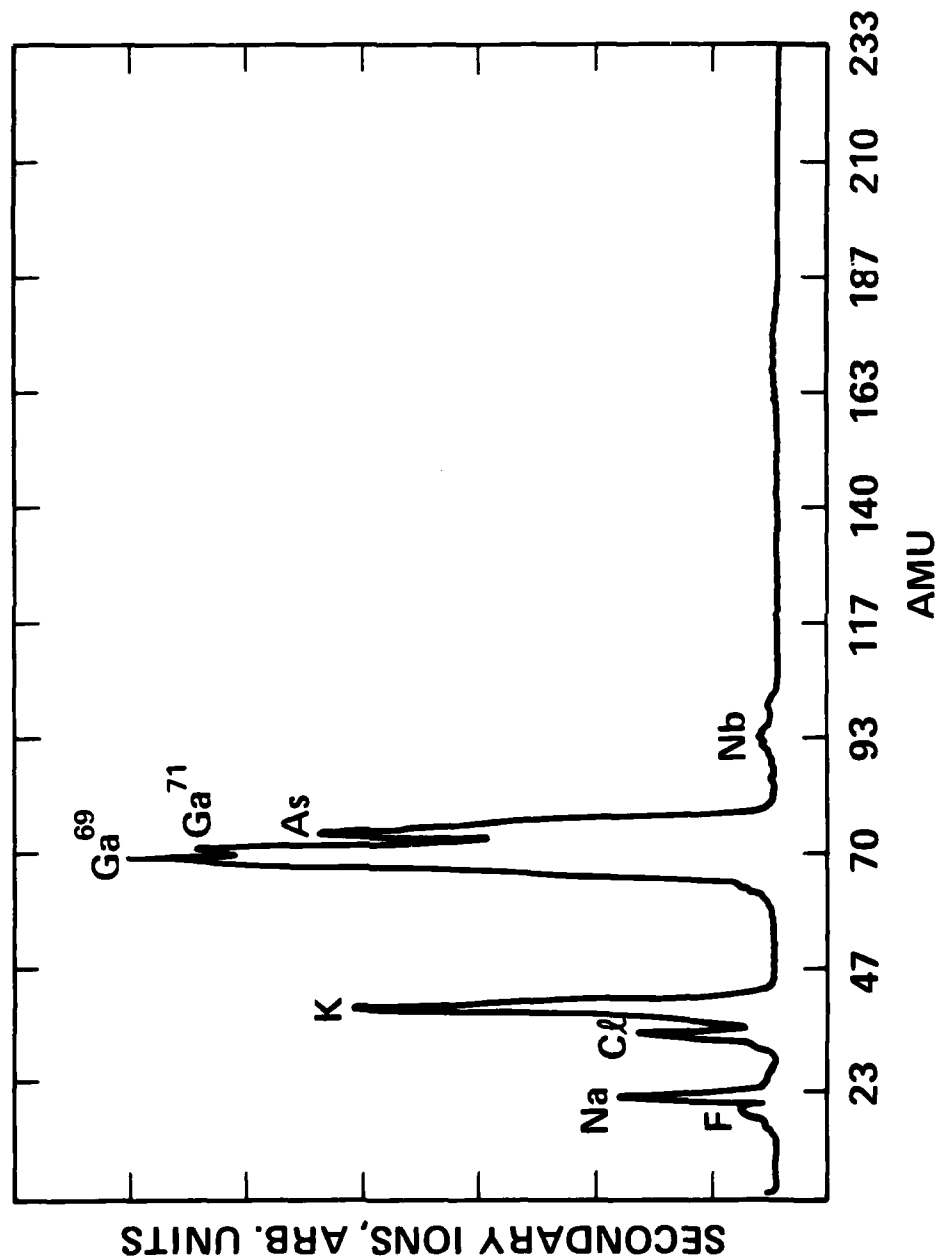
AUGUST 1984

FIG. A4-19

D. SIMS IMAGING PERFORMANCE OF

UC-HRL SIM:

ELEMENTAL MAPS AT

HIGH SPATIAL RESOLUTION

Ga$^+$ FOCUSED-ION-BEAM IMAGES
LITHIUM CONTAMINATION ON Au-COATED Si
SIMS ELEMENTAL MAPS AT HIGH SPATIAL RESOLUTION
UC-HRL SIM (39 keV Ga$^+$ IONS)
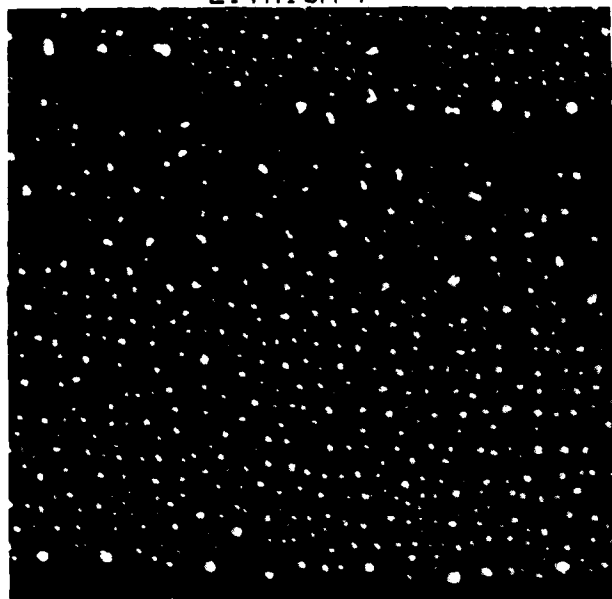
LITHIUM 7+   IMPLANTED GALLIUM 69+
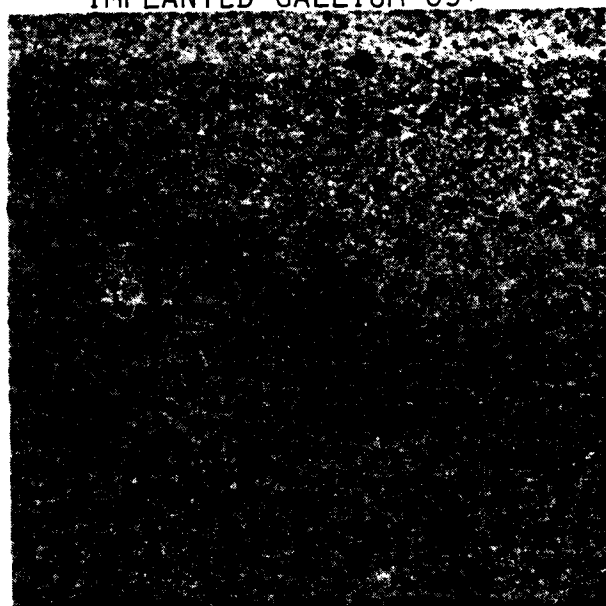
46 μM FULL SCALE
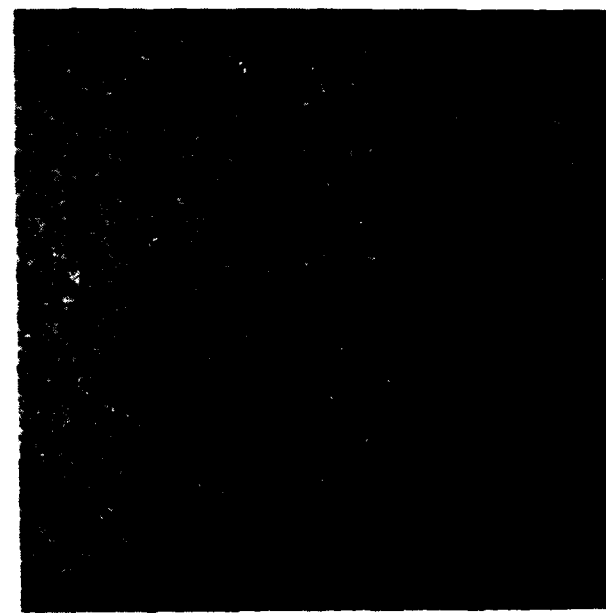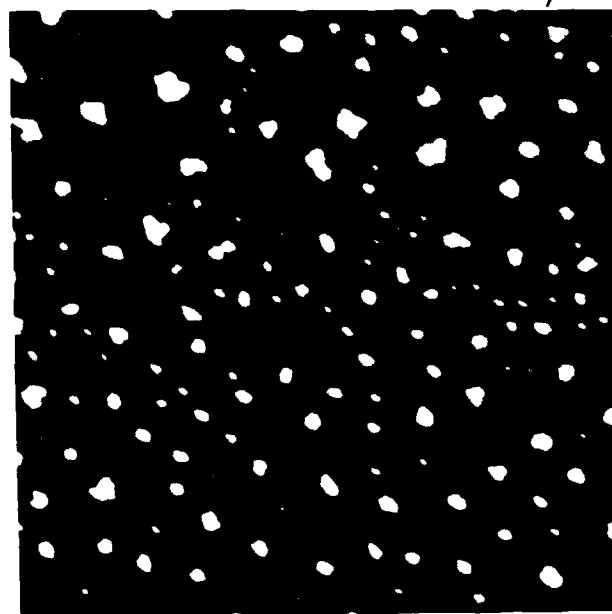
23 μM FULL SCALE

Ga$^+$ FOCUSED-ION-BEAM IMAGES
FERMILAB SUPERCONDUCTING WIRE, POLISHED SECTION
SIMS ELEMENTAL MAPS
UC-HRL SIM (40 keV Ga$^+$ IONS)

TOTAL ISI

COPPER 63+
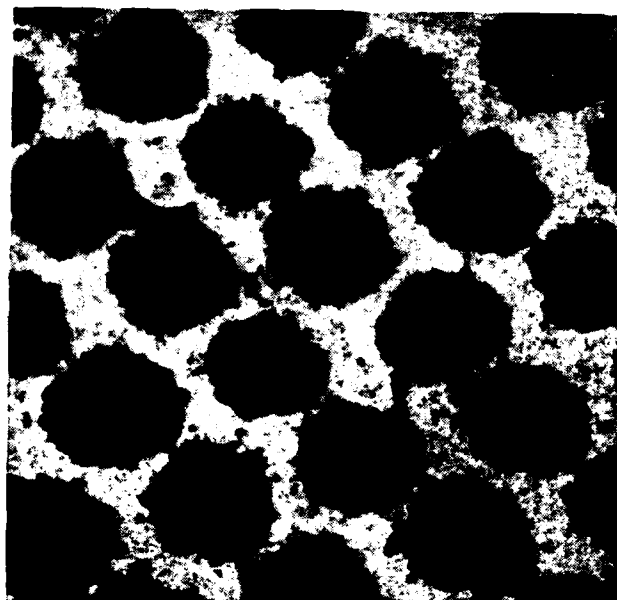
50 μM FULL SCALE
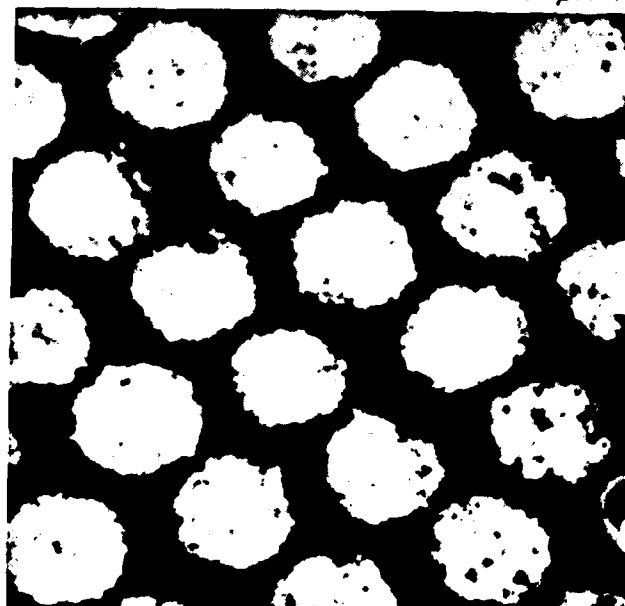
TITANIUM 48+
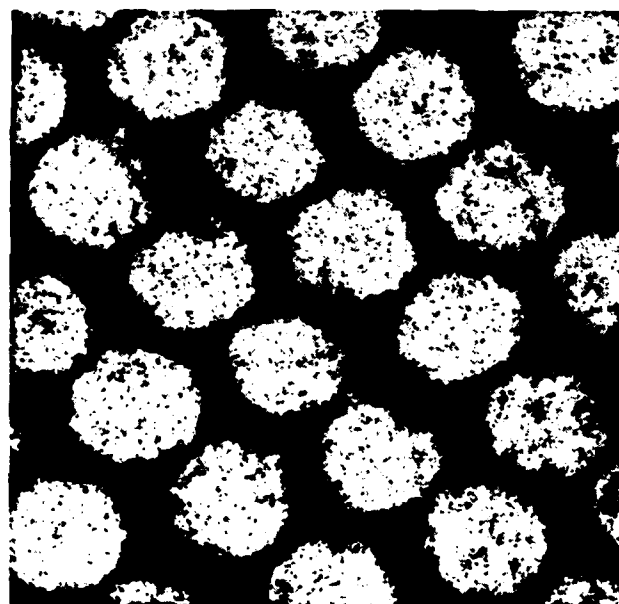
NIOBIUM 93+

Ga$^+$ FOCUSED-ION-BEAM IMAGES
SIMS ELEMENTAL MAPS OF A ROUGH Be-Cu SURFACE
UC-HRL SIM (39 keV Ga$^+$ IONS)

TOTAL SIMS   COPPER 63 +
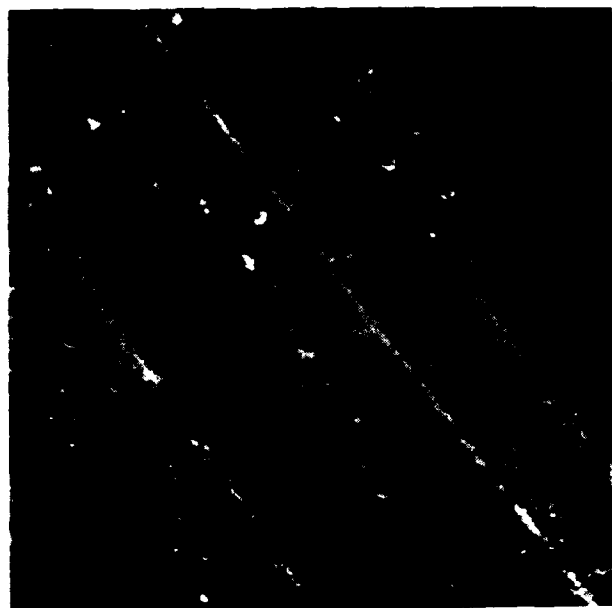
100 μM FULL SCALE

BERILLIUM 9 +   SODIUM 23 +

Ga$^+$ FOCUSED-ION-BEAM IMAGES
PASSIVATED INTEGRATED CIRCUIT, Au-COATED
ELEMENTAL MAPS BY SIMS
UC-HRL SIM (40 keV Ga$^+$ IONS)
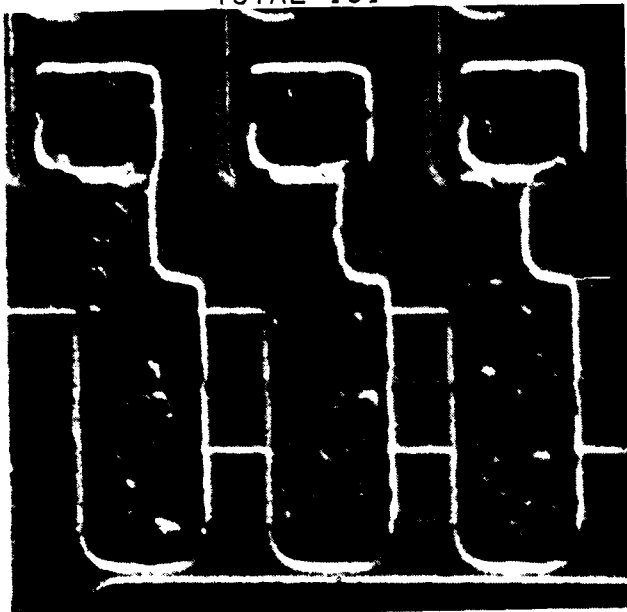
TOTAL ISI

ALUMINUM 27+
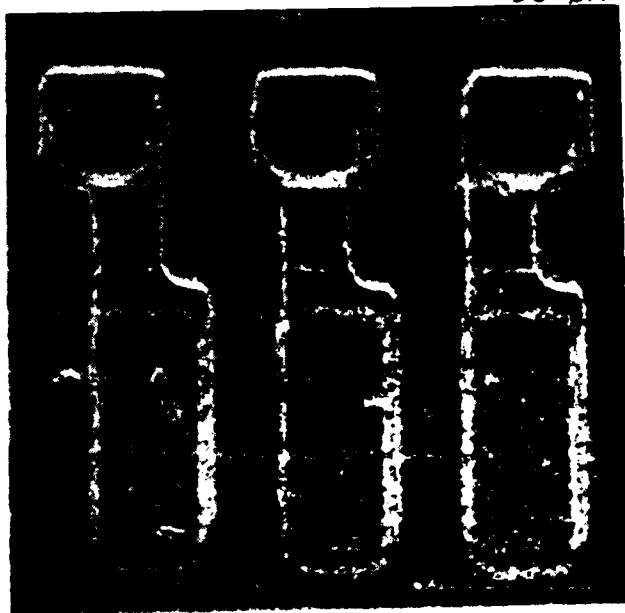
50 UM FULL SCALE

CALCIUM 40+
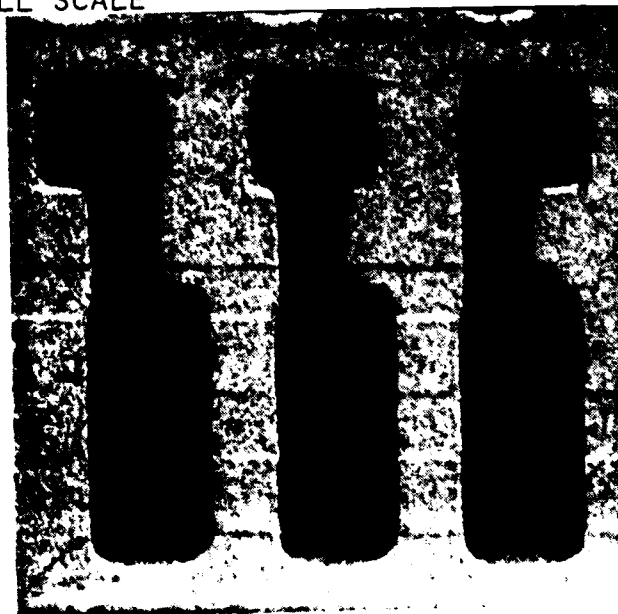
SILICON 28 +

Ga⁺ FOCUSED-ION-BEAM IMAGES
PASSIVATED INTEGRATED CIRCUIT, Au-COATED
ELEMENTAL MAPS BY SIMS
UC-HRL SIM (40 keV Ga⁺ IONS)
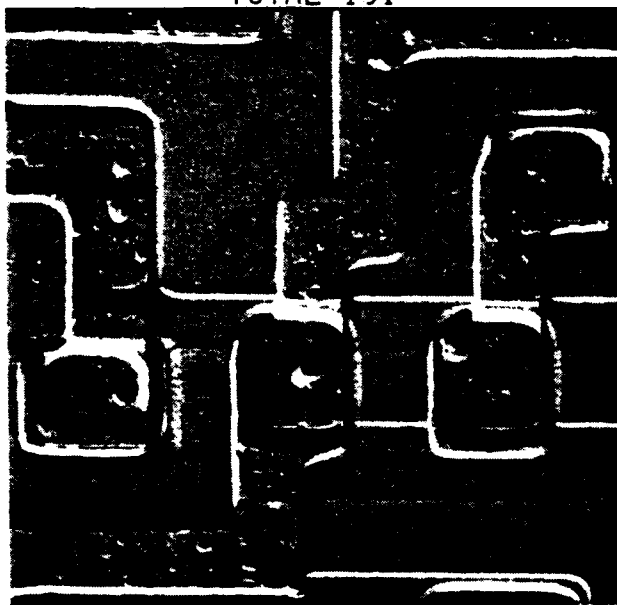
TOTAL ISI
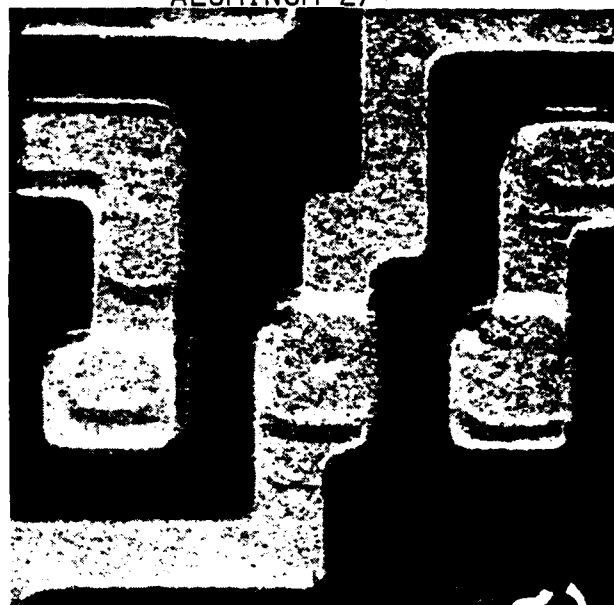
ALUMINUM 27+

50 µM FULL SCALE

SILICON 28+
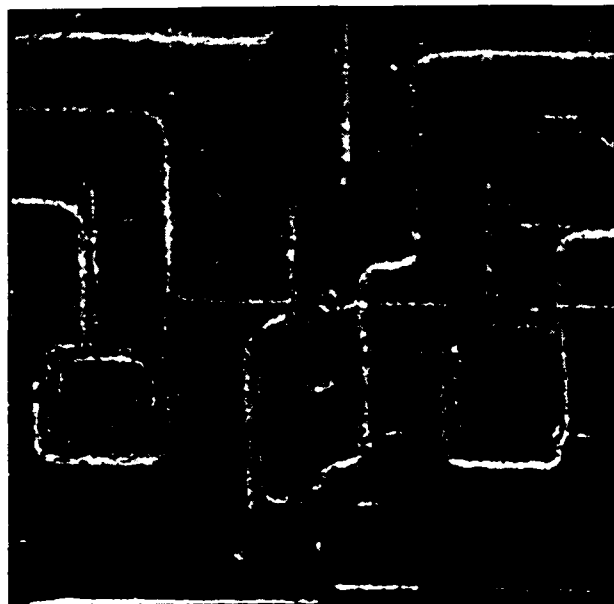
CALCIUM 40+

Ga$^+$ FOCUSED-ION-BEAM IMAGES
PASSIVATED INTEGRATED CIRCUIT, Au-COATED
ELEMENTAL MAPS BY SIMS
UC-HRL SIM (40 keV Ga$^+$ IONS)

TOTAL ISI ALUMINUM 27+
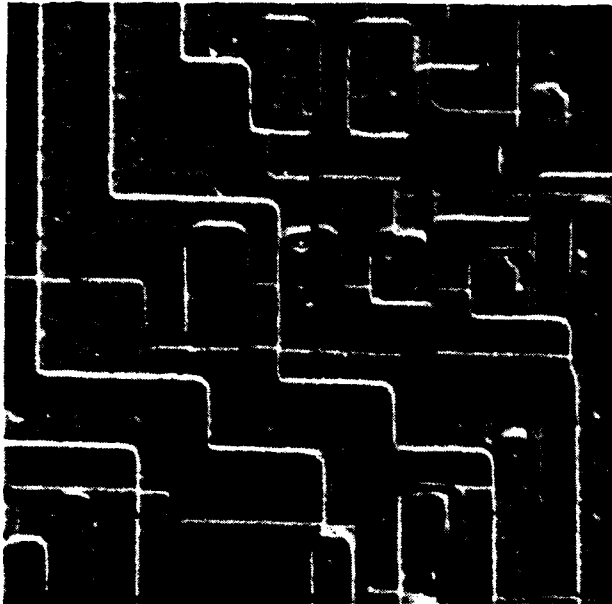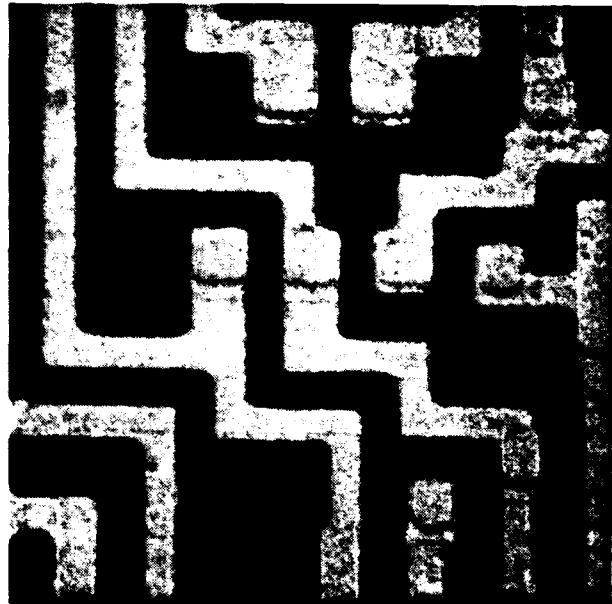
100 μM FULL SCALE
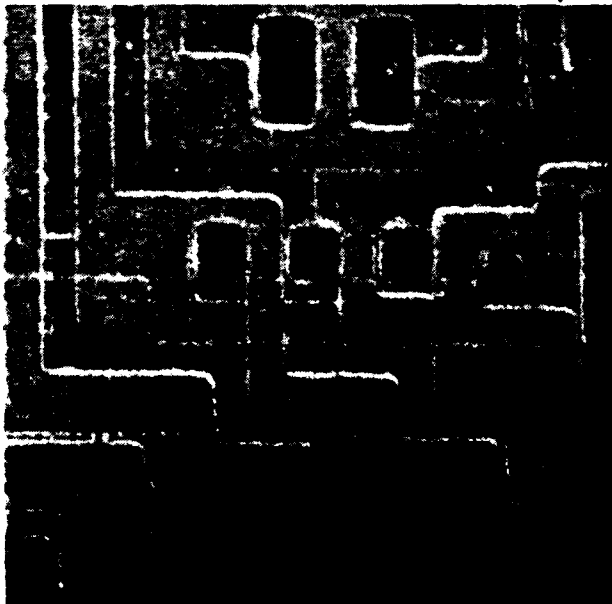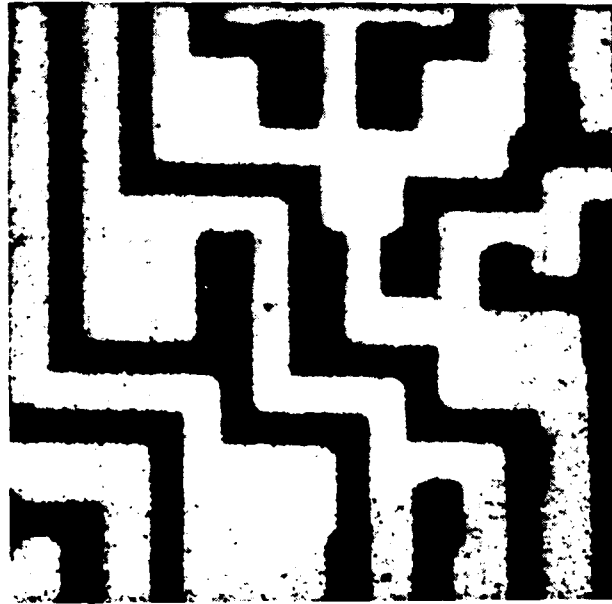
SODIUM 23+ SILICON 28+

APPENDIX 5

EXPLORATORY RESEARCH APPLICATIONS

Ga$^+$ FOCUSED-ION-BEAM IMAGES
SIMS ELEMENTAL MAPS OF FET IN GaAs
UC-HRL SIM (39 keV Ga$^+$ IONS)

TOTAL ISI   SILICON 28+

100 μM FULL SCALE

GALLIUM 69+   CHROMIUM 52+
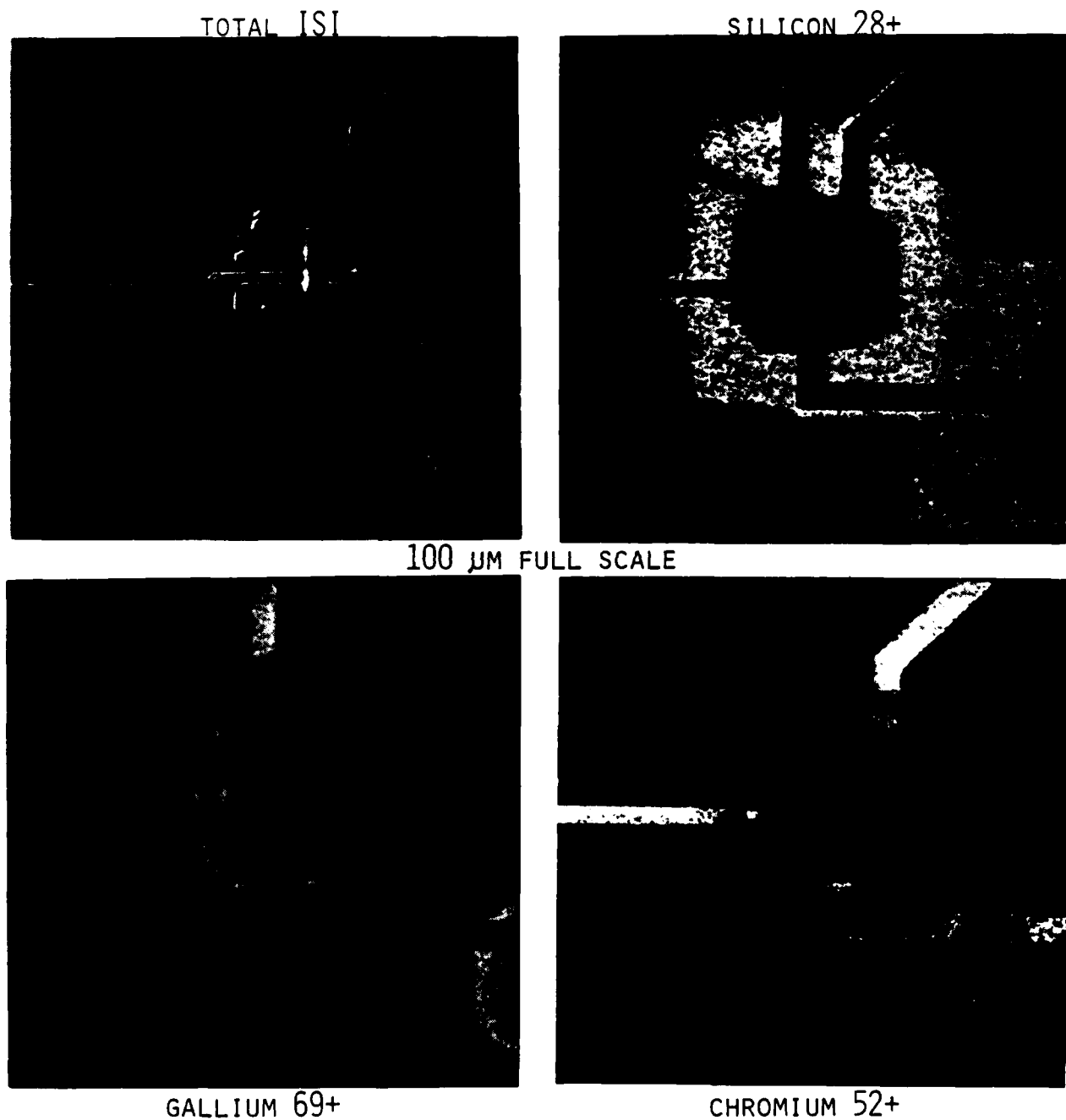
Ga⁺ FOCUSED-ION-BEAM IMAGES
SIMS ELEMENTAL MAPS OF FET STRUCTURES IN GaAs
UC-HRL SIM (39 KEV Ga⁺IONS)

TOTAL ISI

TITANIUM 48+

50 µM FULL SCALE

TOTAL ISI
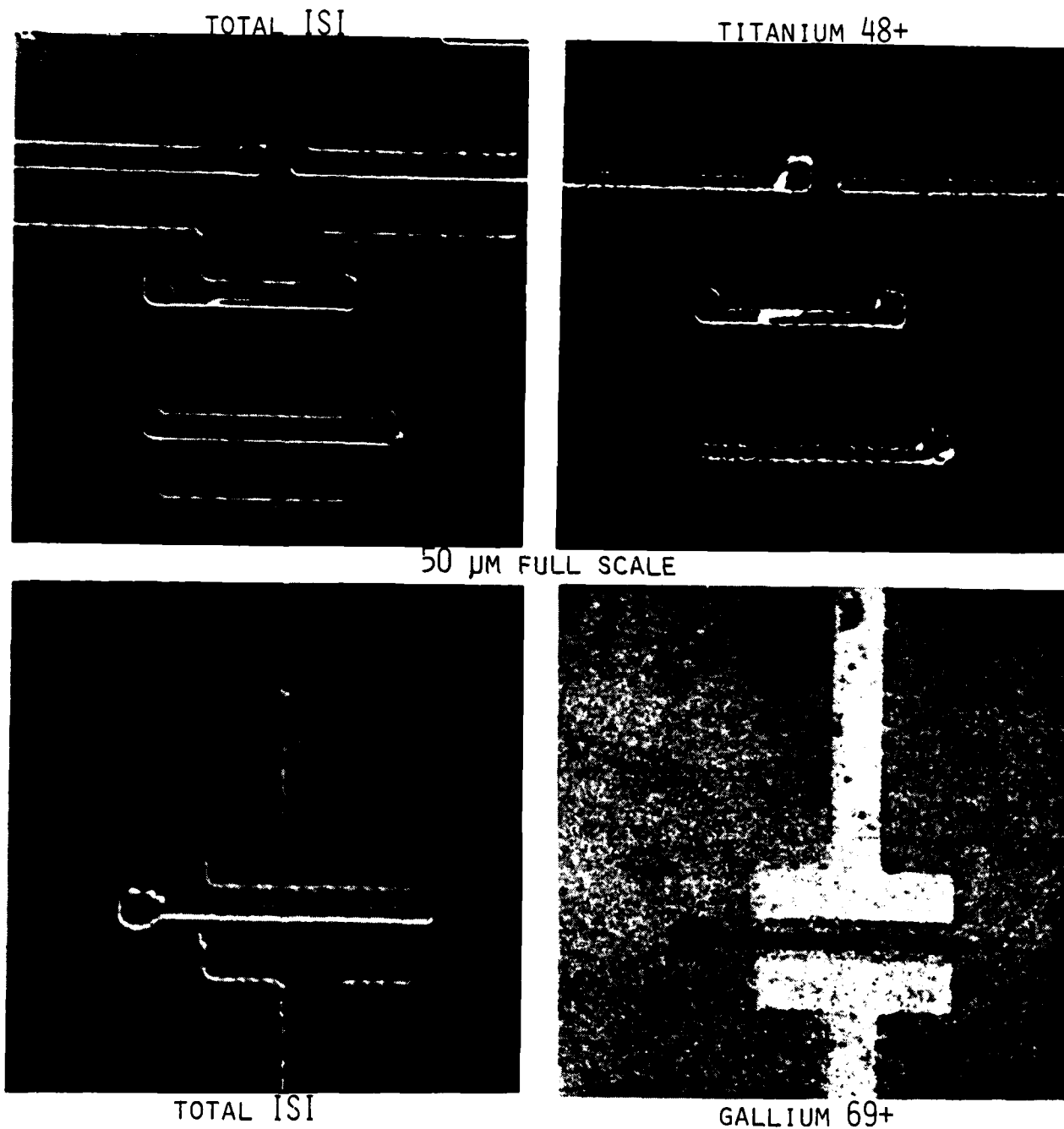
GALLIUM 69+

Ga$^+$ FOCUSED-ION-BEAM IMAGES
SIMS ELEMENTAL MAPS OF FET STRUCTURES IN GaAs
AFTER EROSION BY ION BOMBARDMENT (DOSE 1x10^{17} IONS/CM^2)
UC-HRL SIM (39 keV Ga$^+$ IONS)

TOTAL ISI
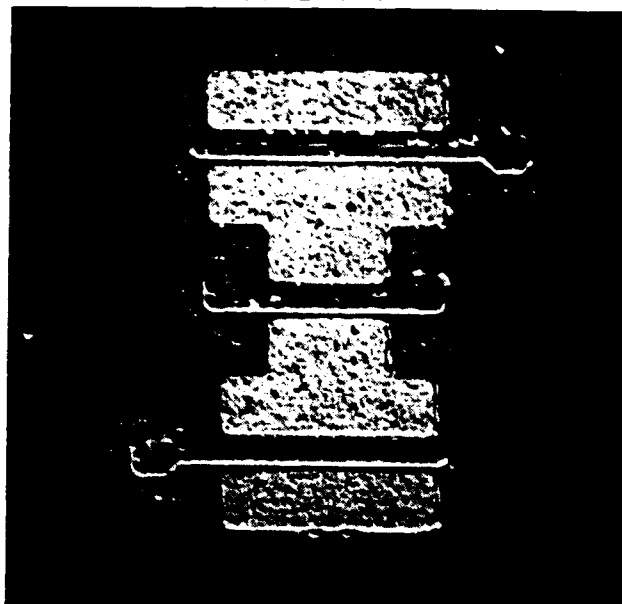
TITANIUM 48+
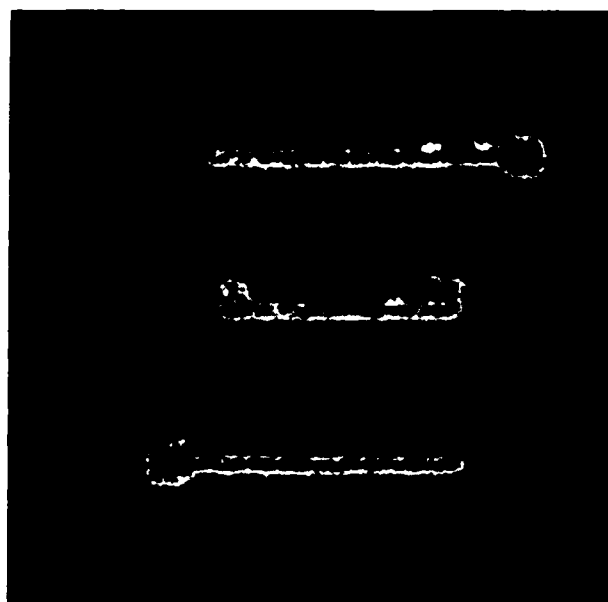
50 μM FULL SCALE
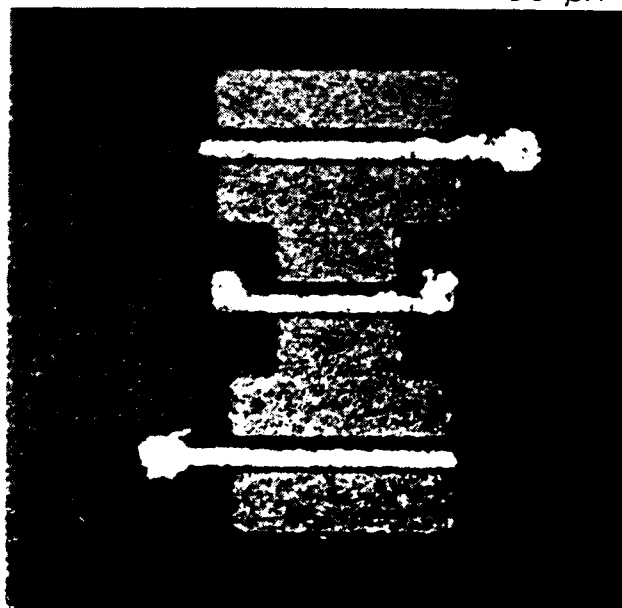
GALLIUM 69+

MOLECULAR GALLIUM 138+
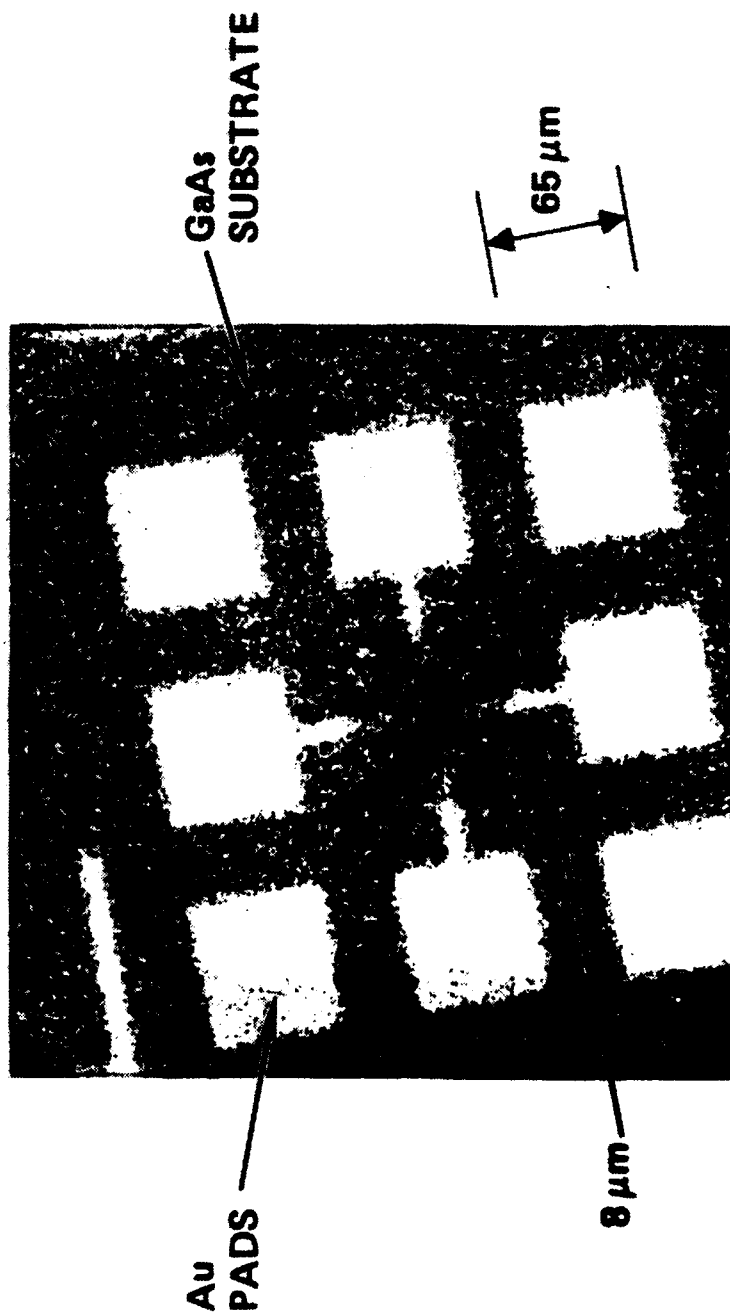
FIG. A5-4

HUGHES

FIB-SIMS MICRO-PHOTOGRAPHS

14316-2

AUGUST 1984

Na ION IMAGE OF Au PADS ON GaAs. 160 μm F.S.
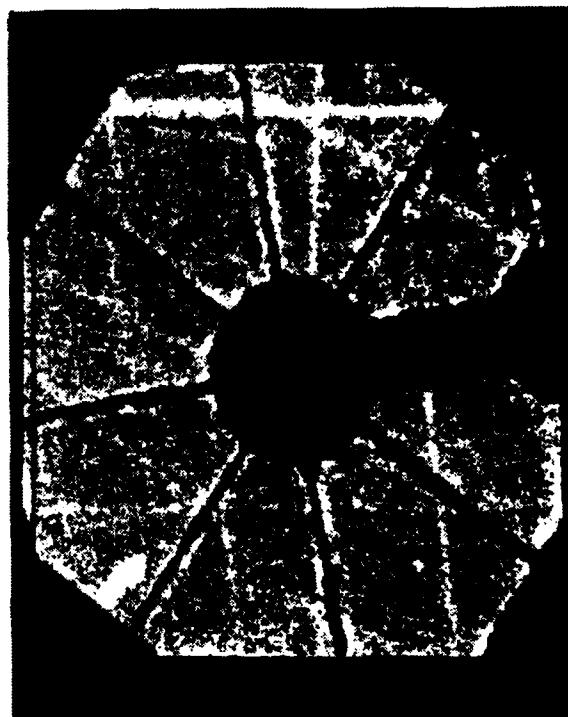
Ga ION IMAGE OF Au PADS ON GaAs. 160 μm F.S.

FIG. A5-5

Ga$^+$ FOCUSED-ION-BEAM IMAGES
CHONDRULE RIM IN MEZO MADARAS METEORITE (Au-COATED SECTION)
SIMS ELEMENTAL MAPS AT HIGH SPATIAL RESOLUTION
UC-HRL SIM (40 keV Ga$^+$ IONS)

SODIUM 23+

MAGNESIUM 24+

50 µM FULL SCALE

POTASSIUM 39+

IRON 56+

Ga$^+$ FOCUSED-ION-BEAM IMAGES
MEZO-MADARAS METEORITE (AU-COATED SECTION)
SIMS ELEMENTAL MAPS AT HIGH SPATIAL RESOLUTION
UC-HRL SIM (40 KEV GA$^+$IONS)

SODIUM 23+   MAGNESIUM 24+

45 UM FULL SCALE
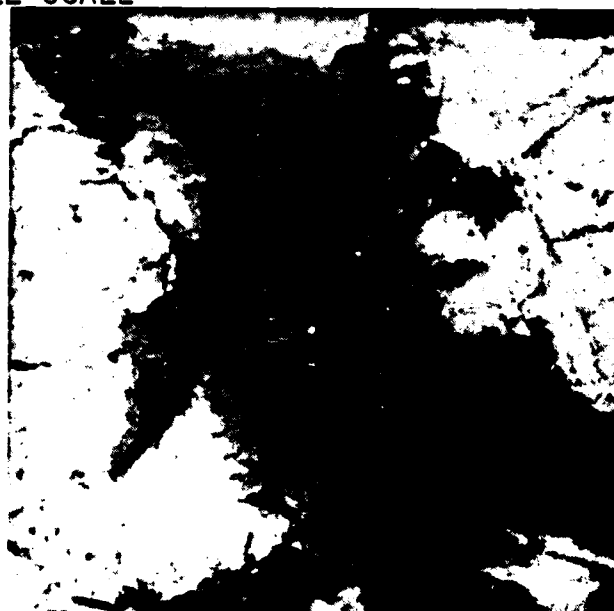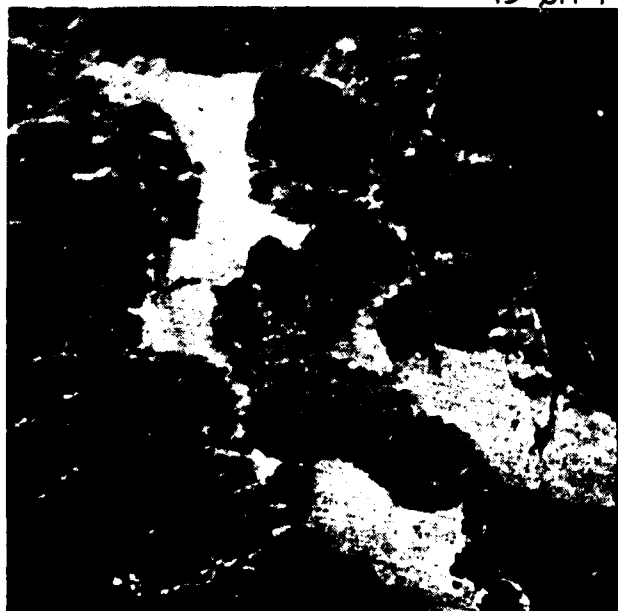
Ga$^+$ FOCUSED-ION-BEAM IMAGES
ALLENDE METEORITE, Au-COATED SECTION
SIMS ELEMENTAL MAPS AT HIGH SPATIAL RESOLUTION
UC-HRL SIM (40 keV Ga+ IONS)

SODIUM 23+

ALUMINUM 27+
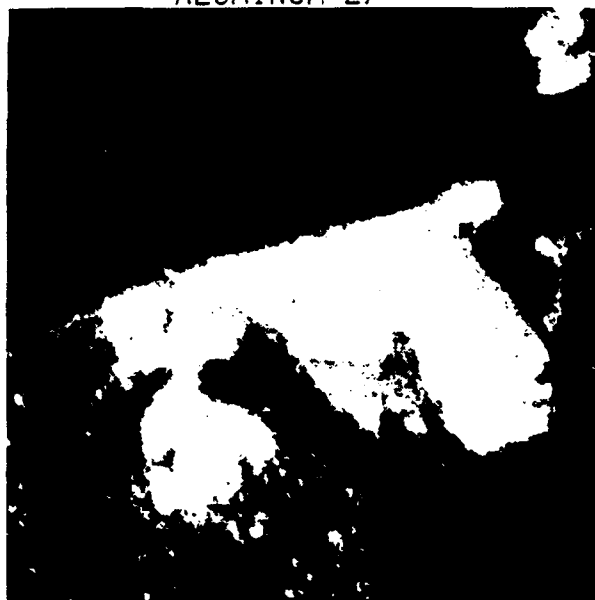
25 µM FULL SCALE

MAGNESIUM 24+
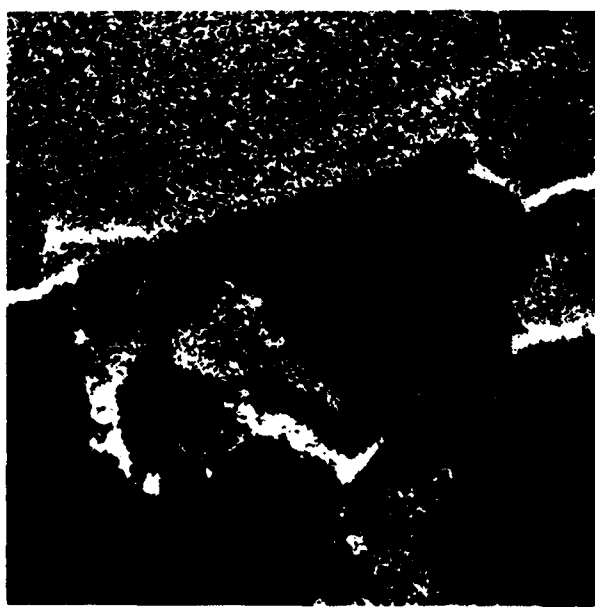
MAGNESIUM 25+

GA$^+$ FOCUSED-ION-BEAM IMAGES
SBCL$_5$ STAGE-2 INTERCALATED GRAPHITE
MULTIDOMAIN STRUCTURES, SECONDARY ELECTRON IMAGES
UC-HRL SIM (40 KEV GA$^+$ IMAGES)
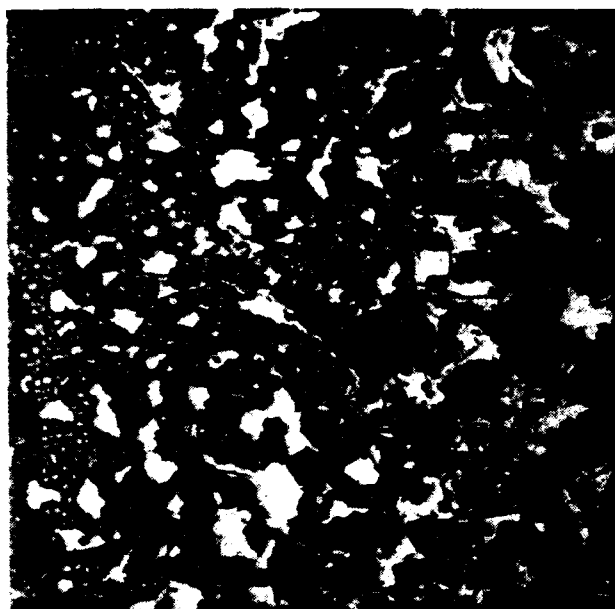
262 µM FULL SCALE
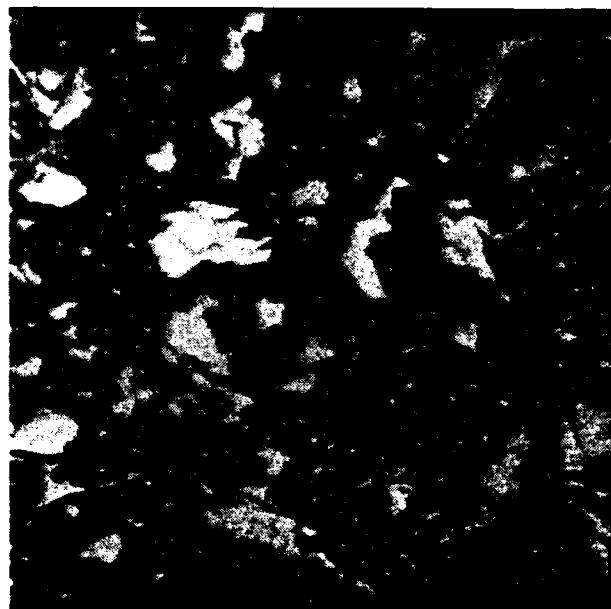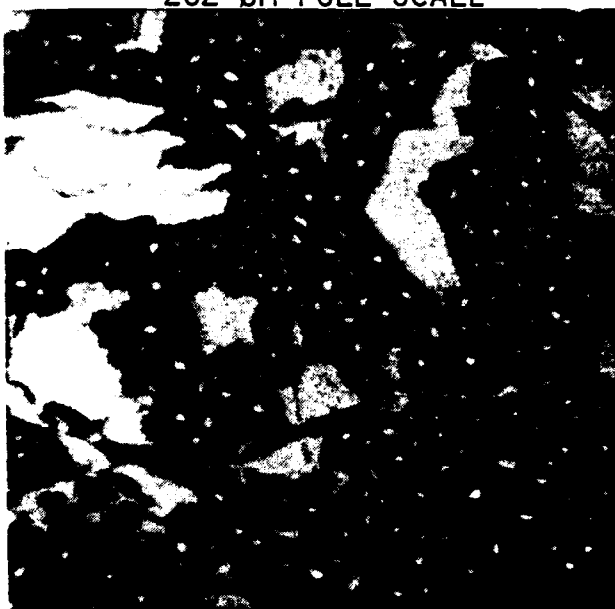
131 µM FULL SCALE
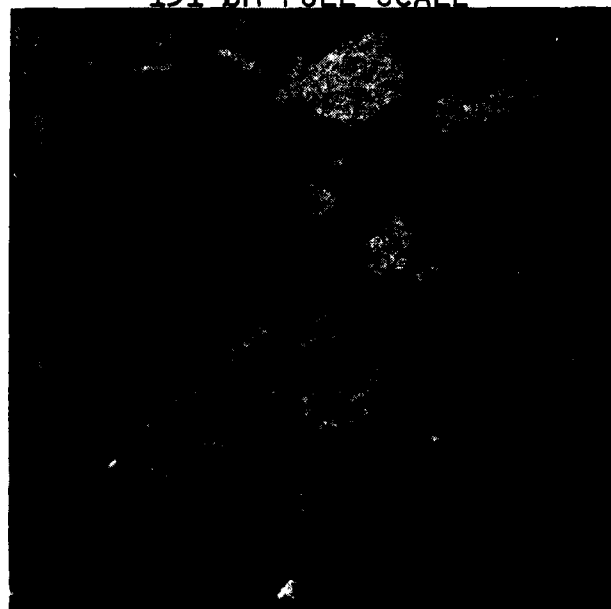
65 µM FULL SCALE

131 µM FULL SCALE

Ga$^+$ FOCUSED-ION-BEAM IMAGES
SbCl$_5$ INTERCALATED PYROLITHIC GRAPHITE
DOMAIN STRUCTURES, SECONDARY ELECTRON IMAGES
UC-HRL SIM (40 keV Ga$^+$ IONS)

STAGE 4
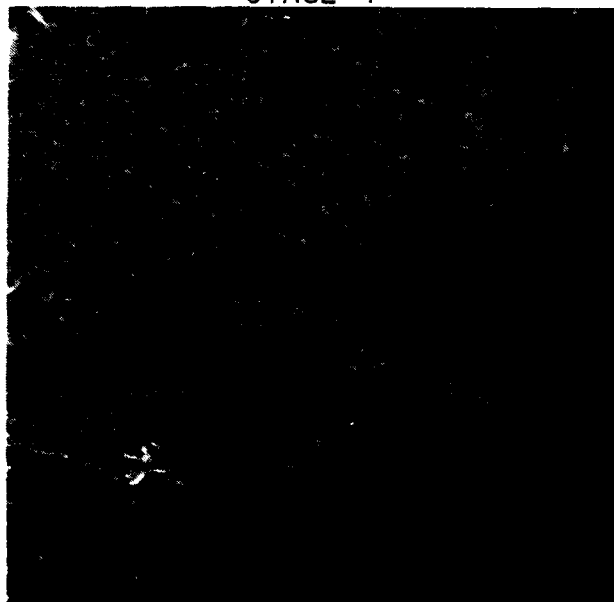
STAGE 2
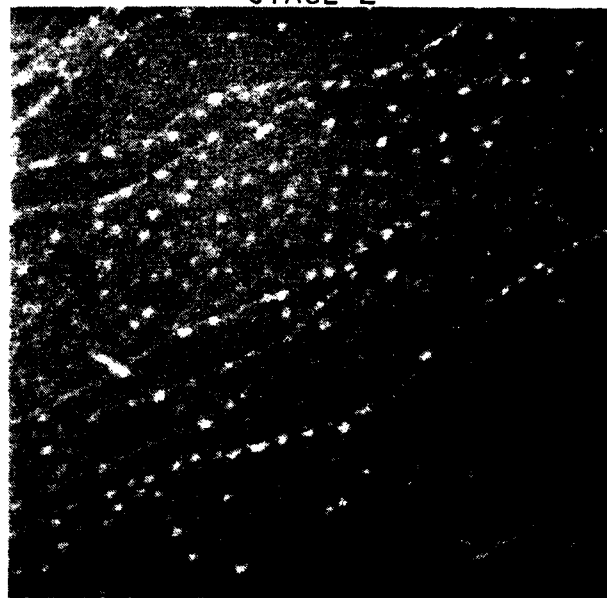
24 μM FULL SCALE
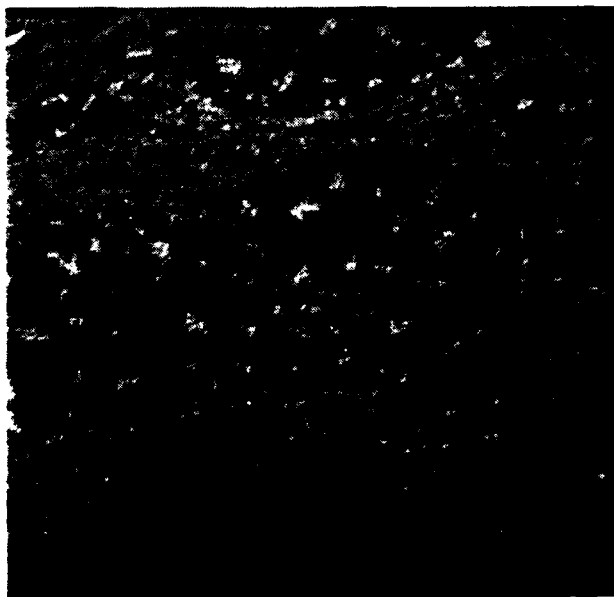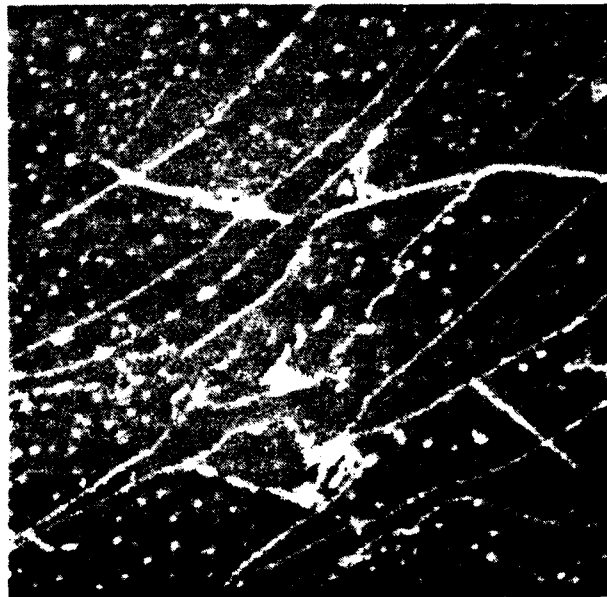
12 μM F.S.

12 μM F.S.

12 μM F.S.

GA$^+$ FOCUSED-ION-BEAM IMAGES
ISE IMAGES OF STRUCTURES IN HIGHLY ORIENTED PYROLITHIC GRAPHITE
UC-HRL SIM (40 KEV GA$^+$ IONS)

50 μM FULL SCALE

25 μM FULL SCALE

Ga$^+$ FOCUSED-ION-BEAM IMAGES
HUMAN KIDNEY STONE, UNPOLISHED FRACTURE, Au-COATED
CRYSTALLOGRAPHIC CONTRAST AND SIMS CALCIUM MAPS
UC-HRL SIM (40 keV Ga$^+$ IONS)

TOTAL ISI
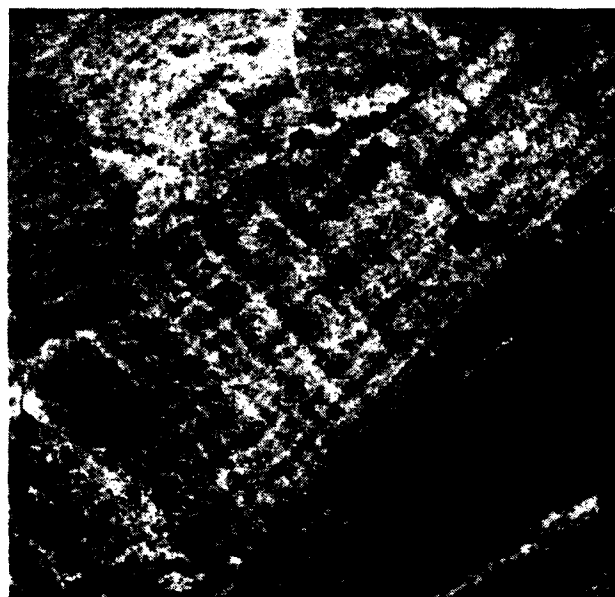
CALCIUM 40+

50 UM FULL SCALE
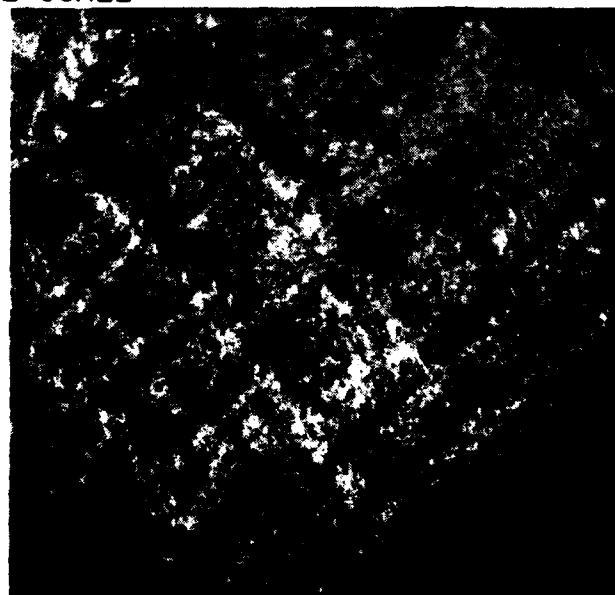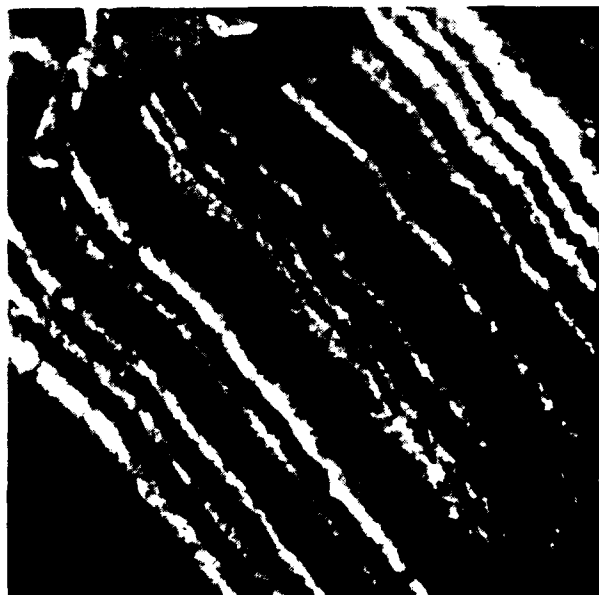
25 UM FULL SCALE

Ga⁺ FOCUSED-ION-BEAM IMAGES
HUMAN KIDNEY STONE, UNPOLISHED FRACTURE, Au-COATED
SECONDARY ION IMAGES AND SIMS CALCIUM MAPS
UC-HRL SIM (40 keV Ga⁺ IONS)

TOTAL ISI   CALCIUM 40+

25 UM FULL SCALE
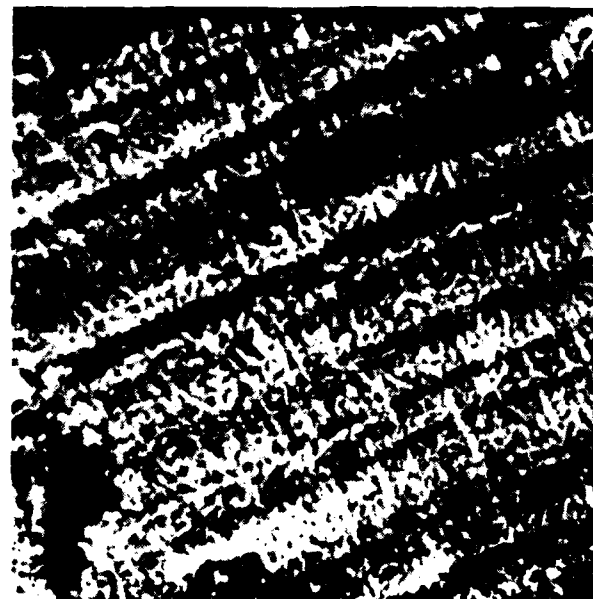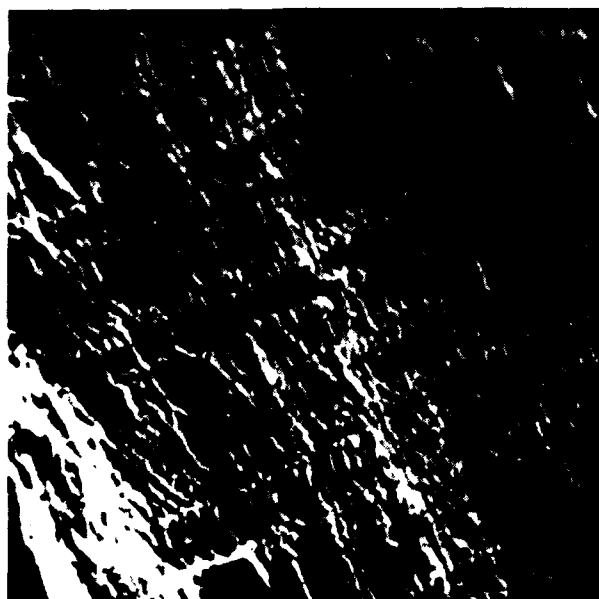
GA$^+$ FOCUSED-ION-BEAM IMAGES
SKULL BONE (CALVARIA) OF NEONATAL MOUSE
SIMS ELEMENTAL MAPS AT HIGH SPATIAL RESOLUTION
UC-HRL SIM (40 KEV GA$^+$IONS)
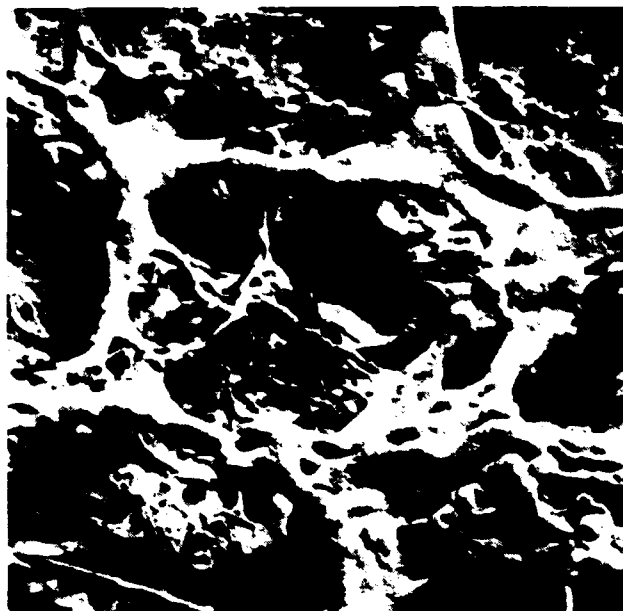
TOPOGRAPHY (ISI)   SODIUM 23+
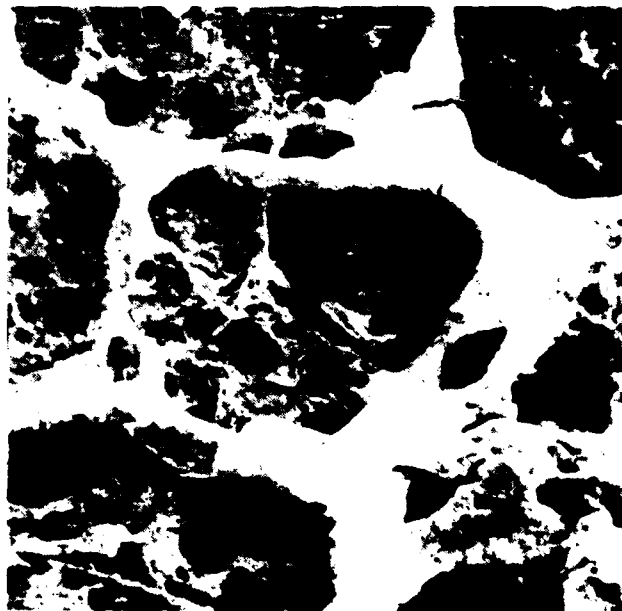
50 µM FULL SCALE
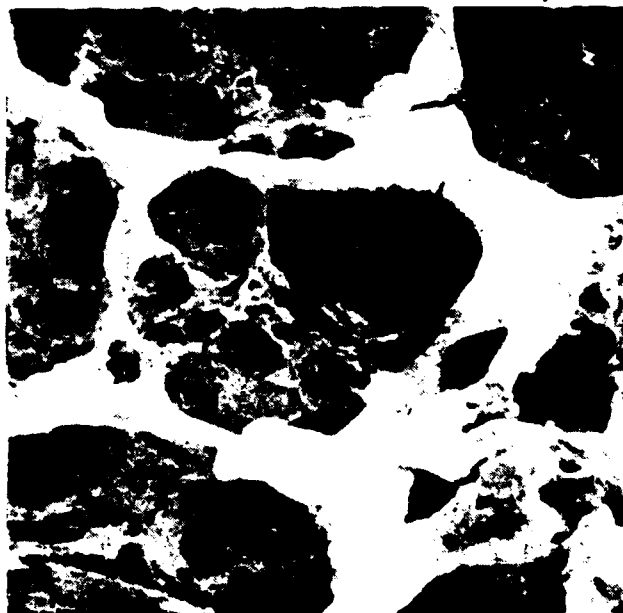
POTASSIUM 39+   CALCIUM 40+

GA+ FOCUSED-ION-BEAM IMAGES
SKULL BONE (CALVARIA) OF NEONATAL MOUSE
SIMS ELEMENTAL MAPS AT HIGH SPATIAL RESOLUTION
UC-HRL SIM (40 KEV GA+IONS)

TOPOGRAPHY (ISI)   SODIUM 23+
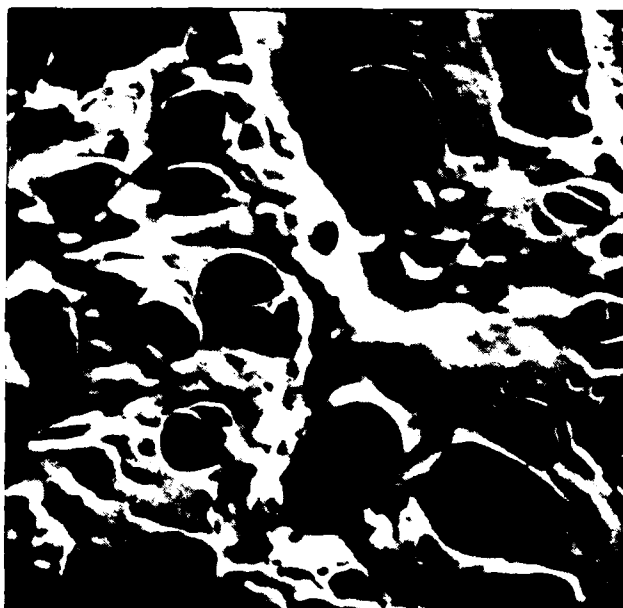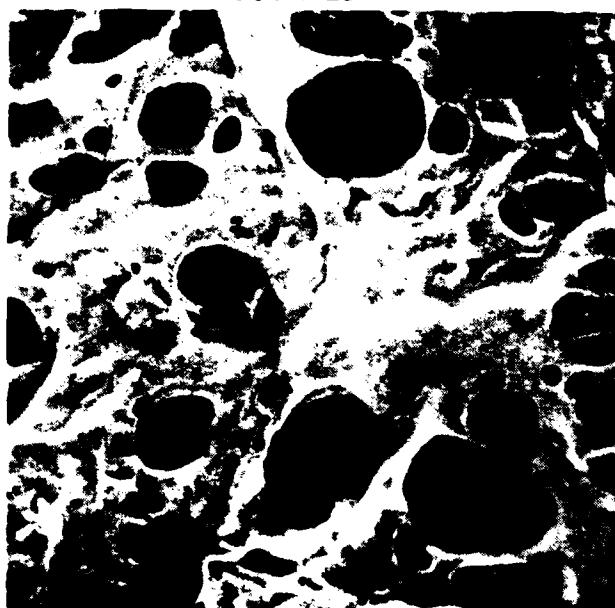
25 μM FULL SCALE
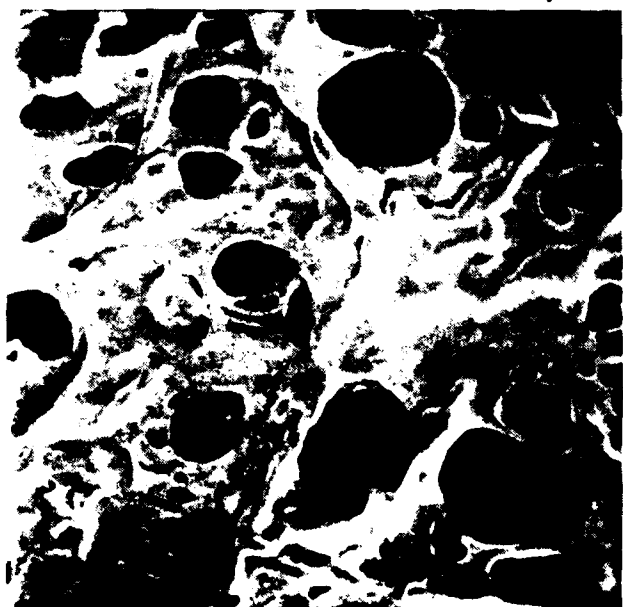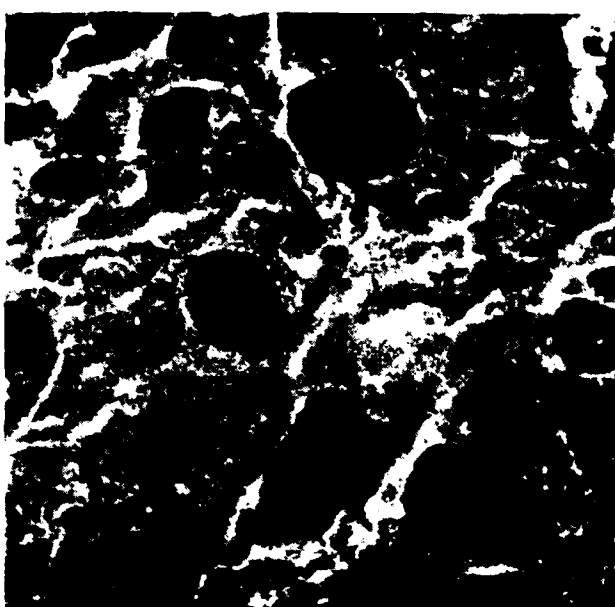
POTASSIUM 39+   CALCIUM 40+

30 Kv |—————| 1500 μm

(a)

30 Kv |—————| 750 μm

(b)
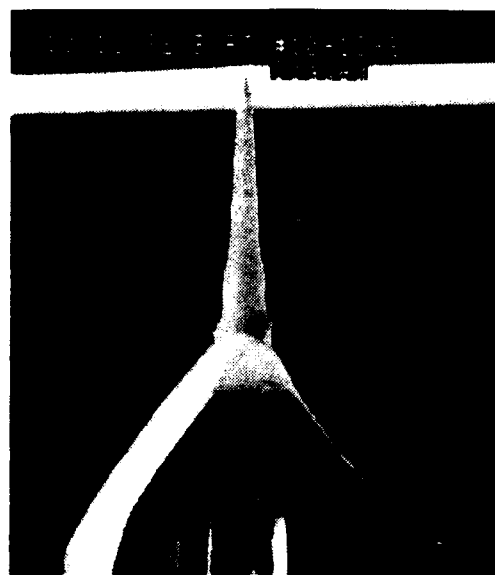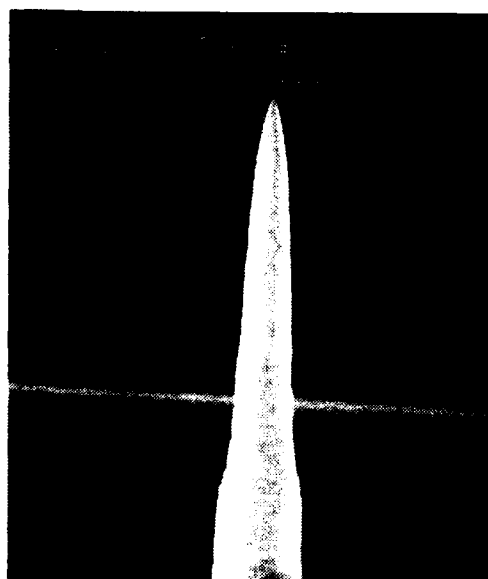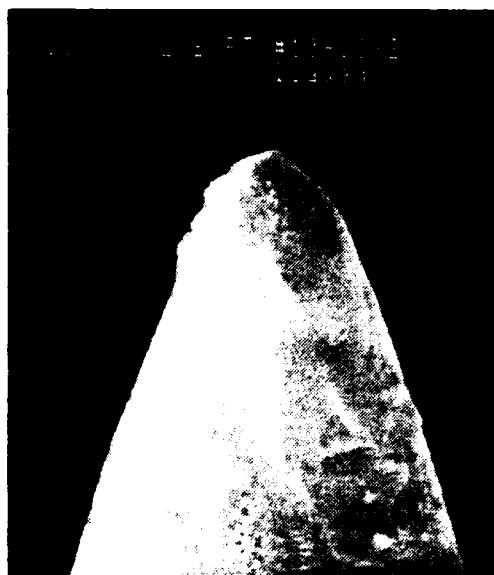
30 Kv |—————| 20.0 μm

(c)

Fig. A5-16

SEM photographs of B–Pt eutectic alloy ion source before use. Figure 4-4(a) shows the overall assembly, while Figures 4-4(b) and (c) are higher magnification views of the rhenium tip showing smoothness before use of source.
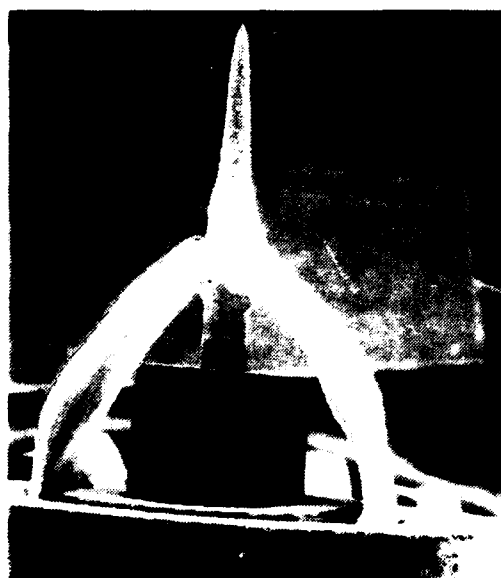
25 Kv   1500 μm

(a)
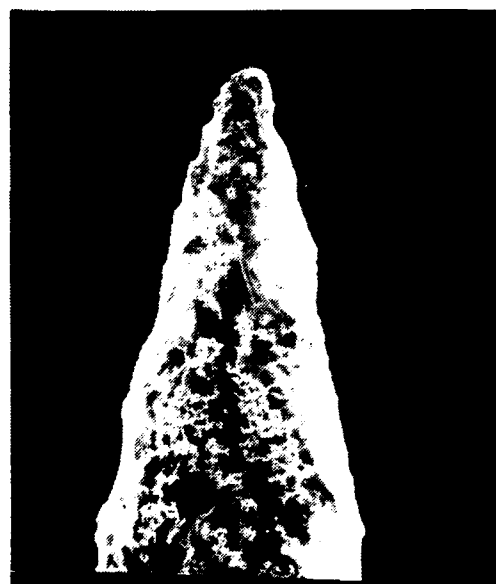
25 Kv   86 μm

(b)

25 Kv   13.6 μm

(c)

Fig. A5-17

SEM photographs of used B-Pt liquid
metal ion source. Comparison of
Figure 4-5(b) and (c) with
Figure 4-4(b) and (c) shows
heavy corrosion of tip material
during use of source.

14316-3

HUGHES

FIB-SIMS MICRO-PHOTOGRAPHS

AUGUST 1984

SECONDARY ION IMAGE
OF B-Pt SOURCE
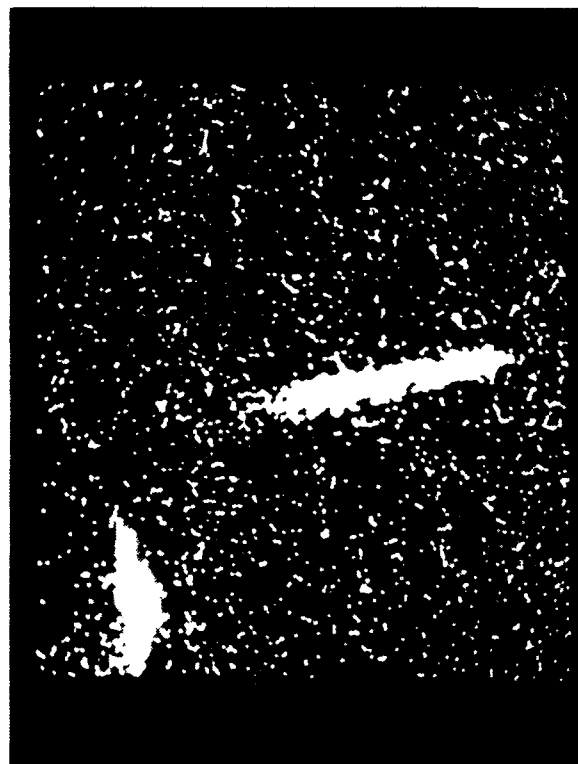
Pt ION IMAGE OF
B-Pt SOURCE
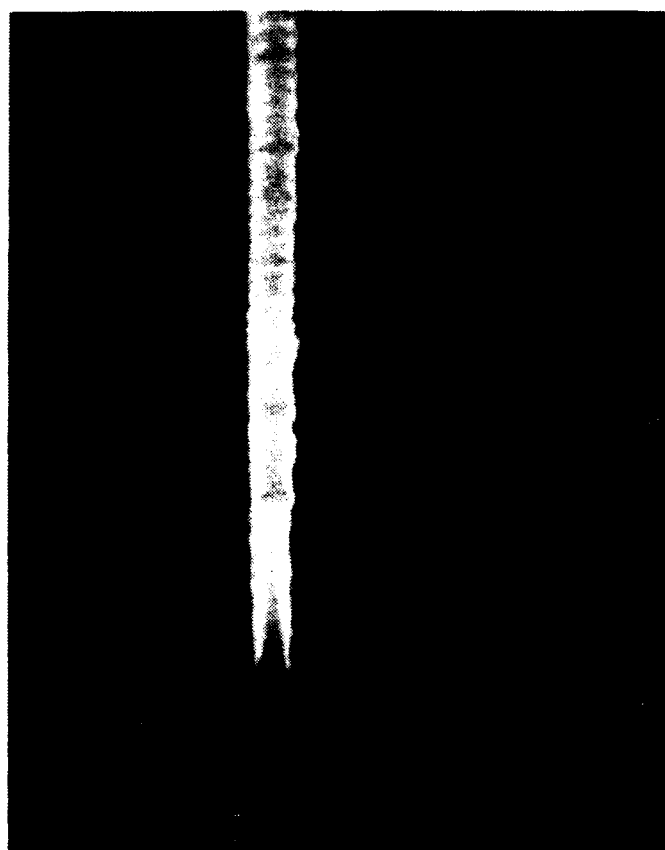
FIG. A5-18

Fig. A5-19 High aspect ratio structures fabricated by focused ion beam
(40 keV Ga$^+$) exposure (8 x 10^{12}/cm^2) of double layer resist
on Si, and subsequent reactive ion etching.

Fig. A5-20 High aspect ratio structures fabricated by focused ion beam
(40 keV Ga$^+$) exposure ($8 \times 10^{12}/cm^2$) of double layer resist
on Si, and subsequent reactive ion etching.

I—I = 1 μm

I——I = 1 μm
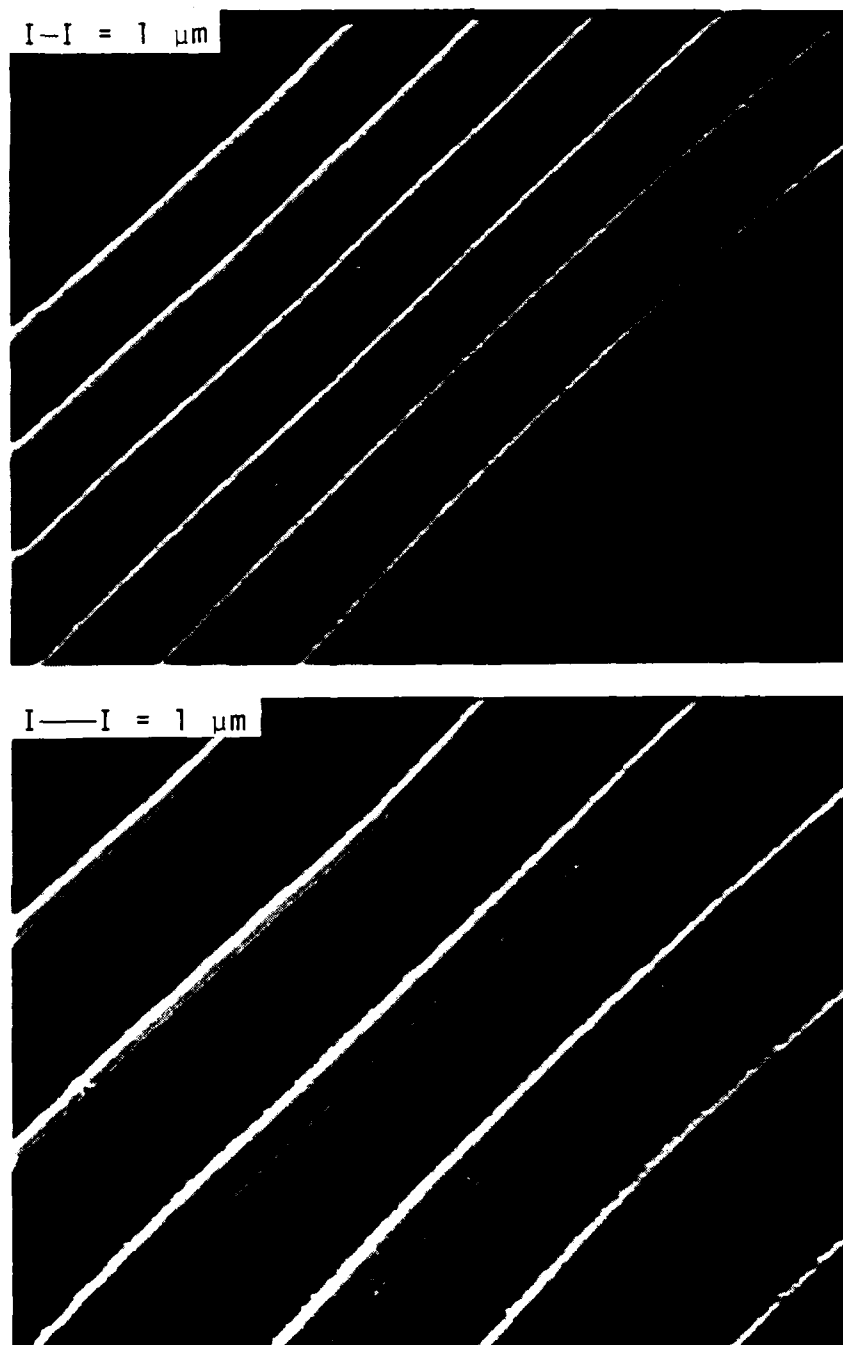
Fig. A5-21 Line patterns written at doses of (from left to right): 4.3×10^{14}, 4.3×10^{15}, 4.3×10^{16} ions/cm^2 or speeds of 400, 40, 4 μm/sec. (110) Si at 10° incidence. 14pA, 50 keV Ga$^+$ ion beam, with 500 Å spot size. This and following micrographs taken with Hitachi HFS-2 SEM.
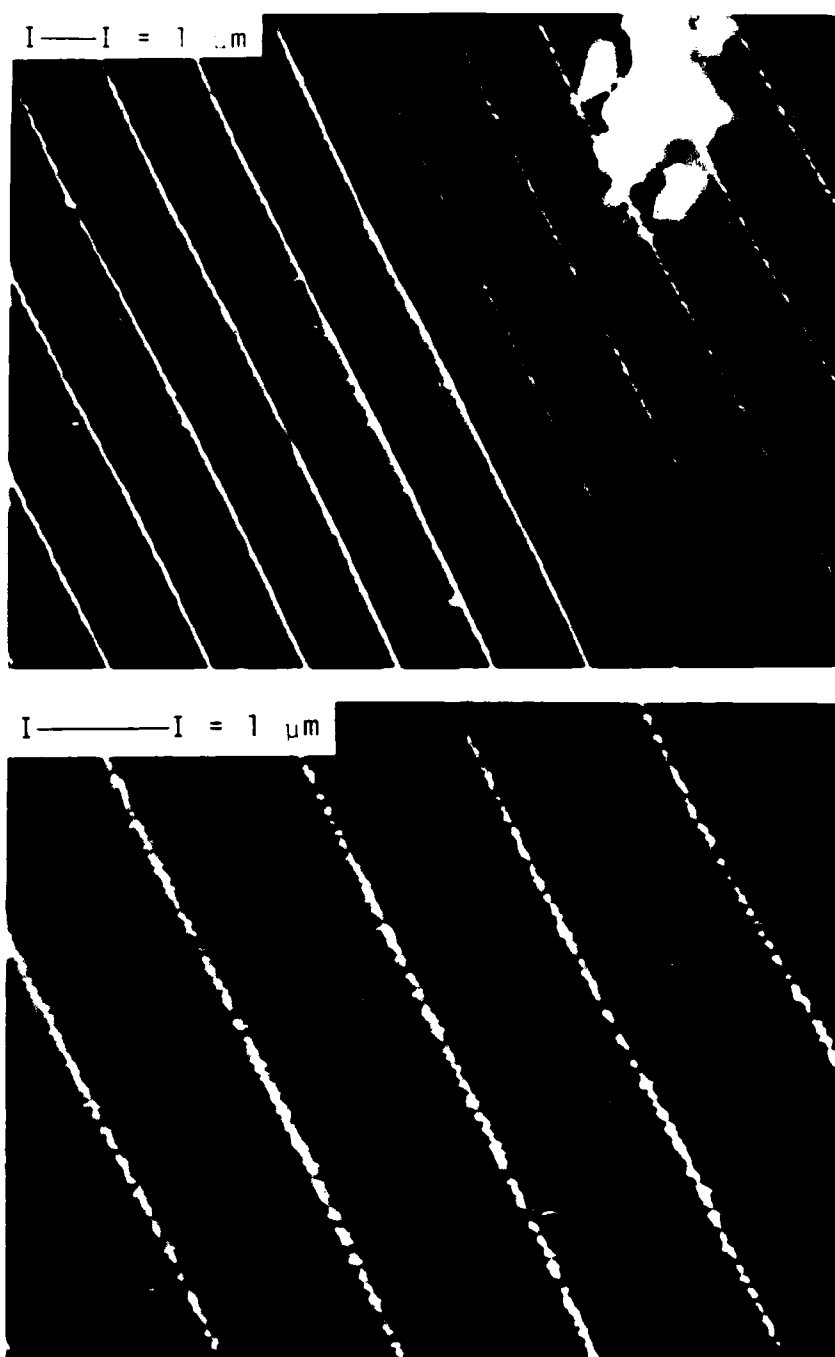
Fig. A5-22 Line patterns written at doses of 4.3×10^{14} ions/cm^2 (top left) and 2.1×10^{14} ions/cm^2 (top right and bottom). Corresponding speeds are 400 and 800 µm/sec. (110) Si at 10° incidence.

Fig. A5-23 Line patterns written at doses of 4.3 x 10^{14} ions/cm^2 (400 μm/sec). Bottom left written at twice the above dose. (110) Si at 10° incidence.
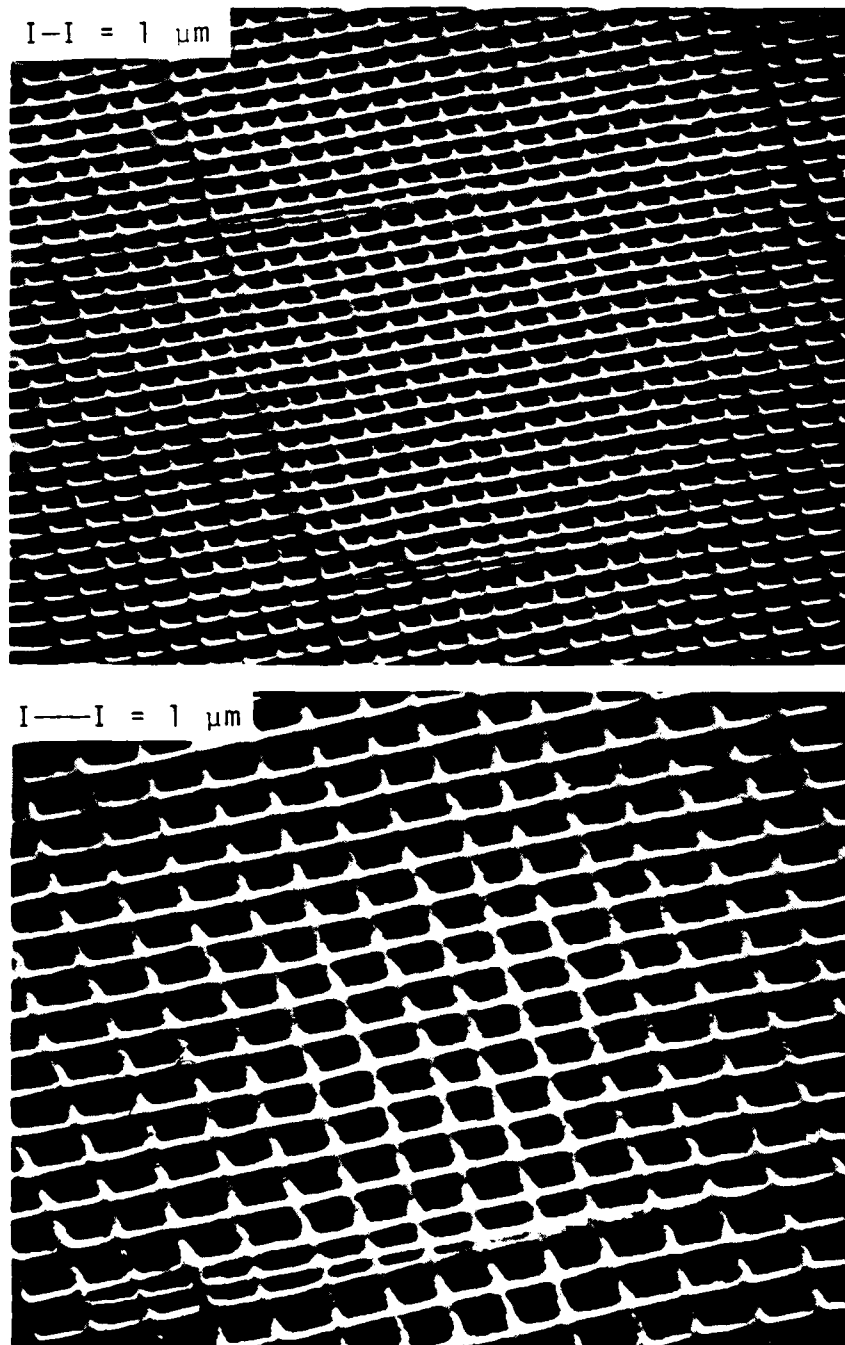
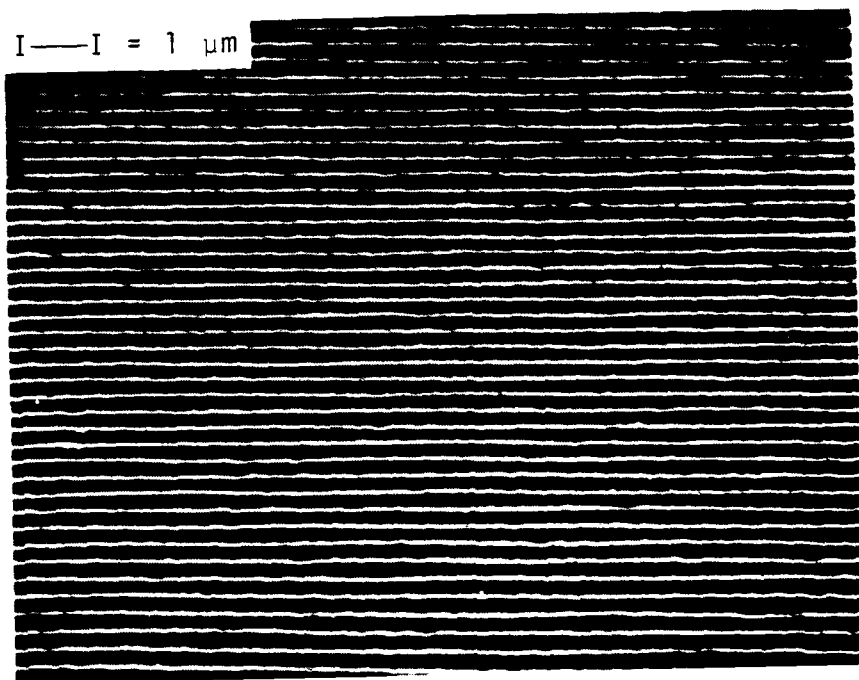Fig. A5-24 Grid pattern written at 4.3 x 10^{14} ions/cm^2 (400 µm/sec). (110) Si at 10° incidence.

Fig. A5-25 Grid pattern written at 4.3×10^{14} ions/cm^2 (400 µm/sec). (110) Si at 10° incidence. Waviness caused by accidental 60 Hz hum on vertical ramp.
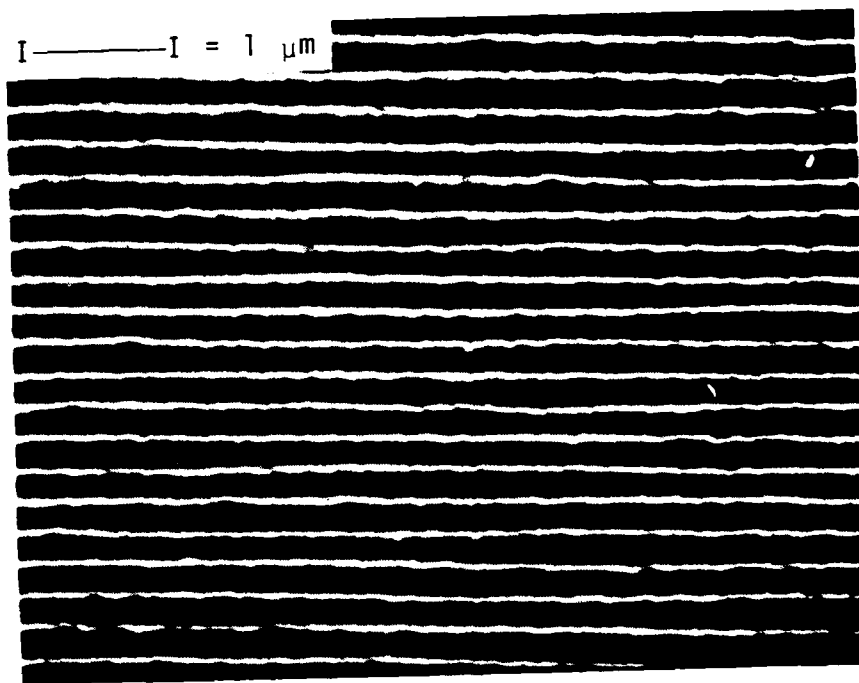
Fig. A5-26 High density patterns written at 2.1×10^{14} ions/cm^2 (800 µm/sec). (110) Si at 10° incidence.
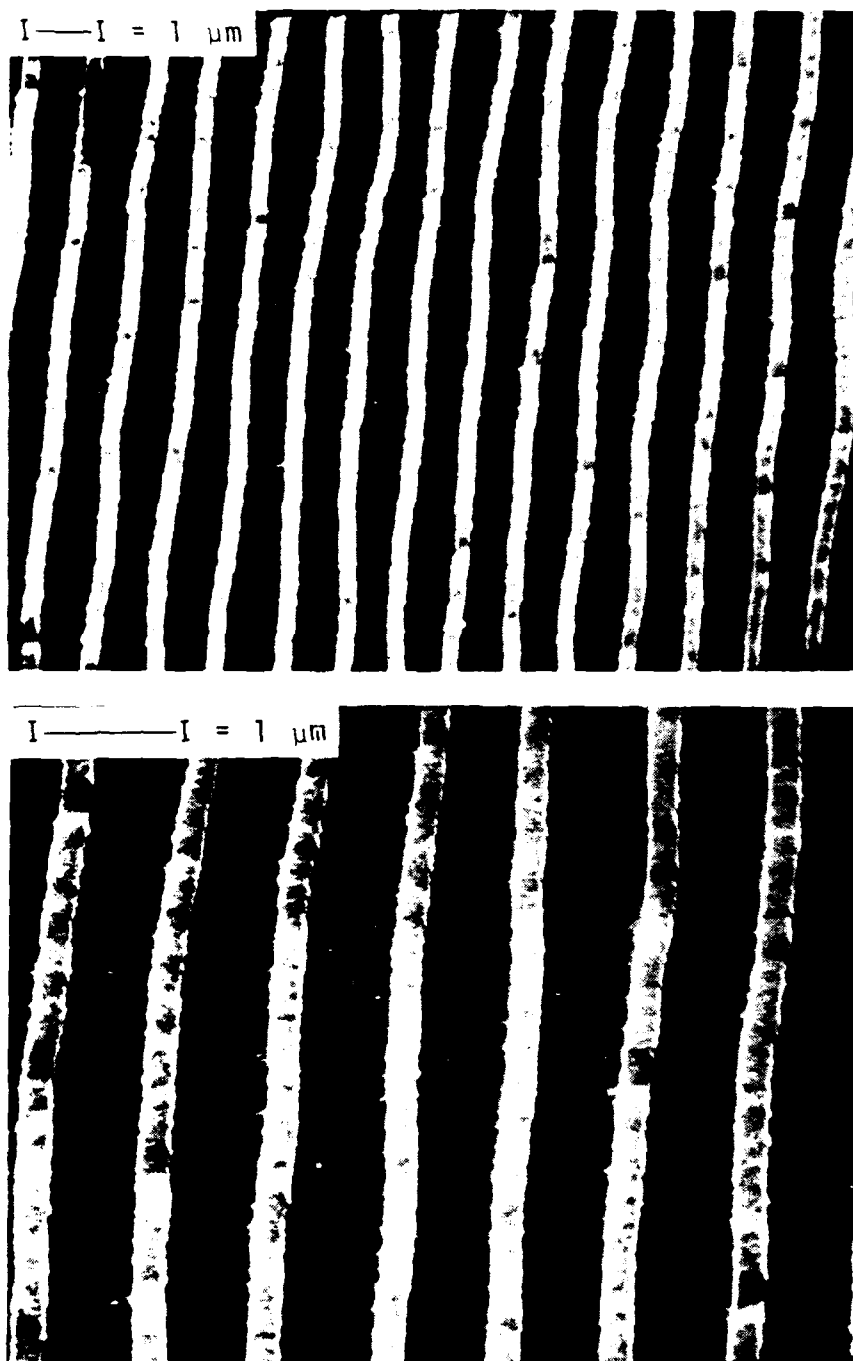
Fig. A5-27 Deep etch of lines written at 4.3 x 10^{14} ions/cm^2 (400 μm/sec).
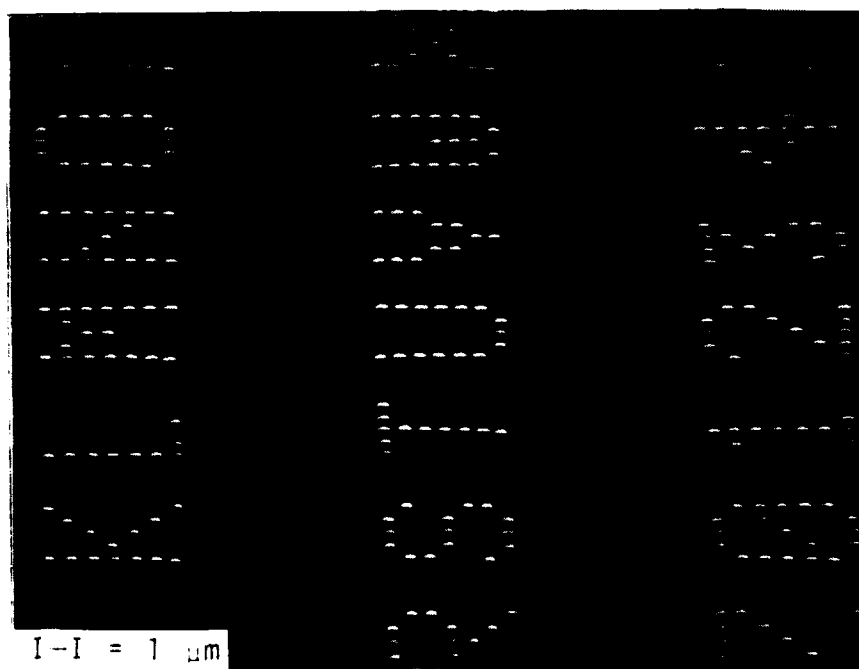Waviness caused by 60 Hz hum on vertical ramp.

c)

d)

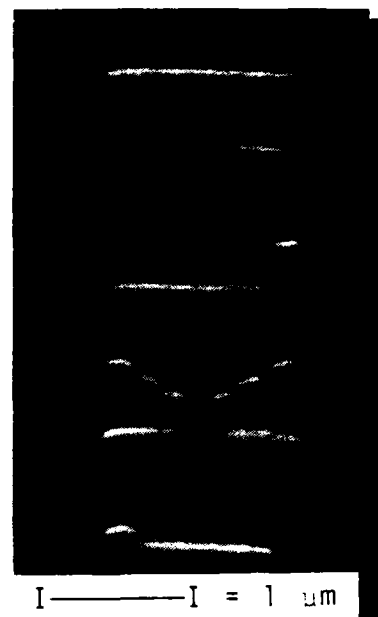I————I = 1 µm

I——I = 1 µm

a)

b)

I-I = 1 µm

I——I = 1 µm
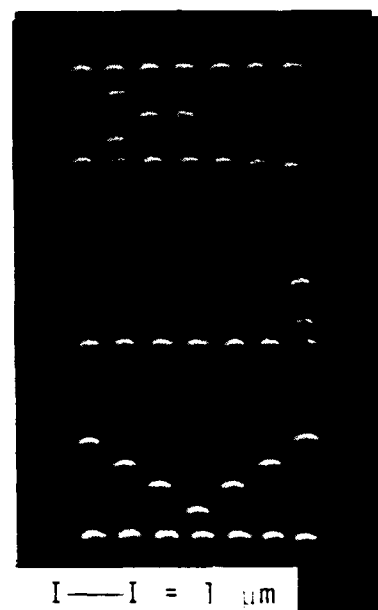
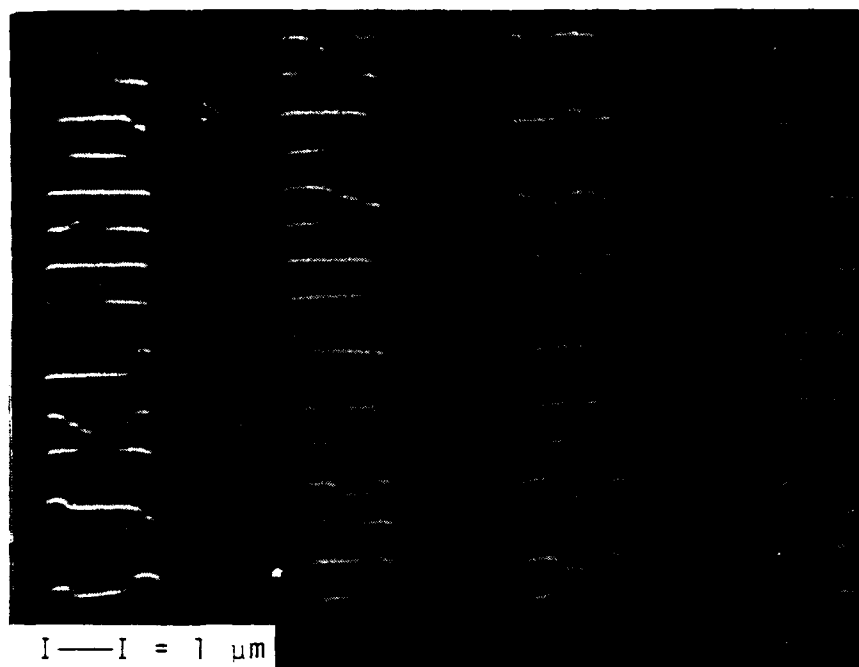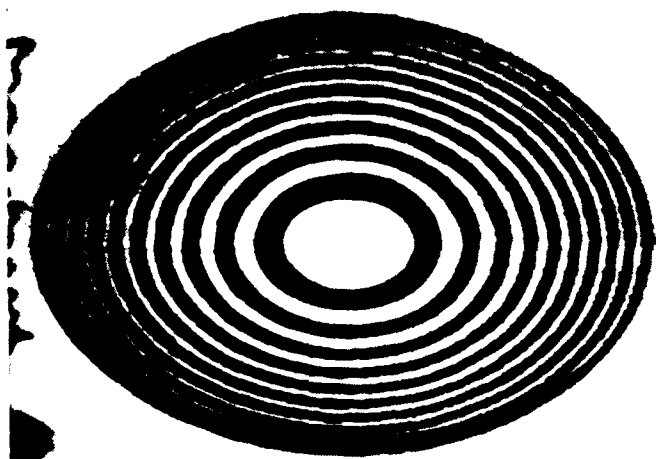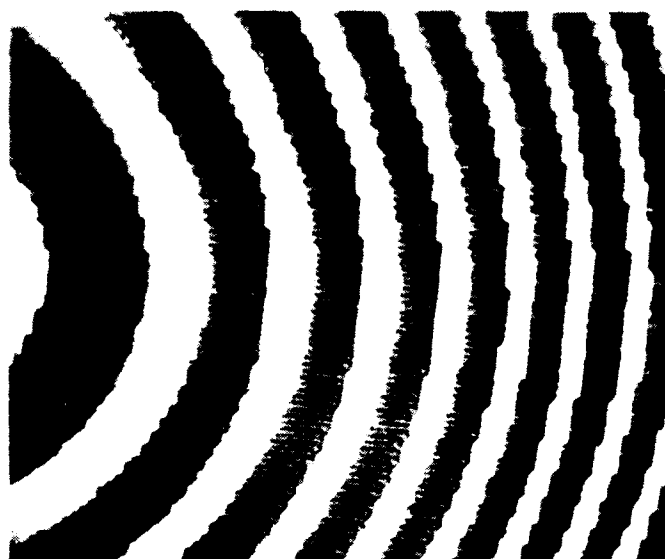Fig. A5-28   Examples of vector scan writing with a 10 pA beam of 50 keV
Ga+ ions in (100) Si. Beam spot diameter ⁓ 500 Å.

GA INDUCED ETCH STOP IN AMORPHOUS SI
60 NM AMORPHOUS SI ON (100) P-TYPE SI
DIRECT IMPLANTATION BY VECTOR SCAN IN 60 KEV UC-SIM
HITACHI HFS-2 25 KEV SEM IMAGES

280 μM HORIZ. F.S.

100 μM HORIZ. F.S.

45 μM HORIZ. F.S.

20 μM HORIZ. F.S.

U.C.

FIG. A5-29

END

FILMED

3-85

DTIC